

---

# Single molecule studies at the nanoscale: STED Fluorescence Fluctuation Spectroscopy in subdiffraction focal volumes

---

Dissertation  
zur Erlangung des Doktorgrades  
der Mathematisch-Naturwissenschaftlichen Fakultäten  
der Georg-August-Universität zu Göttingen

vorgelegt von  
Christian Ringemann  
aus Harsewinkel

Göttingen, den 22.10.2008

**D7**

**Referent: Prof. Dr. T. Salditt**

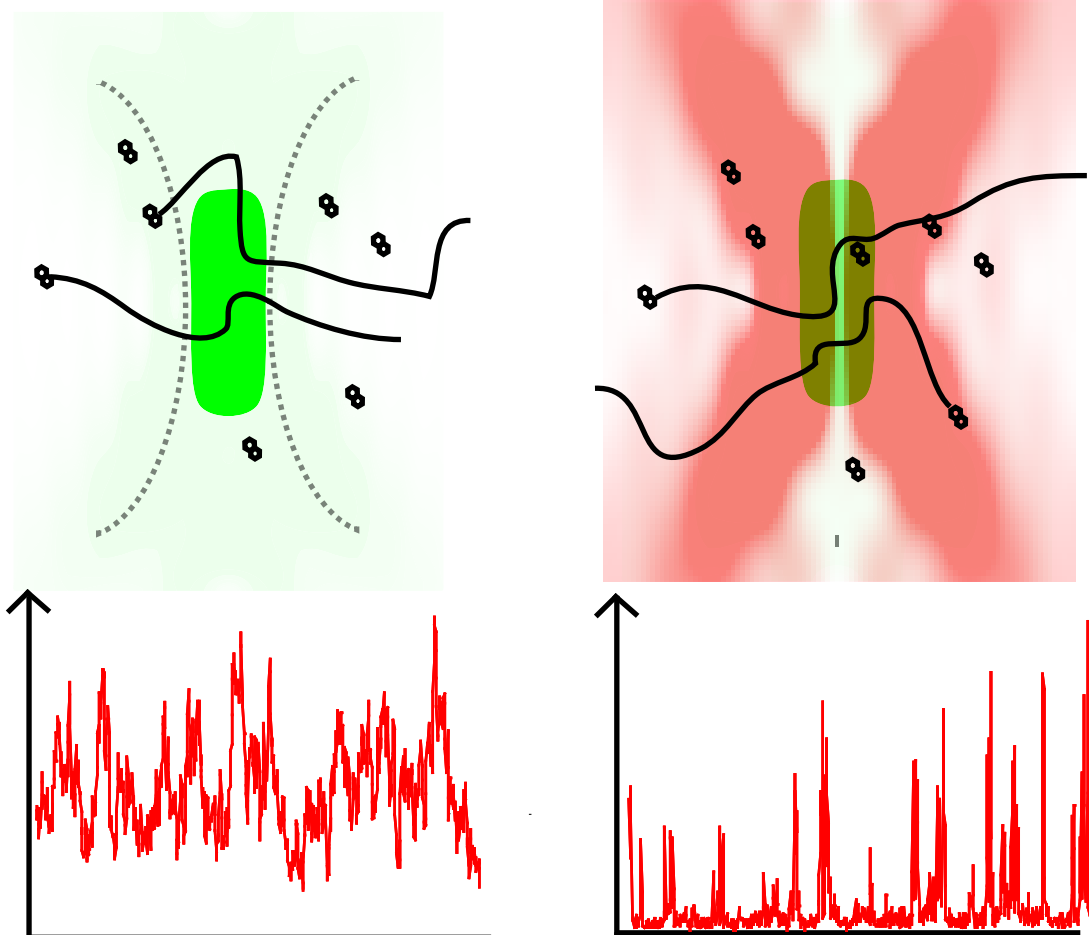
**Koreferent: Prof. Dr. S. W. Hell**

**Tag der mündlichen Prüfung: 20. November 2008**

---

# Single molecule studies at the nanoscale: STED Fluorescence Fluctuation Spectroscopy in subdiffraction focal volumes

---







# Contents

<b>1</b>	<b>Introduction</b>	<b>3</b>
1.1	Fluorescence Microscopy: A Tool for Imaging and Spectroscopy . . . . .	3
1.2	Breaking the diffraction limit: The RESOLFT concept . . . . .	5
1.3	The STED Microscope . . . . .	8
<b>2</b>	<b>Fluorescence Fluctuation Spectroscopy</b>	<b>11</b>
2.1	Introduction . . . . .	11
2.2	Theory of FCS . . . . .	11
2.3	Theory of FIDA . . . . .	15
2.4	Single Molecule Analysis . . . . .	19
<b>3</b>	<b>STED Fluorescence Fluctuation Spectroscopy</b>	<b>20</b>
3.1	Introduction . . . . .	20
3.2	Experimental details . . . . .	21
3.3	STED FFS in solution . . . . .	24
3.3.1	STED Fluorescence Correlation Spectroscopy . . . . .	24
3.3.2	Fluorescence intensity distribution analysis . . . . .	25
3.3.3	Dependence on experimental conditions . . . . .	27
3.3.4	Adaptation of the refractive index . . . . .	29
3.3.5	Modus of confinement . . . . .	30
3.3.6	Suppression of uncorrelated low-brightness signal . . . . .	30
3.3.7	STED-FFS on lipid membranes . . . . .	32
3.3.8	Photobleaching . . . . .	34
3.4	Conclusion . . . . .	38
<b>4</b>	<b>STED Fluctuation Spectroscopy on biological membranes</b>	<b>39</b>
4.1	Introduction . . . . .	39
4.1.1	The cell membrane . . . . .	39
4.1.2	The 'raft' controversy . . . . .	40
4.2	Experimental details . . . . .	42
4.3	STED FFS on cell membranes . . . . .	47
4.3.1	Lipid Diffusion in the cellular plasma membrane on a nanoscale . . . . .	47
4.3.2	Monte Carlo simulations of lipid diffusion . . . . .	58
4.3.3	Membrane affinity of the labeled lipids . . . . .	61
4.3.4	Photobleaching and adverse STED effects on the plasma membrane . . . . .	63



# 1 Introduction

## 1.1 Fluorescence Microscopy: A Tool for Imaging and Spectroscopy

Fluorescence Microscopy is nowadays the most widespread microscopy technique used in the Life Sciences. The physical phenomenon Fluorescence was coined in 1852 by Sir George Gabriel Stokes in his famous paper 'On the refrangibility of light'[108] as a description of the observation of the light emission from  $\text{CaF}_2$ , when illuminated with UV light. The Jablonski diagram in figure 1.1 gives an overview of the different electronic states and their energy levels, which are involved in the process of fluorescence. Fluorescence dye molecules are excited by photons of a certain energy (wavelength) from the singlet ground state  $S_0$  into the first excited singlet state  $S_1$ , from which they relax back into the ground state, usually on a nanosecond timescale, by emitting photons of a slightly higher wavelength due to the so called Stokes shift.

The noninvasive nature of the fluorescence light makes it possible to investigate biological processes in living cells and living organisms with a minimum disturbance of the cellular environment and, by using far-field optics, one is not restricted to the sample surface. This allows for the investigation of any fluorescently labeled structure within the living cell. To this end a huge variety of different fluorescent tags are available, which enable the labeling of nearly any cellular component, such as lipids, peptides or proteins, with a high degree of specificity. Additionally, fluorescence provides a whole variety of different readouts such as fluorescence lifetime, fluorescence anisotropy, fluorescence intensity and fluorescence color with an excellent signal to noise ratio[26, 66]. This has led to the development of many different imaging and spectroscopic methods with high temporal resolution[79, 73, 104, 129].

Nevertheless, the application of Fluorescence Microscopy in biology faces one major drawback since it is limited by the finite resolution of visible light microscopy due to diffraction[1], making it impossible to analyze most macromolecular building blocks of cells (e.g. protein complexes), either spectroscopically or by imaging. In principle Near-field techniques such as scanning near-field optical microscopy (SNOM)[86], superlenses[82] and probing on nanostructures[69, 117] are able to overcome the resolution limit and are already successfully applied in investigation of biological macromolecular structures. Yet, those techniques are limited to the analysis of objects close to the surface, which leaves them not free of artificial influence prohibiting a bias free analysis. Other optical methods with an operating wavelength far below the visible range, such as electron microscopy or x-ray spectroscopy[8, 63], also provide a sufficiently high resolution even down to the atomic scale, but mostly either depend on fixed cells or are highly destructive towards the cellular environment and are therefore not truly live cell compatible[38, 83].

In recent years the group of Prof. Hell was able to break the diffraction limit by exploiting the internal photophysical properties of fluorescent dyes[46], which led to the development of a whole range of fluorescent nanoscopy methods[48]. The most prominent is the STED - Microscope (STImulated

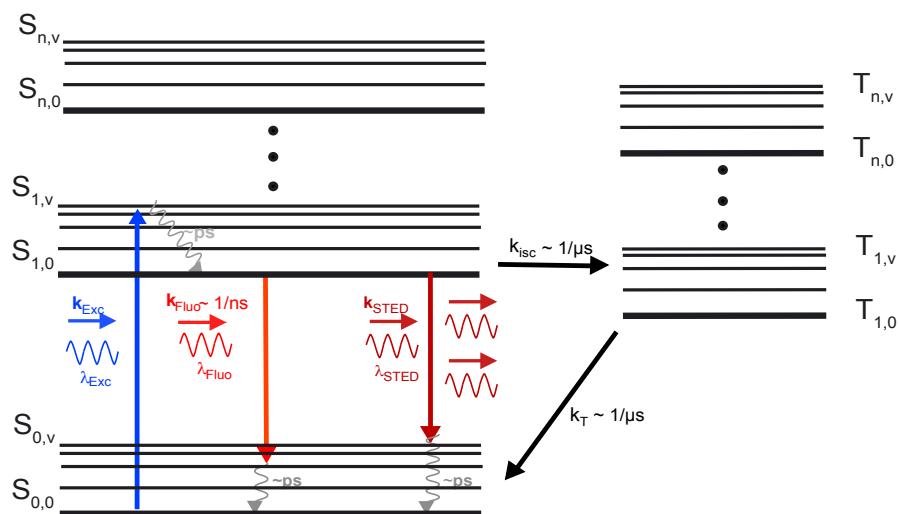


**Figure 1.1: Energy level scheme of a fluorescent dye molecule.** Electronic singlet ( $S$ ) and triplet ( $T$ ) energy levels of the first and higher order ( $S_n$ ,  $T_n$ ), as well as additional vibrational levels (e.g.  $S_{..,v}$ ) are shown. Molecules are instantaneously excited from the electronic ground state ( $S_{0,0}$ ) to a vibrational level of the first excited electronic state  $S_{1,v}$  by a photon of wavelength  $\lambda_{exc}$  and quickly relax to the vibrational ground state of the first excited electronic state  $S_{1,0}$  within  $10^{-12}$  s. Fluorescence occurs from the first excited electronic state normally within  $10^{-9}$  s (fluorescence rate  $k_{fluo} = 1 \cdot 10^8 - 10 \cdot 10^8$  1/s) by emitting a photon of lower energy than the excitation photon, i. e., with a wavelength  $\lambda_{fluo} > \lambda_{exc}$  due to the Stokes shift. The electronic triplet state  $T_1$  is populated via intersystem crossing on a microsecond time scale (intersystem crossing rate  $k_{isc} = 1 \cdot 10^6$  1/s), since the  $S - T$  transition is normally spin forbidden. This long living dark state of the molecule is spontaneously depopulated non-radiantly by thermal relaxation in aqueous solution ( $10^{-6}$  s, triplet relaxation rate  $k_T = 1 \cdot 10^5$  1/s). If an already excited dye molecule is hit by a second photon of the right wavelength  $\lambda_{STED}$  stimulated emission can occur with an effective STED rate  $k_{STED}$  depending on the intensity of the STED beam.

Emission Depletion Microscope), which makes it possible to image in cells with a resolution below  $<30$  nm [21, 22].

In this study, I will show the extension of the STED method to the study of single molecule dynamics at the nanoscale. Studying dynamics on the basis of single-molecule detection has gained new, detailed insights into physical, chemical and biological problems and is supported by statistical analysis tools such as fluorescence fluctuation spectroscopy (FFS) including the prominent techniques Fluorescence Correlation Spectroscopy (FCS)[32, 44, 71] and photon-counting histogram analysis (PCH)[16] or fluorescence intensity distribution analysis (FIDA) [58].

## 1.2 Breaking the diffraction limit: The RESOLFT concept

In a conventional scanning far-field fluorescence microscope a propagating light beam is focused through a high aperture objective lens into a sample. This leads to a diffraction limited pattern called the focal spot, due to a constructive interference of the focused light. The intensity distribution in the focal plane  $I(r)$  (also called the point spread function - PSF), as the square of the electrical field amplitude  $|E|^2$ , is given according to scalar diffraction theory by[11]:

$$I(r) = |E(r)|^2 \cdot \int_0^\alpha \sqrt{\cos\theta} \cdot \sin\theta J_0\left(k\sqrt{x^2 + y^2} \cdot \sin\theta\right) \exp(ikz \cdot \cos\theta) d\theta \quad (1.2.1)$$

with the spatial coordinates  $r = (x, y, z)$ , the semi - aperture angle  $\alpha$ , the zero order Bessel function  $J_0$  of the first kind, the refractive index  $n$  of the medium surrounding the sample and the wavenumber  $k = 2\pi n/\lambda_0$ , with  $\lambda_0$  being the vacuum wavelength of the focused light. The resolution of such a microscope is given by the full width half maximum (FWHM) of the central maximum of the PSF :

$$\Delta x, \Delta y \approx \frac{\lambda_0}{2n\sin\alpha}, \quad (1.2.2)$$

in the lateral directions  $(x, y)$  and in the axial direction  $z$  along the optical axis by:

$$\Delta z \approx \frac{\lambda_0}{n\sin^2(\alpha/2)}, \quad (1.2.3)$$

where  $\lambda$ ,  $n$  and  $\alpha$  denote the wavelength of the focused laser light, the refractive index and the semi-aperture angle of the objective lens, respectively. The expression  $n \cdot \sin\alpha$  is often combined to the numerical aperture  $NA$ , being solely defined by the characteristics of the objective lens in use. The image formation is usually done by point wise scanning over the sample and detecting the fluorescence at each point. The resolution limit forecloses the separation of objects which are closer together than roughly half the wavelength of the applied light. To give a concrete example: A microscope setup using an excitation laser light of  $\lambda_{exc} = 633$  nm and an oil objective lens with a numerical aperture of  $NA = 1.42$  has a theoretical resolution limit of  $\Delta x, \Delta y \approx 223$  nm in the lateral direction.

The RESOLFT concept proposes a way to overcome this barrier by utilizing a reversible saturable switching mechanism of an optical property of a dye molecule between two optically distinguishable states  $X$  and  $Y$  (see figure 1.2a)[47]. This can be the fluorescence itself (bright and dark states), the absorption (absorbing and non-absorbing), the orientation of the molecule (perpendicular and parallel), or any other optically property of the dye. Let us assume that the switching mechanism between  $X$  and  $Y$  is light driven with a forward rate  $k_{XY} = \sigma_{XY} \cdot I = \sigma_{XY} \cdot P/A$ , with  $\sigma_{XY}$  denoting the molecular cross section of the transition,  $I$  the intensity and  $P$  the power of the incident light and  $A$  the focal area ( $P/A = I$  is a substitute for the intensity  $I$  of the applied laser light, which will be used during my work, since the power  $P$  of the incident light is an easily accessible parameter in an optical setup). The reverse rate is either light or thermally driven with a rate  $k_{YX}$ . The system can than be described by the following rate equations:

$$dN_X/dt = -dN_Y/dt = k_{YX}N_Y - k_{XY}N_X, \quad (1.2.4)$$

with  $N_X + N_Y = 1$ , and for  $t \gg \frac{1}{k_{XY} + k_{YX}}$  one gets the following steady state values  $\overline{N}_X$  and  $\overline{N}_Y$ :

$$\begin{aligned} \overline{N}_X &= \frac{k_{YX}}{k_{YX} + k_{XY}} \\ \overline{N}_Y &= 1 - \overline{N}_X = \frac{k_{XY}}{k_{YX} + k_{XY}} \end{aligned} \quad (1.2.5)$$

If the initial population of  $N_X$  is normalized to  $N_X = 1$ , one can approximated the steady state population of  $\overline{N}_X$  for a pulsed illumination with a short rectangular pulse of duration  $\tau$  for the switching light between  $X$  and  $Y$  as:

$$\overline{N}_X = \exp(-\sigma_{XY} \cdot \tau \cdot P/A) = \exp(-P/P_{SAT}), \quad (1.2.6)$$

as long as  $k_{XY} \gg k_{YX}$ , which is especially fulfilled for large average power of the incident light  $P = \frac{1}{T} \int_0^T P(t)dt$ . The saturation power  $P_{SAT} = -\sigma_{XY} \cdot \tau/A$  is defined as the power  $P$  of the switching light, where the population  $\overline{N}_X$  has dropped to  $\frac{1}{e}$  of its initial value(see figure 1.2c).

As can be seen in figure 1.2 b) with such a light driven transition between two distinguishable states and an appropriately shaped illumination pattern for the driving light, featuring a central area with zero intensity, the effective detection area can be reduced beyond the diffraction limit. This enables to specifically address spectroscopic properties of molecules on a subdiffraction length scale, or if one scans with the whole arrangement over the sample, to successively build an image with subdiffraction resolution. In the next section I am going to concrete this abstract concept by introducing the type of RESOLFT microscope I have used for my study: The STED Microscope. Besides the STED Microscope several other high resolution microscopes based on the RESOLFT concept, which take advantage of different switching mechanism, have been realized (GSD (ground

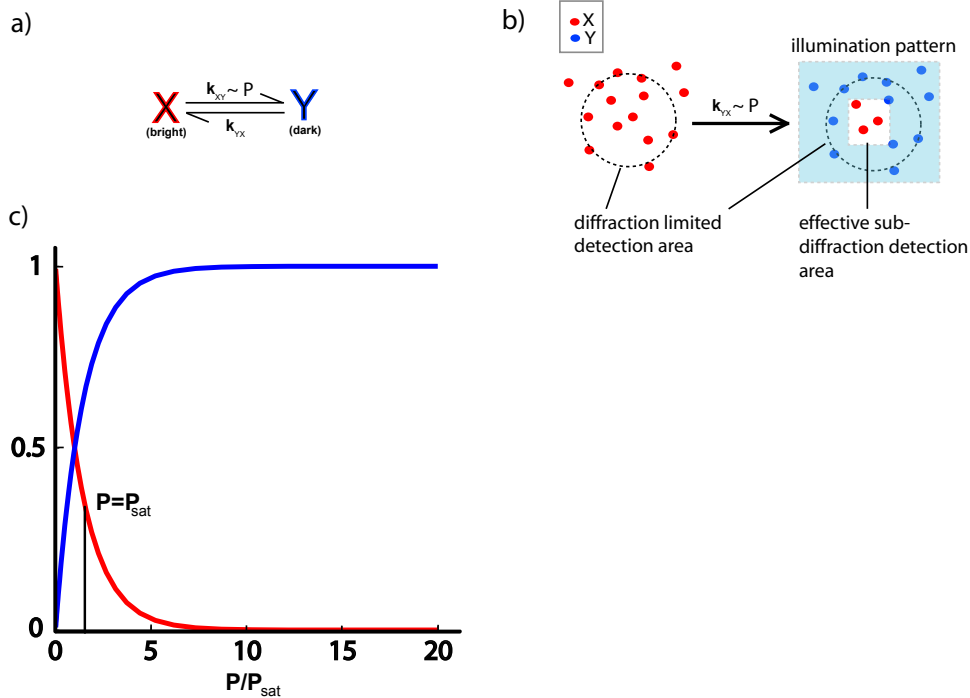


**Figure 1.2: Saturation behavior of a simple two state photoswitching model** a) Scheme of the two state model. State  $X$  is fluorescent, absorbing, state  $Y$  is non-fluorescent, non-absorbing. The transition between  $X$  and  $Y$  is light driven and is proportional to the applied power  $P$ . b) The dashed circle indicates the diffraction limited detection area formed by a far-field optic. All molecules in state  $X$  (red dots) within the detection area contribute to the signal. After applying a particular illumination pattern (light blue) for switching off featuring a central area with zero intensity only molecules within this area of subdiffractional size contribute to the overall signal. c) Dependence of the subpopulation  $N_X$  and  $N_Y$  on the saturation factor  $P/P_{\text{sat}}$  for pulsed illumination (see equation 1.2.6). With high enough power  $P$  one can virtually move all the molecules from state  $X$  to state  $Y$ .

state depletion) microscopy[14], RESOLFT microscopy with switchable proteins[51, 99], RESOLFT microscopy with switchable photochromic compounds[12]).

### 1.3 The STED Microscope

The thus far most successfully realized RESOLFT type microscope is the STimulated Emission Depletion Microscope. The first STED microscope was realized as an extension of a standard fluorescence scanning microscope[64] with pulsed lasers used for excitation and for STED. The two optical distinguishable states X and Y are represented by the first excited state  $S_1$  (bright) and the ground state  $S_0$  (dark) of the dye and the inhibition of the fluorescence from the bright state  $S_1$  is driven by stimulated emission induced by a second laser beam. A detailed description of the different energy states can be seen in the Jablonski Diagram in figure 1.1. The steady state populations of the three electronic energy levels for the dye, the ground state  $S_0$ , the first excited state  $S_1$  and the triplet state  $T_1$  can be described by the following rate equation system<sup>1</sup>:

$$\begin{aligned} dS_0/dt &= -k_{Exc}S_0 + (k_{fluor} + k_{STED})S_1 + k_T T_1, \\ dS_1/dt &= k_{Exc}S_0 - (k_{fluor} + k_{STED})S_1 - k_{ISC}S_1, \\ dT_1/dt &= -k_T T_1 + k_{ISC}S_1, \end{aligned} \tag{1.3.7}$$

At least for low excitation power  $P_{exc}$  one can safely neglect the triplet population  $T_1$ , due to the low probability of intersystem crossing. Additionally, since  $k_{STED} \sim P_{STED}$ , for high enough power of the STED beam  $P_{STED}$ , it follows that  $k_{STED} \gg k_{fluor}$ . Thus the rate equation system can in this case be further reduced to a simple two level system:

$$\begin{aligned} dS_0/dt &= -k_{Exc}S_0 + k_{STED}S_1, \\ dS_1/dt &= k_{Exc}S_0 - k_{STED}S_1 \end{aligned} \tag{1.3.8}$$

Since this two level system is equivalent to the system described by equation 1.2.4, the steady state population  $\overline{S_1}$  for a STED setup with a pulse duration  $\tau$  and an average Intensity  $\overline{P_{STED}}$  is approximated by:

---

<sup>1</sup>Note, that this is already a simplification, since also higher energy levels for the singlet as well as for the triplet manifold have to be considered to have a full account of the photophysical properties of a dye molecule[91]. Additionally photo destruction is neglected in this model, which can occur from the singlet and triplet states[31, 29]. The higher vibrational states can safely be neglected because of the fast relaxation to the ground state.



$$\begin{aligned}\overline{S}_1 &= S_1^0 \cdot \exp(-k_{STED} \cdot \tau) \\ S_1^0 \cdot \exp(-\sigma_{STED} \tau \cdot \overline{P_{STED}}/A) &= S_1^0 \cdot \exp\left(-\frac{\overline{P_{STED}}}{P_{SAT}}\right)\end{aligned}\quad (1.3.9)$$

where  $S_1^0$  represents the initial population of the first excited state reached after the preceding pulsed excitation and  $\sigma_{STED}$  the molecular cross section for the stimulated emission. The parameter  $P_{SAT}$  is an experimental accessible parameter and can for example be extracted out of the depletion curve shown in figure 1.3a). After the STED pulse duration the remaining population of  $\overline{S}_1$  renders a fluorescence signal  $F$  depending on the quantum yield  $q$  of the dye molecules and the detection efficiency  $h_{det}$  of the setup,

$$F \sim q \cdot h_{det} \cdot \overline{S}_1. \quad (1.3.10)$$

To get a resolution improvement with a STED Microscope it is necessary to inhibit the fluorescence  $F$  everywhere but at a single isolated spot in the center of the excitation focus. Therefore one has to shape the focus of the STED laser beam so that it features a central zero. This is done by introducing a wave plate into the STED beam, which leads to defined phase retardation of the beam wavefront ensuring a doughnut shaped intensity distribution in the focal plane for the STED beam, as illustrated in the inset of figure 1.3b) (for a list of possible inhibition patterns see [61]). Combining the STED focus with an excitation focus so that the center zero of the STED focus matches the maximum of the confocal focus results in an effective fluorescence spot of subdiffraction size (inset of figure 1.3b)) due to the saturated inhibition of the fluorescence in the focal periphery. The actual size of the spot can be seamlessly tuned depending on the applied STED power and is approximately described by a slight modification of the Abbe equation[42]:

$$FWHM_{x,y}, d \approx \frac{\lambda}{2 \cdot NA \sqrt{1 + P_{STED}/P_{SAT}}} \quad (1.3.11)$$

with the wavelength  $\lambda$  of the fluorescence light, the numerical aperture  $NA$  of the objective and the saturation STED intensity  $P_{SAT}$  being characteristic for the fluorophore and the STED light distribution in use.

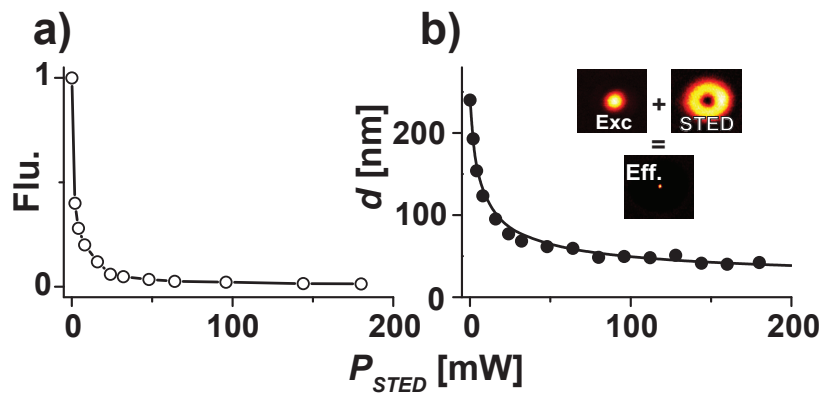


**Figure 1.3: Far-field nanoscopy.** (a) STED Microscopy is based on saturated fluorescence inhibition (Flu.) by red shifted STED light featuring a focal intensity distribution with a local zero ((b) inset) and is overlaid with the diffraction-limited excitation spot ((b) inset). (b) The effective focal fluorescence spot is of sub-diffraction size ((b) inset), its diameter  $d$  decreasing with the power  $P_{STED}$  of the STED light (experimental data (circles) and fit equation 1.3.11 to the data with  $P_{sat} = 3mW$ ). The data depicted are recorded on  $\sim 20nm$  sized crimson beads: fluorescence inhibition when combining the excitation spot with a non-engineered, diffraction limited spot at increasing  $P_{STED}$ (a), and average diameter  $d = FWHM$  determined from the STED images at increasing  $P_{STED}$  (b) (see section 3.1 experimental details: STED microscope for more details). The intensity distributions of the excitation and STED light (inset (a)) were both measured by scanning a scattering subdiffraction sized gold bead through the focal region. The effective fluorescence spot of the STED microscope (inset (b)) was measured on a fluorescence crimson bead with  $P_{STED} = 150$  mW.

## 2 Fluorescence Fluctuation Spectroscopy

### 2.1 Introduction

As already mentioned in the first chapter one advantage of using fluorescence as a readout in a microscope is the excellent signal to noise ratio as well as the high sensitivity of this photophysical phenomena. This enables a whole range of spectroscopic methods referred to as Fluorescence Fluctuation Spectroscopy (FFS), which in particular depends on the ability to detect single molecules. Already today the requested sensitivity is easily realized even with the most basic confocal fluorescence microscopes. At the time when Elson and Madge derived the theory for FCS (Fluorescence Correlation Spectroscopy)[33], the first FFS related technique, the experimental realization was rather cumbersome and therefore not widely used. Not until the first APD (avalanche photo detectors), the confocal microscope and stable laser sources became commercially available in the 1990's one could observe a boost in the development FFS techniques and applications[90].

All of these techniques take advantage of fluctuations in the fluorescence signal stemming for example from fluctuations in the dye concentration due to the diffusion of dyes through the confocal detection volume. Also intra- or inter-molecular interactions can be analyzed by FFS as long as they influence the fluorescence signal of a dye molecule (e.g. singlet - triplet transitions, cis-trans isomerizations or other bright - dark state transitions of the dye). In this work I have used three FFS techniques (FCS: Fluorescence Correlation Spectroscopy, FIDA: Fluorescence Intensity Distribution Analysis, SMA: Single Molecule Analysis), which I will describe in greater detail in the following sections.

### 2.2 Theory of FCS

**Standard model: single molecule diffusion** FCS (Fluorescence Correlation Spectroscopy) is the earliest FFS techniques developed and has been extensively described and reviewed in numerous articles ([70, 89, 102, 119]). Therefore I will only briefly review the concept.

The fluorescence signal defined as  $F(t) = \langle F(t) \rangle + \delta F(t)$ , stemming from dye molecules diffusing through the focus, can be divided into a time-averaged fluorescence signal  $\langle F(t) \rangle$  and a temporally fluctuating part  $\delta F(t)$ . FCS analyzes the temporal characteristic of the fluorescence signal by calculating the normalized second order autocorrelation function of the signal defined as:

$$\begin{aligned} G(t_c) &= \frac{\langle F(t)F(t+t_c) \rangle}{\langle F(t) \rangle^2} = 1 + \langle \delta F(t) \cdot \delta F(t+t_c) \rangle / \langle F(t) \rangle^2 \\ &= 1 + \langle \delta F(0) \cdot \delta F(\tau) \rangle / \langle F \rangle^2 \end{aligned} \tag{2.2.1}$$

with correlation time  $t_c$  or  $\tau$  and triangular brackets indicating averaging over the measurement

time. The total fluorescence signal  $F(t)$  stems from all parts of the detection volume  $V$ :

$$F(t) = \sigma \cdot q \cdot K \cdot \int_V I_{exc}(r) h_{det}(r) C(r, t) d^3r, \quad (2.2.2)$$

where  $K$ ,  $\sigma$  and  $q$  are constants giving the overall detection efficiency of the microscope, the molecular absorption cross section and the quantum yield of the dye, respectively.  $C(r, t)$  denotes the temporal spatial distribution of the dye molecule concentration and  $I_{exc}(r)$  and  $h_{det}(r)$  are functions reflecting the spatial distribution of the excitation PSF (compare 1.2.1) and the detection efficiency of the optical setup and are usually combined into a single dimensionless brightness function  $B(r) = I_{exc}(r)/I_0 \cdot h_{det}(r)$ , with  $I_0$  being the excitation intensity amplitude maximum. In the standard FCS approach the brightness function of a confocal microscope is usually well approximated by a three dimensional Gaussian function:

$$B(r(x, y, z)) = \exp[-2(x^2 + y^2)/w_0^2] \exp(-2z^2/z_0^2), \quad (2.2.3)$$

where  $w_0$  and  $z_0$  are the lateral and axial coordinates at which the brightness value has dropped to a factor of  $e^{-2}$  compared to the maximum. Especially, the beam waist  $w_0$  plays an important role for FCS and therefore it is important to keep in mind that it is closely related to the FWHM of the PSF:

$$FWHM_{x,y} \approx \sqrt{2 \ln 2} \cdot w_0 \quad (2.2.4)$$

Since fluctuations in the fluorescence signal stem either from fluctuations  $\delta C(r, t) = C(r, t) - \langle C \rangle$  in the molecule concentration, from changes in the absorption cross section  $\delta\sigma$  or in the quantum yield  $\delta q$ , they can be conveniently described by

$$\delta F(t) = \delta\sigma \cdot \delta q \cdot K \cdot I_0 \int B(r) \delta C(r, t) d^3r. \quad (2.2.5)$$

Fluctuations in the quantum yield of the molecules  $\delta q$  can stem from transitions between bright and dark states (like the triplet state, quenching or environmental changes of the dye), whereas fluctuation in the molecular absorption cross section  $\delta\sigma$  are among others due to the rotation of the molecules. The factor  $\eta = \sigma \cdot q \cdot K \cdot I_0$  determines the average countrate per detected molecule per second (molecular brightness) and is an important factors in FCS measurements. In a first step I will assume for simplicity that  $\sigma$  and  $q$  are constant or that fluctuations in both values are faster than the time resolution of the FCS measurement. If one inserts equation 2.2.5 into equation 2.2.1 one gets the following autocorrelation function:

$$G(\tau) = 1 + \frac{\int \int B(r) B(r') \langle \delta C(r, 0) \cdot \delta C(r, \tau) \rangle d^3r \cdot d^3r'}{(\langle C \rangle \int B(r) d^3r)^2} \quad (2.2.6)$$

In the case of freely diffusing molecules with a diffusion coefficient  $D$ , the concentration autocorrelation

$\langle \delta C(r, 0) \cdot \delta C(r, \tau) \rangle$  is given by[71]

$$\langle \delta C(r, 0) \cdot \delta C(r, \tau) \rangle = \langle C \rangle (4\pi D\tau)^{-3/2} \exp(-(r - r')^2 / 4D\tau), \quad (2.2.7)$$

which results in the following normalized autocorrelation function assuming a Gaussian shaped brightness function  $B(r)$ :

$$G(\tau) = \frac{1}{V \langle C \rangle} \cdot \frac{1}{(1 + \tau/\tau_{xy})} \cdot \frac{1}{\sqrt{1 + \tau/\tau_z}}, \quad (2.2.8)$$

where  $\tau_{xy} = \frac{w_0^2}{4D}$  is the average lateral diffusion time and  $\tau_z = \frac{z^2}{4D}$  is the average axial diffusion time for a molecule passing through the measurement volume

$$V = \frac{(\int B(r) d^3r)^2}{\int B^2(r) d^3r} = \pi^{3/2} \cdot w_0^2 z. \quad (2.2.9)$$

The amplitude of the autocorrelation curve  $G(0) = \frac{1}{V \langle C \rangle}$  is inversely proportional to the average number of particles  $N = V \langle C \rangle$  in the measurement volume. If the measurement volume  $V$  is known with a high enough precision or calibrated beforehand, the average molecule concentration can be calculated from the autocorrelation amplitude  $G(0)$  by  $\langle C \rangle = \frac{1}{V \cdot G(0)}$ .

For molecules that do not diffuse in a 3D - volume but are restricted to a two dimensional system the autocorrelation function is simply reduced to[101]:

$$G_{2D}(\tau) = \frac{1}{V \langle C \rangle} \cdot \frac{1}{(1 + \tau/\tau_{xy})} \quad (2.2.10)$$

**Extended model: hindered diffusion, additional kinetics, uncorrelated background** Thus far the diffusion of the molecules were always assumed to be free, which means that the mean square displacement of the molecules increases linearly with the time,  $\langle r^2 \rangle \sim t$ . This linear relationship breaks down if molecules are hindered in their diffusion pathways because of obstacles, trapping or barriers. In that case the mean square displacement time relationship has to be modified yielding  $\langle r^2 \rangle \sim t^\alpha$ , with  $\alpha < 1$  [93, 101, 113]. This effects the distribution of passage times for molecules diffusing through the focal volume, normally described by one diffusion constant  $D$ . There are in principle two different ways to account for this change. First, one can think of artificially separating the molecules into classes with different diffusion constants  $D_i$  leading to different diffusion times  $\tau_D^i$ . Each of this molecule class would then represent a fraction  $A_i$  of the total number of diffusing molecules. Experimentally, it has been shown that two classes of molecules are in most cases sufficient to get good agreements between the recorded data and the model function, which is then defined as[101]:

$$G_{3D}(\tau) = \frac{1}{V \langle C \rangle} \left[ A_1 \cdot \frac{1}{(1 + \tau/\tau'_{xy})} \cdot \frac{1}{\sqrt{1 + \tau/\tau'_z}} + A_2 \cdot \frac{1}{(1 + \tau/\tau''_{xy})} \cdot \frac{1}{\sqrt{1 + \tau/\tau''_z}} \right] \quad (2.2.11)$$

with  $0 < A_2 < 1$  giving the fraction of molecules that are hindered or trapped,  $0 < A_1 < 1$  giving the fraction of molecules that diffuse freely ( $A_1 + A_2 = 1$ ) and  $\tau'$  and  $\tau''$  defining the two corresponding molecular transit times.

The other possibility is to introduce an anomaly factor  $\alpha < 1$  into the autocorrelation function to account for the hindered diffusion, which leads to the following expression for the autocorrelation function[101]:

$$G_{3D}(\tau) = \frac{1}{V \langle C \rangle} \cdot \frac{1}{(1 + [\tau/\tau_{xy}]^\alpha)} \cdot \frac{1}{\sqrt{1 + [\tau/\tau_z]^\alpha}}, \quad (2.2.12)$$

where smaller values of  $\alpha$  mean a higher degree of anomaly. Both models are able to describe deviations from normal free diffusion. Which of the two model one should choose depends on the experimental situation and the properties of the investigated sample. The two species model is more descriptive, whereas the anomaly model is defined more rigorously but lacks a clear and intuitive meaning, especially since in this case the diffusion constant  $D$  derived from the diffusion time  $\tau_{xy}$  has a fractional time dimension[62].

Thus far only fluctuations in the fluorescence signal due to diffusion of the molecules were considered in the calculation of the autocorrelation curve. If the brightness of the molecules are effected by intramolecular or intermolecular kinetics, the equation 2.2.8 has to be modified by introducing additional terms accounting for those changes. This leads to a product of autocorrelation functions components for each kinetic reaction  $G_{kinetics}(\tau)$  with  $G_{Diff}(\tau)$  standing for the component of the autocorrelation function due to diffusion defined in equation 2.2.8:

$$G_{total}(\tau) = G_{Diff}(\tau) \cdot \prod G_{kinetics}(\tau) \quad (2.2.13)$$

In the prominent case of triplet kinetic reaction this gives the following autocorrelation function[121]:

$$G(\tau) = G_{Diff}(\tau) \cdot \left[ \frac{1-T}{T} \cdot \exp\left(-\frac{\tau}{\tau_T}\right) \right] \quad (2.2.14)$$

where  $T$  is the average triplet population and  $\tau_T$  is the triplet correlation time.

In figure 2.1a) a typical autocorrelation curve recorded for the dye Atto 647N in a thiodiethanol (TDE) solution is shown. The data is fitted by the autocorrelation function 2.2.8 with an additional triplet term (see equation 2.2.14), which gives the diffusion time  $\tau_{xy}$  in the lateral direction, the diffusion time  $\tau_z$  in the axial direction and the number of particles  $N$  as well as the triplet parameters

of the dye molecule Atto 647N.

In all those cases described above,  $1/G(0)$  always defines the average number of molecules  $N$  in the detection Volume  $V$  as long as the whole fluorescence signal stems from bright dye molecules and is therefore correlated. If one has uncorrelated background  $F_B$  in our system (scattering signal, low brightness species, autofluorescence), which is always the case in a real experiment, one can correct for this by introducing a damping factor for the number of particles[65]:

$$\begin{aligned} G(0) &= 1/N_{FCS} = (1 - F_B/F_{total})^2 \cdot \frac{1}{N_{real}} \\ N_{real} &= (1 - F_B/F_{total})^2 \cdot N_{FCS} \end{aligned} \quad (2.2.15)$$

Thereby one can correct the apparent number particles of our FCS analysis  $N_{FCS}$  and get the corrected number of particles in the focal volume  $N_{real}$  if only the amount of uncorrelated background  $F_B$  is known or experimental accessible.

Damping of the correlation amplitude by low brightness due to noise is absent for the unnormalized correlation function  $G_{raw}(\tau)$ :

$$\begin{aligned} G_{raw}(\tau) &= \langle \delta F(0) \cdot \delta F(\tau) \rangle \\ &= \langle F(0) \cdot F(\tau) \rangle - \langle F(0)^2 \rangle \\ &= G(0) \left[ G_{Diff}(\tau) \cdot \prod G_{kinetics}(\tau) \right] \end{aligned} \quad (2.2.16)$$

with  $G(0) = N_{real} \cdot \eta$ . While the amplitude  $G(0)$  of the unnormalized correlation data is not influenced by uncorrelated low-brightness signal  $F_B$ , knowledge of the fluorescence brightness  $\eta$  is now needed to extract  $N_{real}$  from the amplitude of the autocorrelation function.

### 2.3 Theory of FIDA

**General FIDA theory** Unlike in the time correlation approach of FCS, FIDA (Fluorescence Intensity Distribution Analysis) exploits the information which can be found in the amplitude distribution of the intensity fluctuations of the fluorescence signal, by analyzing the photon counting histogram generated from the number of photons detected in consecutive, constant time intervals  $T$ . There are some requirements that have to be full filled to enable the FIDA analysis of the recorded data[16, 55]:

1. Coordinates of molecules have to be independent of each other.
2. Contribution to fluorescence intensity from a particle can be expressed as a product of a specific brightness  $\eta$  characteristic for the dye molecules and a spatial brightness profile function  $B(r)$

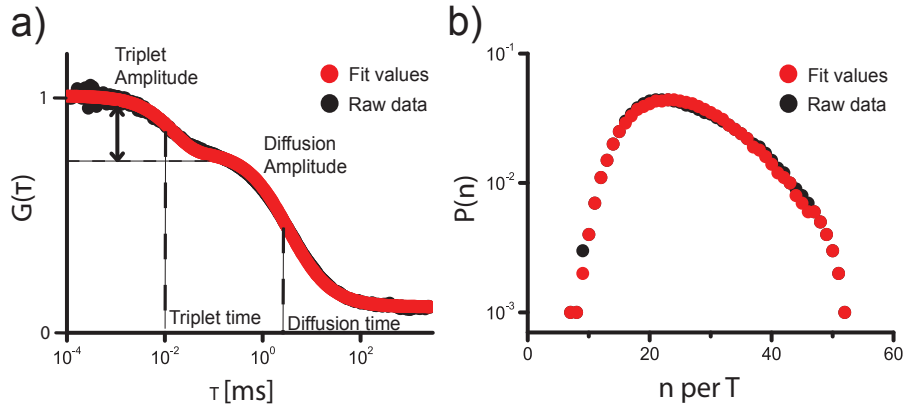


**Figure 2.1: Autocorrelation  $G(\tau)$  (a) and fluctuation intensity distribution function (b) recorded simultaneously for Atto 647N in TDE.**  $P_{exc} = 500$  uW. The time window  $T$  for FIDA is 40  $\mu$ s. The raw data is given by the black circles and the fitted values are the red circles. (a) The autocorrelation amplitude  $G(\tau)$  is plotted against the correlation time  $\tau$ . For the fitting procedure of the autocorrelation curve the equation 2.2.14 was used. (b) The probability  $P(n)$  of  $n$  photons within the time window  $T$  is plotted against the number of photons  $n$ . Fitting of  $P(n)$  is described in the text. From the fit of the autocorrelation curve one gets the diffusion time  $\tau_{xy}$ , the number of particles  $N_{FCS}$ , the average triplet population  $T_{Triplet}$  and the triplet correlation time  $t_T$ . FIDA delivers the number of particle  $N_{FIDA}$ , the brightness  $\eta_{FIDA}$  and the average background signal  $F_B$ .



characteristic for the optical setup.

3. The counting time interval  $T$  has to be short, so that the brightness of the molecules doesn't change due to translational diffusion or any intramolecular changes like e.g. singlet - triplet transition within this time intervall.

Let us now assume that we can divide the spatial brightness function  $B(r)$  of the optical setup into small sub-Volumes  $dV_i$ , where the spatial brightness  $B_i$  of the molecules is constant. Without knowing the shape of the brightness function we can still give an expression for the probability to detect  $n$  photons emitted by  $m$  molecules in the  $i$ -th section of the detection volume:

$$P_i(n) = \sum_{m=0}^{\infty} P_i(m) \cdot P_i(n|m) \quad (2.3.17)$$

where  $P_i(m)$  is the Poissonian distribution of the number of molecules within the small volume element  $dV_i$ , with a mean value of the distribution  $c \cdot dV_i$  for an average concentration  $c$  of the molecules.  $P_i(n|m)$  gives the conditional probability to have  $n$  photon counts when there are  $m$  molecules in the detection volume element and is also a Poissonian distribution with a mean value of  $m\eta B_i T$ . Here,  $\eta$  is the specific brightness as already mentioned in the FCS part and  $B_i$  gives the value of the brightness function in the volume element  $dV_i$ . Therefore the full expression of  $P_i(n)$  is a double poissonian with two parameters  $m\eta B_i T$  and  $c \cdot dV_i$

$$P_i(n) = \sum_{m=0}^{\infty} \frac{(cdV_i)^m}{m!} \cdot \exp(-cdV_i) \cdot \frac{(m\eta B_i T)^n}{n!} \cdot \exp(-m\eta B_i T). \quad (2.3.18)$$

To get the complete fluorescence intensity distribution  $P(n)$  for the whole detection volume  $V$  one has to convolve the individual  $P_i(n)$ :

$$P(n) = P_1(n) \otimes P_2(n) \otimes \dots \otimes P_{\infty}(n) \quad (2.3.19)$$

For a known functional relation between  $B_i$  and  $dV_i$  it is in principle possible, to calculate the contributions from different sections  $P_i(n)$  and combine them per convolution to get the complete probability distribution  $P(n)$ . Direct calculation of this set of convolutions numerically is very time consuming and therefore a generating function  $R_{P(n)}(\varphi)$  is introduced defined as

$$R_{P(n)}(\varphi) = \sum_{n=0}^{\infty} \exp(i\varphi)^n P(n). \quad (2.3.20)$$

This transforms the convolution in equation 2.3.19 into a product of the corresponding generating functions by a Fourier transformation, greatly facilitating the numerical calculations to get the intensity

fluctuation distribution  $P(n)$ . A detailed description can be found in [55, 57].

The uncorrelated background with a mean value  $F_B T$  ( $T$  being the counting time interval) is also Poissonian distributed and has to be convolved with the full intensity fluctuation distribution  $P(n)$  of the fluorescence signal stemming from the dye molecules.

$$P_{total}(n) = P_{dye}(n) \otimes P_{back}(n) = P_{dye}(n) \otimes \frac{(F_B T)^n}{n!} \cdot \exp(-F_B T). \quad (2.3.21)$$

Finally one has to define the relation between the spatial brightness function  $B(r)$  and the volume  $V$ . It may look feasible to do this by using a three dimensional gaussian as in the FCS approach, however it has been shown that this delivers only poor results[55]. Therefore a more heuristic way is considered. First one can introduce a new variable  $x = \ln(B_0/B(r))$ , thereby expressing the three dimensional coordinate  $r$  of the brightness function by a now one dimensional variable  $x$ , being a monotonic function of  $B(r)$ . Afterwards the one dimensional brightness function  $dV/dx$  models the experimental brightness profile with a sufficient accuracy[55]:

$$\frac{dV}{dx} = A_0 x^{a_3} (1 + a_1 x + a_2 x^2). \quad (2.3.22)$$

The system parameters  $a_1$ ,  $a_2$  and  $a_3$  are empirical parameters describing the shape of the brightness profile and can be found by calibrating the optical system with a standard dye solution of known brightness and concentration. The selection of the normalization parameters  $A_0$  and  $B_0$  only give the units of  $V$  and  $B(r)$ , usually defined by the normalization  $\int B(r) dr = \int B^2(r) dr = 1$ . The Gaussian shaped brightness profile would deliver  $dV/dx = A_0 \sqrt{x}$  for the one-dimensional brightness profile, which would be a too rigid expression for the one dimensional brightness profile compared to the one in equation 2.3.22.

To sum it up, FIDA provides a tool to discern the brightness  $\eta$  and the number of particles  $N_{FIDA} = c \cdot V$  of different species from the uncorrelated background  $F_B$  in the average fluorescence signal  $\langle F(t) \rangle = N_{FIDA} \cdot \eta \cdot (B(r)) + F_B$  and is therefore a useful addition to the FCS method, which cannot account directly for the background and is biased in the number of particles[34, 56].

**FIDA correction algorithm** One of the requirements to perform FIDA is the choice of a sufficiently small time window  $T$  so that the brightness of the molecules does not change during this time period due to diffusion. Nevertheless, it is possible to correct for the case when the transition time of the dye through the detection area is equal or smaller than the time window  $T$ . Due to averaging, this would lead to apparently smaller values for the brightness  $\eta(T)$  and increased values for the number of particles in the FIDA analysis  $N_{FIDA}(T)$ . This bias can be corrected by introducing a correction factor  $S < 1$  depending on the ratio between the diffusion time  $\tau_{xy}$  and the chosen time window  $T$  (see [80] for details):

$$N_{FIDA} = N_{FIDA}(T) \cdot S \quad \eta = \eta(T)/S \quad (2.3.23)$$

$$S = [1 + T/\{(6a)(2/\tau_{xy} + 1/\tau_z)\}]^{-a} \approx [1 + (3a/(\tau_{xy}/T))^{-1}]^{-a}$$

where  $\tau_{xy}$  is, e.g., known from complementing FCS analysis and  $a$  is an empirical factor. The simplification is valid since the axial transit time  $\tau_z$  is usually much larger than the lateral transit time  $\tau_{xy}$ .

## 2.4 Single Molecule Analysis

The analysis of single molecules compared to the analysis of molecule ensembles has the advantage that it can specifically resolve heterogeneities of the sample averaged out in the bulk measurements. Both methods, FCS and FIDA are single molecule based analysis tools (only photons of one molecule are correlated with each other). Nevertheless, they are theoretically independent on the number of molecules that are present in the focal detection area as long as those molecules do not influence each other. Therefore, to ensure shorter measurement times, hence higher reproducibility and stability of their results, FCS and FIDA are usually performed at higher concentrations (nM -  $\mu$ M) leading on average to more than one dye molecule in the focal volume.

Unfortunately, independence of the behavior of single molecules can not be assumed a priori especially for more complex environments like cells (e.g. molecular crowding[20]). Therefore it is useful to combine method like FCS and FIDA with a 'true' single molecule analysis. Here, a very low concentration (< nM) of the dye labeled molecules is chosen to ensure that at a time only one molecule is present in the focal detection area. Inevitably, detected photons either stem from the background or a single dye molecule. To be able to differentiate a true photon event from the background, the macro time  $dt_i$  of each photon is collected, defined either as the arrival time from the very beginning of the experiment or as the interphoton time between two consecutive photon events. In the case of a good signal to noise ratio (an absolute prerequisite for a single molecule analysis) dye photons have a much smaller interphoton time than background photons and can therefore be extracted from the bulk of background photons and merged into single bursts of photons stemming from a single molecule diffusing through the focus. To automatize this sorting process, a lot of algorithms exist, taking advantage of the normally poissonian nature of the noise signal by using appropriate filters (see [36] for more details and figure 2.2 for the filtering method used in this study).

On the same time the macro time  $dt_i$  information from many photons can also be used to create FCS curves or the FIDA histograms, losing the information of the individual photon events. It is important to keep in mind that one has to collect photons over a long period of time to get stable FCS curves or FIDA histograms, making this approach of creating FCS and FIDA data more prone to artifacts due to changes in the sample environment (e.g. sample drift). Those artifacts are also sources of potential bias in a pure single molecule analysis.

Although not used in my studies, single molecule analysis offers more information which can be used

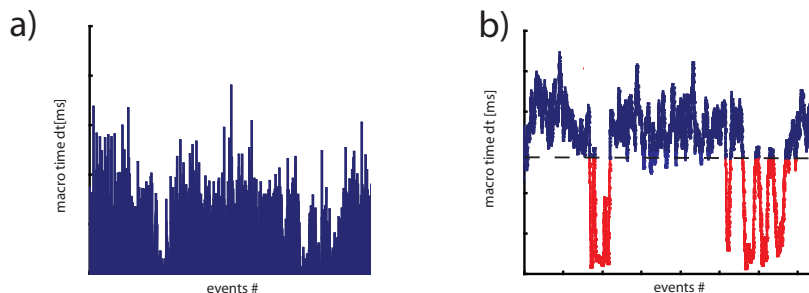


**Figure 2.2: Principle of single molecule burst selection:** **a)** Original macro arrival times for an Atto 647N labeled phospholipid incorporated into the outer cell membrane. The data were collected with a confocal microscope. **b)** The same macro times filtered with a Lee - filter:  $dt^*(i) = \langle dt(i) \rangle + [dt(i) - \langle dt(i) \rangle \cdot \frac{\sigma_i^2}{\sigma_i^2 + s^2}]$ , where  $\langle dt(i) \rangle$  is a moving average with a window width of  $m = 50$  and  $\sigma_i$  is the standard deviation within this window.  $s$  is a deviation parameter, which has to be chosen to ensure good filter results ( $s = 10$ ). Briefly, this filter flattens the poissonian distributed background and preserves signal spikes[25, 35]. The dashed line is the threshold, below which photons events are counted as belonging to fluorescence bursts (red color).

to identify single molecule events. In the case of pulse interleaved excitation, storing the time between the arrival time of the photon and the laser pulse (usually called the micro time) gives the micro time arrival distribution of the photons and thereby the fluorescence lifetime of the dye (This method is called Time Correlated Single Photon Counting or short TCSPC). Before the macro and micro time of the molecules are stored electronically, photons can be sorted by their optical properties like color or polarization by appropriate optical filters and stored with an additional channel information. This enables to sort molecules according to their orientation or dye color.

## 3 STED Fluorescence Fluctuation Spectroscopy

### 3.1 Introduction

In [115] Wawrezinieck et al. showed that a sophisticated FCS approach is in principle able to resolve dynamical details on length scales smaller than the focal diameter by relying on artificial downsized probing volumes. They had grown cells on plates with nanoholes of different diameter and analyzed the change in the diffusion time of membrane molecules depending on the size of those holes. Thereby they were able to identify heterogeneities in the diffusion behavior of certain membrane molecules not visible in a standard confocal probing volume. STED microscopy also provides a method to dynamically scale

the detection area even without the disadvantage of introducing potential artifacts due to the probing volume geometry. Probing on surfaces could heavily influence the dynamical properties of membranes and therefore severely limit the explanatory power of such an approach.

The only requirement the STED method has to fulfill in order to combine it with FCS or other related single molecule techniques is a sensitivity high enough to detect single molecules. It has been shown previously that it is possible to observe single-molecule dynamics in aqueous environment with STED microscopy [59]. However, the first experimental realizations encountered drawbacks having so far impeded further applications. While the decrease in focal volume could directly be measured from the dynamical single-molecule data, a concomitant increase in unspecific background signal precluded accurate single-molecule measurements as well as a reduction of the detection volume further than a factor of 5. Here, I extend these experiments and explore in detail the reason for the unspecific background in order to determine conditions for an optimized detection of single-molecule dynamics at the nanoscale with STED microscopy. This allows for the accurate analysis of dynamical properties of molecules on length scales far beyond the diffraction limit.

## 3.2 Experimental details

### Dye solution

The organic dye Atto 647N (fluorescence excitation and emission maxima of 645 and 670 nm, respectively; Atto-Tec, Siegen, Germany) was dissolved either in PBS buffer (pH = 7.5) or 2,2'-thiodiethanol (TDE, Sigma-Aldrich; 96%, 4% water) to a final concentration of 1-10 nM. Measurements of the free diffusing dye were performed at 22°C in 100  $\mu$ l samples sealed on microscope cover glass.

### Multilamellar layer

100 $\mu$ l of phospholipid blend (DOPE (1,2-dioleoyl-sn-glycero-3-phospho - ethanolamine), DOPS (1,2-dioleoyl-sn-glycero-3-phosphoserine), DOPC (1,2-dioleoyl-sn-glycero-3-phosphocholine) (Avanti polar lipids, Alabaster, AL) 5:3:2 in Chloroform 10mg/ml, stored at -20°C under N<sub>2</sub>-atmosphere) were put on a cover slip and subsequently evaporated under vacuum for roughly 1 1/2 hour. Afterwards the dried lipids were swelled in distilled water to a multilamellar layer for half an hour and rinsed two or three times. For fluorescence measurements 1  $\mu$ l of a 0.01 mg/ml solution of an Atto 647N labeled phospholipid (Atto 647N-1,2-dipalmitoyl-sn-glycero-3-phosphoethanolamine, Atto-Tec) was added to the phospholipid blend before evaporation to yield a dye/lipid molar ratio of approximately 1:100,000.

### Horizontal black lipid bilayer

To perform measurements on a horizontal lipid bilayer (black lipid bilayer), L- $\alpha$ -phosphatidylcholine lipid (type S-IV, Sigma-Aldrich, Steinheim, Germany) was kept at -20°C in a chloroform /

methanol (1:1) mixture at 50 mg/ml. After vacuum evaporation of 100 $\mu$ l of the stock solution I solved the lipid in 100  $\mu$ l n-decane. Planar lipid bilayers were created using a modified painting technique [50, 75]. Briefly, a drop of lipid was smeared over a small hole of  $\sim$ 100  $\mu$ m in diameter in a Teflon foil separating two water filled chambers. The lower chamber was bordered by a microscope cover glass, resulting in a cover glass-to-bilayer distance of approximately 100-150  $\mu$ m. After the evaporation of n-decan a stable lipid bilayer formed spontaneously. To perform FCS measurements on the bilayer membranes, 10  $\mu$ l of the 0.01 mg/ml solution of the Atto 647N labeled phospholipid were added to the S-IV-lipid before evaporation to yield a dye/lipid molar ratio of  $\sim$ 1:50,000.

### STED microscope

I incorporated a standard epi-illuminated confocal microscope for our fluorescence experiments. In short, fluorescence excitation was performed with a 633 nm pulsed laser diode ( $\sim$  80 ps pulse width, LDH-P-635, Picoquant, Berlin, Germany) or a continuous-wave (CW) laser diode (FiberTEC635; AMS Technologies, Munich, Germany). The STED light was supplied by a Titan:Sapphire laser system (MaiTai, Spectra-Physics, Mountain View, CA; or Mira 900F, Coherent, Santa Barbara USA) running at 750-780 nm and with a repetition rate of 76 and 80 MHz, respectively, or the Mira 900F system operated in a CW mode at 780 nm. In case of pulsed irradiation, the repetition rate of the STED laser was taken as trigger for the excitation laser with timing adjustment performed by a home-build delay electronic. The power of the STED laser light was controlled and stabilized by a laser power controller unit (LPC, Brockton Electronics, Brockton, MA) and coupled it into a 120 meter long single-mode fiber (AMS Technologies) for stretching of the pulses to about 250-300 ps. After spatial overlay of both laser beams with appropriate dichroic filters (AHF Analysentechnik, Tübingen, Germany) they were directed on a beam scanning device (mirror tilting system PSH 10/2, Piezosystem Jena, Jena, Germany) and imaged into the microscope (DMIRBE, Leica Microsystems, Mannheim, Germany). An oil immersion objective (PLAPON 60x NA = 1.42, Olympus Japan, or HCXPLAPO NA = 1.4, Leica) was used to focus the laser light to a diffraction-limited spot on the sample and to collect the fluorescence emission. In the case of the horizontal lipid bilayers a water immersion objective (UPLSAPO 60x NA = 1.2, Olympus) was used. The axial position of the focal spots was adjusted by an objective lens positioning system (MIPOS 250, Piezosystem Jena). A doughnut-shaped focal spot with a central zero of the STED light was produced by introducing a phase plate into the beam path, imprinting a helical phase ramp  $\exp(i\varphi)$  with  $0 \leq \varphi \leq 2\pi$  on the circularly polarized wave front [61, 122]. For axial confinement I introduced a phase plate into the linear polarized STED light beam that phase shifted an inner circle of the central wave front incident on the objective lens by  $\pi$  [43, 59, 64] (the beam was again circularly polarized by a  $\lambda/4$  plate in front of the objective). In the case of both lateral and axial phase confinement, the linearly polarized STED beam was split up by a polarizing beam splitter, each divided beam traversed one of the two phase plates, and both beams were again re-combined by another polarizing beam splitter before being

circularly polarized by a  $\lambda/4$  plate in front of the objective. The according powers in the two divided beams and thus in the STED foci for axial and lateral confinement, respectively, were controlled by a  $\lambda/2$  plate in front of the first polarizing beam splitter, as in detail outlined previously [43], and in our experiments split up about evenly. The fluorescence was imaged back over the beam scanning device and coupled into a multi-mode fiber splitter (Fiber Optic Network Technology, Surrey, Canada) with an aperture size corresponding to  $0.8\times$  the magnified Airy disc. The 50:50 split fluorescence signals were then detected by two single-photon counting units (avalanche photo diode SPCM-AQR-13-FC, Perkin Elmer Optoelectronics, Fremont, CA). Potential contributions from scattered laser light or unwanted autofluorescence were blocked by appropriate fluorescence filtering (AHF). The fluorescence counts were further processed by a hardware correlator card (Flex02-01D, Correlator.com, NJ) for FCS and FIDA. I calculated the excitation intensity  $I_{exc} \approx P_{exc}/(\pi \cdot (\text{FWHM}_{exc}/2)^2)$  by measuring the power  $P_{exc}$  incident on the sample and by determination of the diameter  $\text{FWHM}_{exc}$  (full-width-at-half maximum)  $\approx 240\text{nm}$  (oil immersion) or  $330\text{nm}$  (water immersion) of the conventional diffraction-limited focal spot directly measured at a scattering gold bead of sub-diffraction diameter (80 nm gold colloid, En.GC80, BBinternational, Cardiff, UK) on a non-confocal detector (MP 963 Photon Counting Module, Perkin Elmer). The intensity of the excitation light was usually  $25 \text{ kW}/\text{cm}^2$ . For the STED light, I give out the power  $P_{STED}$  incident on the sample. The maximum pulse peak intensity of the focal spot of the STED light can be estimated by  $I_{STED} \approx k \cdot P_{STED}/(\pi \cdot (\text{FWHM}_{STED}/2)^2)/(\tau_P \cdot f)$  with a scaling factor  $k = 1$  for the non-engineered spot and  $k = 0.3$  and  $k = 0.5$  for the focal-engineered spots for lateral and axial confinement, respectively, the focal diameter  $\text{FWHM} \approx 340\text{nm}$  (oil immersion) or  $\text{FWHM} \approx 400\text{nm}$  (water immersion) of the non-engineered spot, the pulse duration  $\tau_P$ , and the pulse repetition rate  $f$ . For calibration of the STED microscope with lateral confinement I have determined the diameters of the effective fluorescence foci by scanning approximately  $20\text{nm}$  large fluorescent crimson beads (Molecular Probes, Eugene, OR) for various STED powers and established the radii (at half-maximum) of the accordingly imaged beads (see figure 1.3b)).

### 3.3 STED FFS in solution

#### 3.3.1 STED Fluorescence Correlation Spectroscopy

In aqueous solution, a single dye molecules diffusing through the confocal detection volume give rise to a burst of fluorescence. The length of the burst varies depending on the diffusion path through the focal spot. Consequently, a decrease in the detection volume introduced by a doughnut shaped STED pattern, should give shorter burst lengths (see Figure 1.3), because the dye molecules pass the smaller effective detection volume faster. In the FCS analysis this should result in a decrease in the lateral diffusion time with increasing  $P_{STED}$ , as can be seen by using equation (1.3.11) and the relation between the beam waist  $w_0$  and the *FWHM*:

$$\tau_{xy}(P_{STED}) = \frac{w_0(P_{STED})^2}{4D} = \tau_{xy}(0) \cdot \frac{1}{1 + P_{STED}/P_{SAT}}, \quad (3.3.1)$$

but should the axial diffusion time  $\tau_z = \frac{z^2}{4D}$  unchanged due to the doughnut shaped form of the STED intensity distribution featuring no intensity along the optical axis. On the same time the decrease in the detection volume  $V$  should lead to a decrease in the average number of molecules  $N$  observed in the measurement. Since the correlation amplitude  $G(0) \sim 1/N$  is inversely proportional to the number of molecules, one should see consequently an increase in the correlation amplitude. The number of particles  $N_{FCS}$  depends analogously to the diffusion time on the STED power  $P_{STED}$ :

$$\begin{aligned} N_{FCS}(P_{STED}) &= c_0 V(P_{STED}) = c_0 \pi^{3/2} w(P_{STED})_0^2 z \\ &= N_{FCS}(0) \cdot \frac{1}{1 + P_{STED}/P_{SAT}} \end{aligned} \quad (3.3.2)$$

Figure 3.1a) shows correlation data recorded for the organic dye Atto 647N in aqueous PBS buffer with and without addition of focal-engineered STED light. The Atto 647N dye was excited with  $\sim 90$  ps long pulses of 633 nm light, swiftly followed by  $\sim 250$  ps long pulses of 770 nm STED light. The STED light featured a doughnut-like intensity distribution with a central zero along the lateral xy-directions (inset figure 3.1). While the FCS data outlines the expected shift towards lower  $\tau_{xy}$ , I observed an unexpected decrease in the amplitude  $G(0)$  with  $P_{STED}$ , meaning an apparent increase in the number of particles  $N_{FCS}$  in the FCS measurement. To analyze the FCS data quantitatively I have fitted the FCS curves to the theoretical autocorrelation curve in equation 2.2.8, with an additional triplet term (see equation 2.2.14). The average triplet population  $T$ , the triplet correlation time  $\tau_T$  and the diffusion time in the axial direction  $\tau_z$  were first determined in the confocal mode and than kept constant in the fitting process for the STED mode, since all those three parameters should not be affected by the STED light<sup>2</sup>. This leaves only the amplitude  $G(0) \sim 1/N_{FCS}$  and the lateral diffusion

<sup>2</sup>This is in a strict sense not true for the triplet parameters, since it has been shown that the triplet manifolds can be depopulated by the incident of a red shifted light[67, 88, 91]. Nevertheless, the robust fitting results as well as the



time  $\tau_{xy}$  as free fit parameters. Figure 3.1b) shows the dependence of  $\tau_{xy}$  and  $N_{FCS}$  on the applied STED power  $P_{STED}$  (compare equations 3.3.1 and 3.3.2). While  $\tau_{xy}$  decreases as expected from 80  $\mu\text{s}$  to 8  $\mu\text{s}$ , a ten fold decrease, the apparent particle number  $N_{FCS}$  actually increases from 1.8 to 3.3 by a factor of 2.3. The decrease in the lateral diffusion time  $\tau_{xy}$  follows nicely the dependence outlined in equation (3.3.1), which gives roughly a 3.3 fold reduction in the lateral beam waist  $w_0$ , corresponding to a  $3.3^2 \approx 10$  fold reduction in the FCS detection volume  $V_{FCS}$ . Since the average dye concentration does not change during the measurements, this should give a corresponding reduction in the number of particles  $N_{FCS} = c_{Dye} \cdot V_{FCS}$ . While there are many possible explanations for the deviation from the theoretical expected behavior of the FCS - data, most probably the FCS analysis is biased due to the rather crude approximation of a 3D - Gaussian distribution for the brightness profile. This is especially true in the case of the downsized detection volume, when measuring in the STED mode. Another possible explanation for the results would be the occurrence of additional background introduced by the STED light, which according to equation 2.2.15 should increase the apparent number of particles. Since this cannot be decided only by using the FCS analysis I have complemented the FCS analysis with FIDA.

### 3.3.2 Fluorescence intensity distribution analysis

According to equation 2.3.18, FIDA is able to distinguish between the background signal  $F_B$  and the actual fluorescence signal  $F = N_{FIDA} \cdot \eta$  stemming from individual fluorophors. Therefore, by recording the photon count histograms along with the correlation data, one should be able to correct the FCS results with FIDA on the same set of fluorescence data recorded for Atto 647N in PBS buffer with increasing power  $P_{STED}$  of the doughnut-shaped STED light. In figure 3.2a) the number of particles  $N_{FIDA}$  as determined by FIDA is plotted against increasing  $P_{STED}$ . For comparison the number of particles as well as the diffusion time estimated by FCS are shown again ( $N_{FCS}, \tau_{xy}$ ) and all values are normalized to one for zero STED power. Additionally, the molecular brightness  $\eta_{FIDA}$  estimated by FIDA is incorporated into the graph, corrected by equation 2.3.23 for high  $P_{STED} > 50\text{mW}$ , since in those cases the diffusion time  $\tau_{xy}$  is smaller than the chosen time window  $T = 40\mu\text{s}$  for the FIDA histogram. Interestingly here, the decrease for the number of particles  $N_{FIDA}$  corresponds well with the decrease of the diffusion time  $\tau_{xy}$  indicating that the number of particles estimated by standard FCS were indeed biased by uncorrelated background (compare equations 3.3.1 and 3.3.2).

The values for  $N_{FIDA}$  and  $\eta_{FIDA}$  were estimated in two different ways out of the measured photon counting histograms:

1. First, the spatial parameters  $a_1$ ,  $a_2$  and  $a_3$  are determined by fitting the histogram for the confocal measurement and are fixed for the histograms at the different STED powers. This

---

probably small effect of the STED light onto the triplet population justifies my approach.

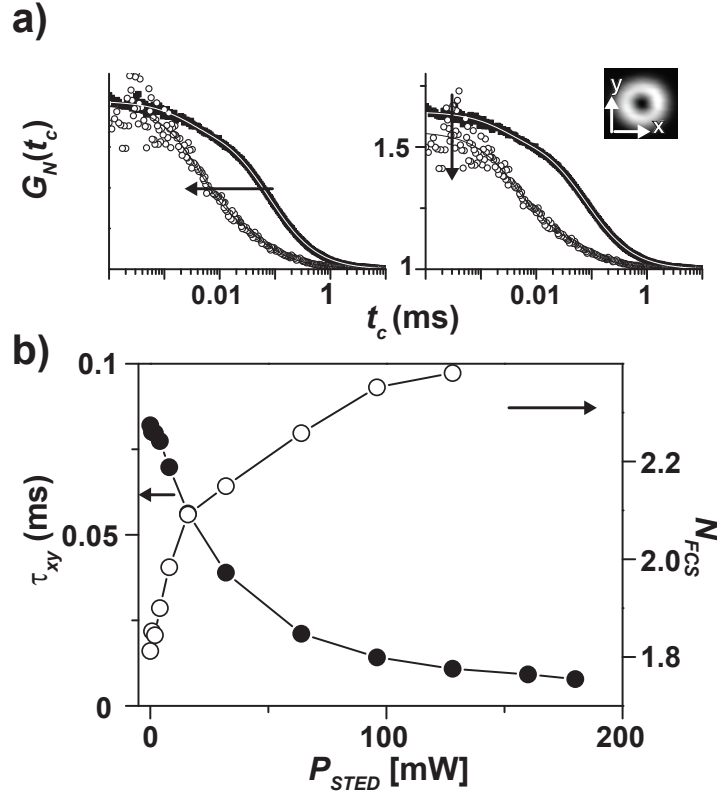


**Figure 3.1: STED FCS in aqueous solution.** **a)** Correlation data  $G(\tau)$  of the dye Atto 647N in PBS at confocal (black circles) and STED recording (open circles) with  $P_{STED} = 50\text{mW}$  (780nm) and the doughnut-shaped intensity distribution (inset, xy - plane) together with fits (grey lines) of equation (2.2.8) to the data: normalization at  $\tau = 0.001\text{ms}$  (left panel) and original data (right panel), showing a decrease of the decay time and amplitude upon focal confinement (arrows). **b)** Dependence of transit time  $\tau_{xy}$  and particle number  $N_{FCS}$  on the STED power  $P_{STED}$  as determined from fitting equation (2.2.8) to the according correlation data. The triplet parameters and the axial diffusion time were fixed to:  $T = 0.14$ ,  $\tau_T = 3\mu\text{s}$  and  $\tau_z = 4\text{ms}$ .

leaves the number of particles  $N_{FIDA}$ , the molecular brightness  $\eta_{FIDA}$  and the background  $F_B$  as free fitting parameters.

2. The uncorrelated background is fixed to a scattering signal of 1 kHz as measured for a dye free PBS buffer solution. The incomplete inhibition of fluorescence is then reflected by a change in the spatial parameters  $a_1$ ,  $a_2$  and  $a_3$ , adapting for the change in the brightness profile  $B(r)$  due to an increase in the fraction of low brightness volume shells.

In both cases either the uncorrelated background or the spatial parameters change significantly with increasing STED power. In the first case, the fit results show a strong increase of the uncorrelated background  $F_B$  up to a countrate of roughly 20 kHz saturating for  $P_{STED} > 20$  mW (figure 3.2b). In the second case, one could observe a strong increase in the fraction of volume shells of low brightness defined by the spatial parameters  $a_1$ ,  $a_2$  and  $a_3$ . The fraction of low brightness volume shells can be determined by integrating equation 2.3.22 for the different spatial parameters depending on the applied STED power. The size of the relative volume shells for a particular brightness are visualized in figure 3.2c) by plotting the normalized volume shells  $V(x)$  against the corresponding normalized brightness values  $B(x) = B(0) \cdot \exp(-x)$  with arbitrary normalizations  $B(0) = 1$  and  $V(x_1) = 1$  at  $B(x_1) = 5 \cdot 10^{-5}$ .

The latter analysis is more rigid, because it explicitly takes into account the change in the brightness profile induced by STED. However, also the first method with an apparently wrong brightness profile is equally able to render good fitting results. Here, the increase in the uncorrelated background adapts for the increase of the fraction of low brightness volume shells. The advantage of the free background method is the greater fitting convergence, which delivers more reproducible results. Therefore, this method was applied throughout the rest of my work.

### 3.3.3 Dependence on experimental conditions

In a previous study Lars Kastrop et. al [59] have reached a 3-5 fold focal confinement by using a STED intensity distribution suited to increase the axial resolution on the dye MR121 in PBS. The improvement of the focal volume confinement in PBS to a factor of  $\sim 10$  shown here can be ascribed to two facts:

1. The dye Atto 647N used in my experiments is brighter and more photostable compared to the dye MR121. Both properties are of decisive importance for single molecule studies[30].
2. The doughnut shaped STED intensity distribution confines the detection volume along both lateral axis while the axial doughnut only reduces the extent of the focal volume along one axes.

Despite those improvements, the measurements are still limited by an increasing fraction of background. In principle, this does not impede more sophisticated FFS measurements, especially if one corrects for this background by a combined FCS - FIDA analysis. Nevertheless, single molecule studies, although

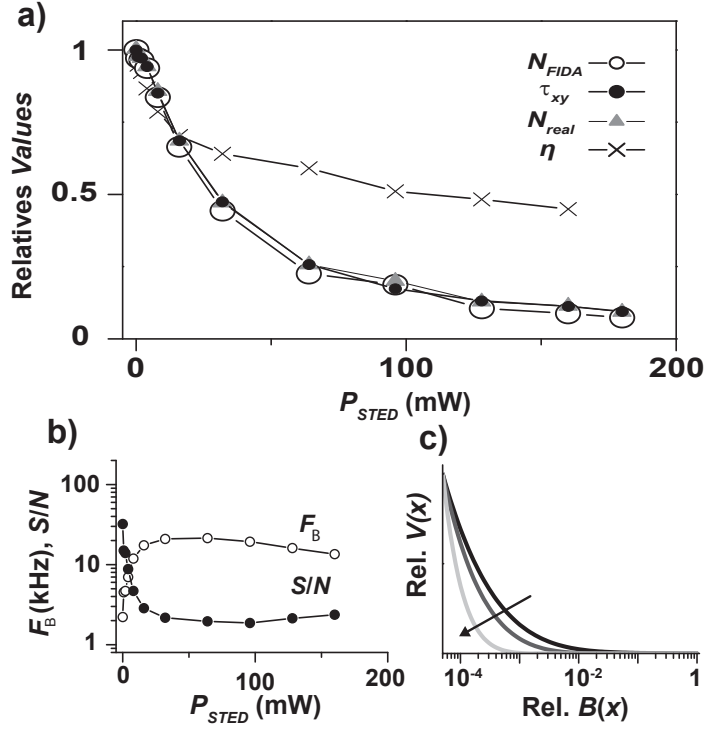


**Figure 3.2: STED FFS of the dye Atto 647N in PBS.** a) Relative dependence of transit time  $\tau_{xy}$ , particle numbers  $N_{FIDA}$  and  $N_{real}$  and the fluorescence brightness  $\eta$  on the STED power  $P_{STED}$  (780nm) as determined from FCS ( $\tau_{xy}$ ), from FIDA ( $N_{FIDA}$ ,  $\eta$ ), and from FCS applying the correction algorithms of equations 2.2.15 ( $N_{real}$ ). b) Dependence of the uncorrelated background  $F_B$  and signal-to-noise ratio  $S/N = \eta/F_B$  on  $P_{STED}$  as determined from FIDA. c) Relative volume size  $V$  of a certain relative brightness  $\eta$  of the focal detection volume, with arbitrary normalizations  $B(0) = 1$  at maximum brightness and  $V(x_1) = 1$  at  $B(x_1) = 5 \cdot 10^{-5}$ , for increasing  $P_{STED} = 0$  mW (black line),  $P_{STED} = 8$  mW (grey line) and  $P_{STED} = 64$  mW (light grey line), depicting a vast increase of volume fractions with low brightness.  $V(x)$  were determined from FIDA applying equation 2.3.22 and  $B(x)$  is determined by the equation  $B(x) = B(0) \cdot \exp(-x)$ .

theoretically still possible with a low signal to noise ratio, are often experimentally impractical due to the long integration times needed to get statistical significant data. Figure 3.2b) shows a drop in  $S/N = \eta/F_B$  from  $\sim 130$  to  $\sim 1.3$  for  $P_{STED} = 160$  mW in aqueous solution due to the volume confinement. Additionally to the increase in background noise, also a reduction of the brightness  $\eta$  for the molecules in the focal center by  $\sim 50\%$  (figure 3.2 a)) weakens the  $S/N$  relation. This is most probably induced by an imperfect intensity zero in center of the doughnut shaped STED distribution inflicted by optical imperfections, mostly resulting from aberrations.

Those aberrations do not impose a principal limit to STED FFS microscopy, since they can be corrected for by, e.g., wavefront corrections, but this can be cumbersome especially for more heterogeneous samples than an aqueous solution. One type of aberrations introduced deliberately into my optical setup stems from the use of an oil immersion objective with a high numerical aperture ( $N_A = 1.42$ ). This is clearly not optimal for the performance of FCS in water solution with a refractive index around  $\sim 1.33$ . The degree of this aberrations is kept as small as possible by performing the experiments close to the surface of the coverslip (less than  $5 \mu\text{m}$  inside the water solution) [49]. I have preferred the oil immersion objective to the water immersion objective, because of the smaller NA of the latter and therefore bigger focal volume from the beginning. But it is in principle possible to do nanoscale single-molecule spectroscopy with a water immersion objective (see figure 3.5).

### 3.3.4 Adaptation of the refractive index

One way to overcome potential negative influence from spherical aberrations is to use 2,2'-thiodiethanol (TDE) as an environment to perform single molecule studies at the nanoscale. TDE is a solvent with an adjustable refractive index in the range of the refractive index for normal immersion oil ( $n \approx 1.52$ ) and has been already used in high resolution microscopy relying on proper phase adjustment [107]. Figure 3.3a) shows the dependence of  $N_{FIDA}$  and the biased  $N_{FCS}$  from the applied STED power  $P_{STED}$  recorded for Atto 647N in TDE. The data was recorded for different types of focal confinement. For the doughnut shaped STED intensity distribution, the same as used for the PBS measurements, the particle numbers  $N_{FIDA}$  and  $N_{FCS}$  initially both decrease as a consequence of an increasing STED power, reflecting an ever smaller focal volume. This decrease continues for  $N_{FIDA}$  even for high STED power and is in good agreement with the confinement estimated by the decrease in diffusion time by FCS ( $\tau_{xy}$  goes down from  $1.2$  ms to  $55 \mu\text{s}$ , a  $\sim 22$  - fold decrease in the focal volume). The obtained values for  $N_{FCS}$  behave differently. They again start to increase for a STED power  $P_{STED} > 20$  mW. Nevertheless, at least for low  $P_{STED}$ , one could observe a decrease in the number of particles for the FCS analysis - a characteristic that was not observable for the experiments in water indicating an improvement in the signal to noise ratio. Therefore, the adaption of the refractive index, leading to a reduction of the spherical aberrations, already improves the performance of the focal confinement by a factor of two ( $\sim 10$  fold volume reduction for Atto 647N in PBS towards  $\sim 22$  fold volume reduction for Atto 647N in TDE). Moreover, although the problem with the uncorrelated background and the

resulting bias in FCS measurement remains still unsolved, at least for high STED power, this problem is far less pronounced for the medium TDE than for water. Unfortunately the overall brightness for Atto 647N is nearly three times smaller in TDE than it is in water (data not shown). This reduction in the brightness and the increase in the uncorrelated background still leads to low signal to noise ratio for high  $P_{STED}$  (small focal volumes, compare figure 3.3c). The lower brightness can partly be explained by the different polarity of the TDE and the water environment, resulting in a lower quantum yield, and the reduced mobility of oxygen due to the higher viscosity of TDE, leading to a reduced quenching of the triple state.

### 3.3.5 Modus of confinement

The same data taken for the doughnut STED modi were also recorded for a STED intensity distribution confining the axial volume (see inset figure 3.3 a), compare [59]) as well as for a combination of both STED modi. In figure 3.3a) the dependence of  $N_{FIDA}$  and  $N_{FCS}$  are shown for the additional focal confinements. In all cases one can observe the same behavior as already seen for the xy - doughnut. The particle number for the FIDA analysis decreases with increasing  $P_{STED}$  while the particle number of the FCS,  $N_{FCS}$ , analysis increases due to an increase in the uncorrelated background (3.3b)). On the same time, both focal confinements lead to a decrease in the molecular brightness  $\eta$  (3.3b)) and an overall vast decrease in the signal to noise ratio  $S/N$ . Yet, slight differences arise from the different modes of focal confinement. The largest focal confinement can be observed for the combination of both STED modi (xyz,  $\sim 25$  fold), the lowest for the z - confinement alone ( $\sim 15$  fold). While one indeed would expect the largest confinement for xyz (3D) STED mode its performance is only slightly better than for the xy - confinement alone. This is most probably due too the rather bad performance of the z STED mode (compare [59]) and the fact that in the case of the xyz STED mode two imperfect zeros are present in the focal center leading to even lower  $S/N$  ratio due to a higher loss of brightness in the focal center.

Further, I have tested the performance of FCS and FIDA at other experimental conditions. Although the focal confinement and single-molecule based dynamical observation in nanoscopic focal spots were realized at all those experimental conditions, I have observed the same uncorrelated background and thus biased signal-to-noise ratios regardless of the choice of excitation light intensity, STED wavelength, or fluorescence inhibition by CW STED light (data not shown).

### 3.3.6 Suppression of uncorrelated low-brightness signal

There are several explanations for the occurrence of the uncorrelated background  $F_B$ , of which some can easily be dismissed. Low brightness contribution due to scattering light from the STED beam or due to excitation via one or multiphoton events by the STED light can be excluded by using an appropriated set of filters (see experimental details). Control measurement of pure water or TDE solution do not show a significant scattering signal for the STED and excitation light ( $< 2\text{kHz}$ ). Direct excitation

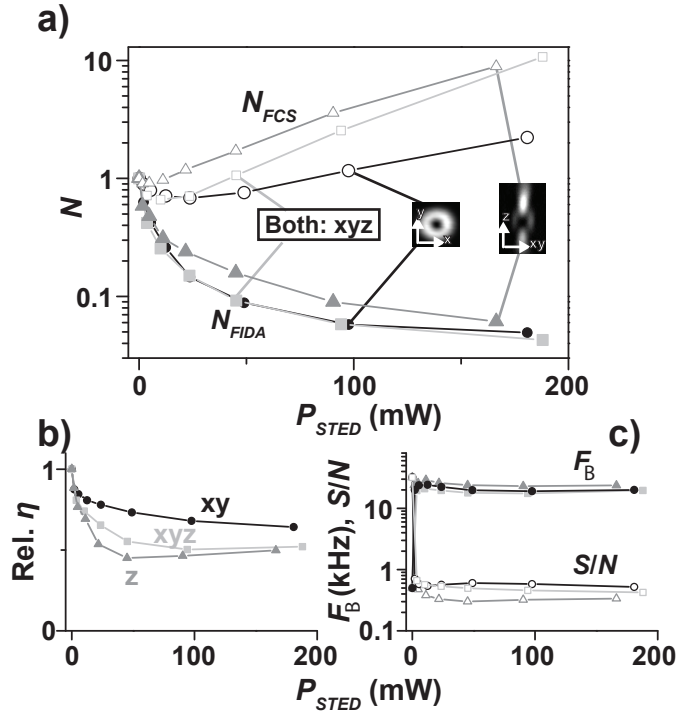


**Figure 3.3: STED FFS of the dye Atto 647N in TDE with different modi of focal confinement by STED.** a) Relative dependence of particle numbers  $N_{FIDA}$  (closed symbols) and  $N_{FCS}$  (open symbols) on the STED power  $P_{STED}$  (780nm) as determined from FCS ( $N_{FCS}$ ) and from FIDA ( $N_{FIDA}$ ) for different focal engineered spots of the STED light: lateral xy-confinement only (black circles) with doughnut-shaped STED intensity distribution (inset), axial z-confinement only (grey triangles) with according STED intensity distribution (inset), and combination of both resulting in a three-dimensional xyz-confinement (light grey squares). b) Relative dependence of the fluorescence brightness  $\eta$  on  $P_{STED}$  as determined from FIDA for the different modi of focal confinement. c) Dependence of the uncorrelated background  $F_B$  and signal-to-noise ratio  $S/N = \eta/F_B$  on  $P_{STED}$  as determined from FIDA for the different modi of focal confinement.

of the dye by the STED light itself is also insignificant ( $<5$  kHz). Moreover I could not observe a scattering peak in the fluorescence lifetime recorded by time-correlated single photon counting (see 2.4) when the STED light is applied during the measurements. In contrast, the measured fluorescence lifetime is identical for the excitation mode alone and for the residual fluorescence in the STED mode staying at a typical value of 3.4 ns and 3.8 ns in water or TDE, respectively.

Another possible source for the low brightness background could be an incomplete depletion of the fluorescence by the STED light in the focal plane. To test for this I have completely overlaid the excitation foci with the slightly larger STED foci without introducing a phase plate into the STED beam and recorded FIDA data for increasing STED power. The idea is to estimate the degree of depletion by extracting the brightness out of the recorded FIDA data. If incomplete depletion in the focal plane is responsible for the background, one would expect that the decrease of the brightness  $\eta$  is closely followed by an equivalent decrease in the total fluorescence  $\langle F \rangle$ . Rather, as can be seen in figure 3.4a), the brightness quickly drops to zero whereas the total fluorescence still shows a residual level of  $>15\%$ . The degree of the residual fluorescence interestingly depends on the size of the confocal pinhole and decreases for smaller pinholes (see figure 3.4a)). Smaller pinholes discriminate stronger against fluorescence out of the focal plane. One can therefore conclude that the spurious background stems from out of focus areas. Unfortunately, it is not possible to eliminate the background contribution from the out of focus region completely by decreasing the pinhole size, because ever smaller pinholes will not only decrease the background signal but on the same time decrease also the molecular brightness of molecules in the focal center, quickly resulting in low signal-to-noise ratios. To sum it up, the optimal choice of the pinhole size for a STED setup is similar to the choice for a confocal setup (see [25] for a discussion of the pinhole sizes in a confocal FCS measurement). All together my results indicate that the background stems most prominently from axial out of focus area where the fluorescence inhibition is incomplete.

However it should be possible to completely suppress the axial out of focus signal by reducing the sample volume to a 2D system such as it is the case for lipid membranes.

### 3.3.7 STED-FFS on lipid membranes

Figure 3.5 shows the result of the FCS and FIDA analysis for a phospholipid covalently labeled with Atto 647N diffusing freely in a multilamellar membrane layer. The measurements were performed with the xy - STED doughnut and the focal center of the excitation beam was positioned directly on the membrane layer. When the STED light was applied the autocorrelation data shows the expected decrease in the diffusion time  $\tau_{xy}$  as well as an increase in the correlation amplitude  $G(\tau)$ . Since diffusion in the axial direction was precluded due to the geometry of the sample, I have fitted my data with a 2D autocorrelation equation (2.2.10) neglecting the axial diffusion time  $\tau_z$ . Different to the previous results, in the case of the multilamellar membranes  $N_{FIDA}$ ,  $N_{FCS}$  and  $\tau_{xy}$  all show a  $\sim 25$  fold confinement of the focal volume from a confocal diameter of  $\sim 240$  nm to roughly 50 nm in



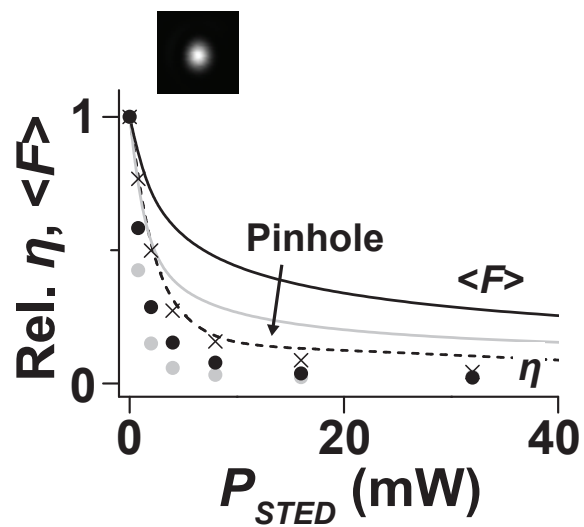


**Figure 3.4: Characteristics of uncorrelated background.** Fluorescence inhibition by the STED light depicted as the relative decrease in total count-rate  $\langle F \rangle$  (lines) and brightness  $\eta$  (circles) of Atto 647N fluorescence in TDE with increasing power  $P_{STED}$  of the STED light (780nm) as determined by FIDA. Depletion of the molecular brightness  $\eta$  is complete; the difference to the total signal  $\langle F \rangle$  stems from unspecific low-brightness signal and decreases with the size of the confocal pinhole (black:  $0.8\times$  and grey:  $1.4\times$  the magnified Airy-disc of the confocal spot) and diminishes when measuring Atto 647N labeled lipids on a multilamellar membrane sheet ( $\eta$ : cross,  $\langle F \rangle$ : dotted line).

the STED modi (figure 3.5 b)). An analysis of the uncorrelated background  $F_B$  by FIDA shows a constant background of  $\sim 1$  kHz irrespective of the STED power, which also explains the unbiased FCS results. This now enables to perform single molecule studies with an excellent signal to noise ratio even at very high STED power  $P_{STED}$ . One advantage of single molecule analysis at the nanoscale is the possibility to use higher dye concentration due to the smaller detection volume. Figure 3.5c) shows the fluorescence time traces for a confocal and a STED measurement at the same membrane layer. Only in the STED mode, bursts stemming from single molecules with an excellent  $S/N$  are identifiable, which are hidden in the confocal time traces (figure 3.5 inset) because of the high dye concentration ( $N > 1$ ).

The methods presented here are not limited to membranes on the surface of the coverslip or to an oil immersion objective. Figure 3.5b) additionally shows the results for an xy - STED modi with a water immersion objective performed on a horizontal supported (black lipid) membrane formed across a small hole in a teflon foil roughly 100  $\mu\text{m}$  above the coverslip. Here again, the uncorrelated background remains negligible even for high  $P_{STED}$  limiting the bias introduced to the FCS analysis.

### 3.3.8 Photobleaching

Due to the high power used for the incident STED light, photobleaching and other adverse effects introduced to the sample are a major challenges for a successful STED application that have to be solved [23, 123]. An earlier concept to limit the negative effect of photobleaching in STED microscopy, especially in the visible range was proposed in [21, 22]. Here, a reduction in the amount of photobleaching and a concomitant increase in the fluorescence signal was reached by eliminating triplet bleaching via a T-REX approach (triplet relaxation due to a low repetition rate of the pulsed excitation ( $< \text{MHz}$ )). Unfortunately, this approach is not feasible for single molecule spectroscopy since the triplet relaxation due the long triplet lifetime ( $\sim \mu\text{s}$ ) needs pulsed laser systems with a low repetition rate ( $\sim \text{kHz}$ ). This leads to low molecular brightnesses and therefore low signal-to-noise ratios.

However, my fluorescence fluctuations analysis is less prone to photobleaching than one might expect, rather it seems that one of the advantage of STED FFS compared to confocal FFS is actually a smaller bias due to photobleaching. Figure 3.6 shows the relative change of the diffusion time  $\tau_{xy}$  measured on a layer of membranes or on the plasma membrane of a mammalian cell for the confocal as well as for the STED mode ( $P_{STED} = 160 \text{ mW}$ ,  $FWHM \approx 40 \text{ nm}$ ) for increasing excitation power  $P_{exc}$ . In both cases the diffusion time for the STED mode is less effected by an increased excitation power than in the confocal mode. The diffusion time in the STED mode on the membrane layers remains unaffected, whereas the STED diffusion time on the plasma membrane drops down to roughly half of its confocal value. The bigger drop for the diffusion time on the plasma membrane can be explained by the fact that the diffusion on the plasma membrane is roughly 5 - 10 times slower than on the membrane stacks ( $\tau_{multi} = 3 - 5 \text{ ms}$  compared to  $\tau_{plasma} = 20 - 30 \text{ ms}$ , data not shown), which in general should increase the degree of photobleaching due to the longer retention time within the

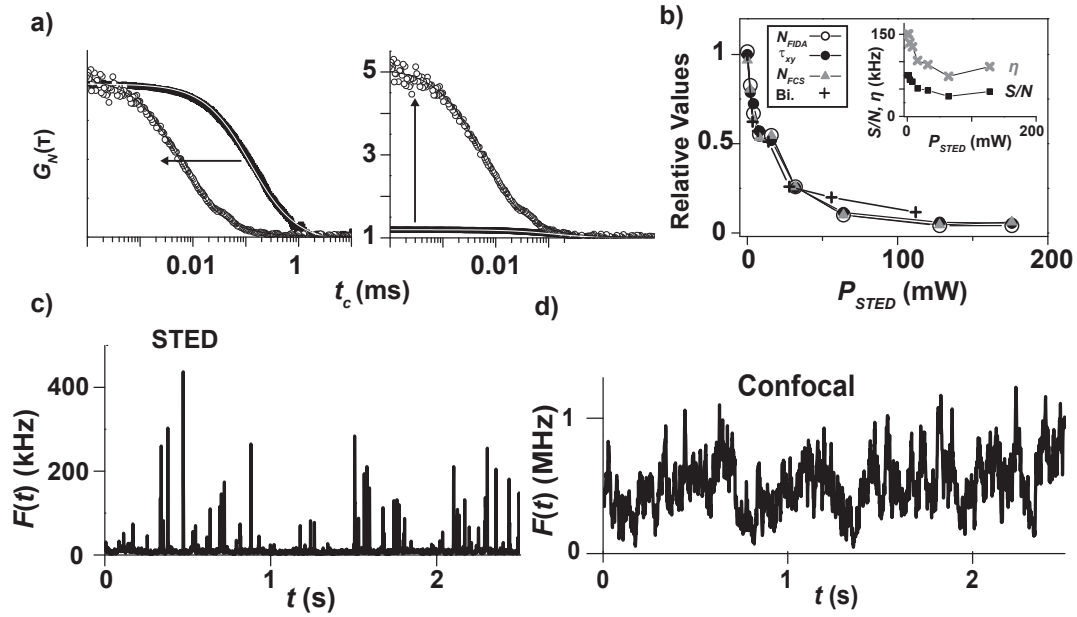


**Figure 3.5: STED FFS on lipid membranes.** (a) Correlation data  $G(\tau)$  of Atto 647N labeled lipid in multilamellar lipid membrane layer at confocal (black circles) and STED recording (open circles) with  $P_{STED} = 50$  mW (780 nm) and the doughnut-shaped intensity distribution together with fits (grey lines) of equation (2.2.10) to the data: normalization at  $\tau = 0.001$  ms (left panel) and original data (right panel), showing a decrease of the decay time along with a rise of the amplitude upon focal confinement (arrows). (b) Dependence of the relative transit time  $\tau_{xy}$  (black circles), the relative particle numbers  $N_{FCS}$  (grey triangles) and  $N_{FIDA}$  (open circles), the molecular brightness  $\eta$  (grey cross inset) and the signal-to-noise ratio  $S/N = \eta/F_B$  (black squares inset) on the STED power  $P_{STED}$  along with the relative decrease of  $\tau_{xy}$  from the measurement on the horizontal membrane bilayers applying a water immersion objective (cross, Bi.). (c) The fluorescence count rate  $\langle F(t) \rangle$  of single Atto 647N labeled lipids diffusing in the multilamellar membrane layer recorded in consecutive time windows of 1 ms with  $P_{STED} = 170$  mW depicts a peak brightness of up to 400 kHz with a signal-to-noise ratio of  $>100$ . (d) For conventional confocal recording, the concentration of Atto 647N labeled lipids is too large for the detection of single isolated molecules, as depicted by the fluorescence time trace of the same sample with the confocal recording. The reduced detection volume by STED enlarges the practical range of fluorophores concentration for single-molecule detection.

focus. This conclusion is supported by the fact that I could not observe a difference between the photobleaching for the STED mode and the confocal mode in the case of freely diffusing Atto 647N molecules in water because the diffusion in this case is already fast enough to even exclude a detectable effect by photobleaching for the confocal mode (data not shown). Therefore, any artifacts which may be introduced into the measurements due to photobleaching by the excitation light is less distinct in the STED mode because of the shorter time span for possible photobleaching[31]. This is definitively a major advantage of STED FFS over confocal FFS.

The second source of possible photobleaching artifacts could stem from the STED light itself. However, this might be, even if present, of minor importance to the concept of dynamical FFS studies, because the bleaching events caused by the STED light occur when the molecules are outside of the detection area and are not supposed to give any information. This is in sharp contrast to excitation bleaching which occur exactly when the dynamics of the molecules are read out. Nevertheless, bleaching if present in the outer region of the detection area, should still effect the number of particle  $N$  able to enter the detection area. In my measurement I could not observe an additional reduction in the number of particle from the STED light by photobleaching, since  $N_{real}$  decreases in good agreement with the decrease in  $\tau_{xy}$  (see figure 3.5c). In principle photobleaching should both reduce  $N$  and  $\tau_{xy}$  differently [31, 120] and therefore one would not expect a congruent reduction of both values with the detection radius. Nonetheless, it is still to early to rule out any effect from photobleaching and therefore in any FFS study the number of particles in the focus should be treated with care.

One possible reason for the absence of effects of STED bleaching in our data is the fact that the rate of photobleaching by STED is usually orders of magnitude smaller than the rate of the competing process of fluorescence inhibition by STED. With typical cross section for stimulated emission of  $\sigma = 10^{-17} - 10^{-16}\text{cm}^2$  [60, 92] compared to the typical cross section of  $\sigma = 10^{-17} - 10^{-16}\text{cm}^2$  for the first excited state of the molecules, from which bleaching due to STED typical occurs[22, 23, 31], combined with the a bleaching probability of  $10^{-8} - 10^{-6}$  from higher electronic states[30, 29], the rate of bleaching should be significantly lower than the rate of STED for the same STED intensities.

Beside artifacts introduced into the measurement by photobleaching the high STED power applied, could in principle show a variety of adverse effects altering the results of the FFS analysis by local heating, radical formation from excited dye states or other changes in the dye kinetic. The proportional decline of the particle number and the diffusion time  $\tau_{xy}$  with the focal radii shown in figure 3.6c) is a strong argument against any light induced bias since such a bias should alter the relation between the particle number and the STED power (see equation 3.3.2).

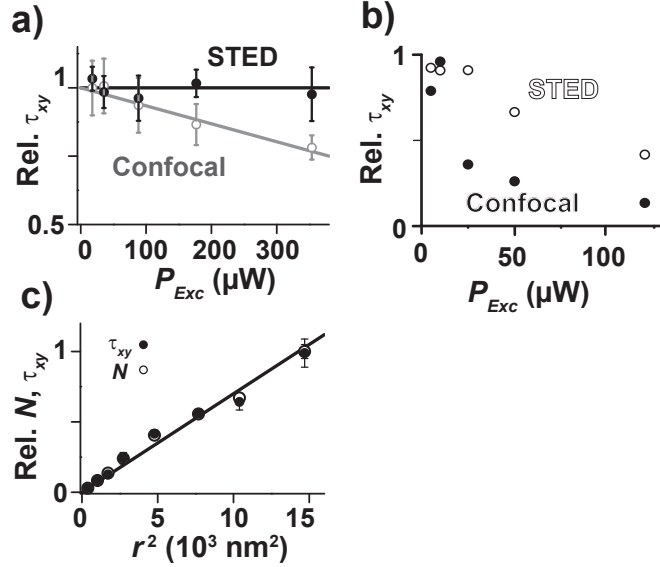


**Figure 3.6: Less bias by photobleaching in STED FFS on membranes.** **a)** Relative decrease of the average transit time  $\tau_{xy}$  of the Atto 647N labeled lipid diffusion in multilamellar membrane layers with excitation intensity  $P_{exc}$  for confocal (open squares) and STED recording (closed squares,  $P_{STED} = 160$  mW). While  $\tau_{xy}$  is reduced down to  $\sim 60\%$  due to photobleaching at confocal recording, photobleaching by the excitation light is negligible for STED recording. **b)** Same results as in a) for Atto 647N labeled lipid diffusion in the plasma membrane of Ptk2 cells (see section 4.2). Here, the diffusion time for the confocal measurements is reduced to  $\sim 10\%$  for high excitation intensities in the confocal mode, compared to  $\sim 50\%$  for the STED mode ( $P_{STED} = 160$  mW). **c)** Relative reduction of the particle number  $N$  (open circles) and average transit time  $\tau_{xy}$  (closed circles) of the Atto 647N labeled lipid diffusion in multilamellar membrane layers with focal area  $r^2$  confined by STED. I determined the values of  $N$  and  $\tau_{xy}$  from FIDA and FCS, respectively, while the radius  $r$  was calibrated for increasing STED power ( $P_{STED} = 0-160$  mW) from according scanning images of  $\sim 20$  nm sized crimson beads (compare figure 1.3b)). All values are normalized to the value determined with the confocal spot. As expected from an ‘ideal’ reduction of the fluorescence spot by STED,  $N$  and  $\tau_{xy}$  decline in proportion to the focal area, according to free diffusion of the lipids. This characteristic is a strong argument against STED light-induced effects other than the spot size reduction.

### 3.4 Conclusion

In this section, I have extended far-field fluorescence observation of single-molecule dynamics to focal volumes with a diameter smaller than 50 nm. Even smaller volumes will be available with optimized laser powers. The signal-to-noise ratio of the nanoscale experiments in three-dimensional open volumes is negatively effected by contributions of (undepleted) low-brightness signal from axial out-of-focus areas, leading to a bias in the FCS analysis. This bias can be avoided by recording the single-molecule data on two-dimensional samples such as membranes showing an excellent signal-to-noise ratios of up to  $\sim 100$  in the measurements presented here. The first part of my study has revealed three major advantage of STED FFS compared to confocal FFS.

1. By reaching the macromolecular scale, it should now be possible to investigate dynamic behavior on length scales, which were up to now not accessible with conventional fluorescence microscopy. This is especially interesting in the field of live cell biology, since for those systems the dynamics of macromolecular complexes are of decisive importance for the organization and function of biological processes in the cell.
2. All in all, photobleaching is a minor problem for STED FFS than for confocal FFS. On the first glance this seems to be a minor technical affair but especially for slow diffusing particles artifacts introduced by bleaching can completely distort the true dynamics of the observed system. An example for that will be given in the second part of my thesis when the hindered diffusion of lipid molecules in the plasma membrane is dissected.
3. Any measurement relying on fluctuation is fundamentally limited by the height of those fluctuations compared to the noise level. Fluctuations are in any macroscopic system in the thermodynamical equilibrium inversely proportional to the square root of the number of particles ( $\Delta N/N \sim 1/\sqrt{N}$ ). Therefore the reduction of the focal volume followed by a reduction of the observed number of particles by STED allows to perform FFS experiments at higher concentrations. Again, this has proved itself of being helpful when experiments are conducted in living cells, since here a control of the concentration of labeled macromolecules is often either difficult or nearly impossible[59, 110]. Further, the range of single-molecule based experiments can be expanded to larger concentrations, a topic that was otherwise been solved through photobleaching large parts of the ensemble[74] or through the use of photo-switchable labels[27].

Combinations of STED microscopy with total-internal-reflection or multi-photon excitation will most probably further reduce the noise from axial out-of-focus areas. Moreover forming sub-diffraction focal spots with photo-switchable fluorescence markers would facilitate single-molecule analysis, since the number of visible fluorophors can be tuned additionally[27]. Finally, one could combine different fluorescence and physical readouts on the nanoscale, such as simultaneous recording of fluorescence intensity, lifetime, anisotropy, color, temperature, force or electrical currents.

## 4 STED Fluctuation Spectroscopy on biological membranes

### 4.1 Introduction

#### 4.1.1 The cell membrane

The plasma membrane of eukaryotic cells contains a large variety of different lipid species, which can be sorted into three different classes: glycerophospholipids, sphingolipids and sterols. The first two classes, while consisting of a range of different lipids, differ only in the headgroups which the two fatty acid chains are attached. Glycerophospholipids are based on glycerin, whereas sphingolipids are based on a ceramide backbone and have either a phosphocholine (Sphingomyelin, SM) or a complex carbohydrate structure headgroup (Glycosphingolipids, e.g. GM1). The ceramide backbone enables the sphingolipids to function as hydrogen bond acceptors and donors, whereas the glycerin is only a hydrogen bond donor[52, 81]. The third class, the sterols, have a completely different structure, formed by a rigid four ring system, with cholesterol being the most ubiquitous in the cell membrane (see figure 4.1 a)). The exact amount of those lipid classes can differ remarkably from cell to cell, but cholesterol is usually in the range of 30-40 mol %[112, 125]. Sphingomyelin is present at 10-20 mol % where as glycosphingolipids are only present in a few specialized cells in a significant amount[106].

Independent of the exact distribution of the lipids, plasma membranes of the cell always form a bilayer structure, with an inner and an outer leaflet, serving as barrier to protect the interior environment from uncontrolled exterior influences. Both leaflets differ in their lipid composition: the outer leaflet contains most of the sphingolipids whereas the inner leaflet is enriched in the phospholipids PI (phosphatidylinositol) and PS (phosphatidylserine)[13]. This asymmetry is sustained by specific membrane proteins actively flipping the lipids from one leaflet to the other[7]. Cholesterol seems to be equally distributed in both leaflets due to its high rate of spontaneous flipping between the two leaflets ( $\sim 1$  s)[76].

Since this high degree of complexity in the organization of the plasma membrane is not a prerequisite for the formation of a stable bilayer, which is already in principle possible with just a single amphiphilic lipid, it has long been proposed that the complexity of the composition of the membrane is reflected in a structured lateral organization of the membrane by macro- and microdomains[13, 105, 111]. Examples for such domains are clathrin-coated pits, caveolae, cilia and microvilli, all containing a specific set of proteins and lipids[39]. Putative 'Rafts' are special kind of microdomains, supposedly enriched in sphingolipids and cholesterol, first argued for by Simons et. al. [105] (see figure 4.1b)). It is assumed that they are distributed over the whole outer leaflet of the plasma membrane, playing a vital role in various important cellular functions such as signalling, cell apoptosis, cell adhesion and migration and synaptic transmission. One proposed way by which 'rafts' succeed in influencing biological processes is by separating the cell membrane into small sub-areas, thereby providing an environment to crowd special proteins in such areas. A prominent and widely studied example are glycosyl-phosphatidylinositol (GPI) anchored proteins, which have been found to be associated with sphingolipid - enriched

domains [39, 103].

Although intensively studied in a large body of work (see [54, 77] for an overview), there is still a controversy as to whether 'rafts' indeed exist and, if so, which exact role they play in the organization and function of the eukaryotic cell. Two of the major obstacles for the direct investigation of 'rafts' in living cells are the highly dynamic nature of the plasma membrane with lipid diffusion coefficients around  $D \approx 5 \cdot 10^{-9} \text{ cm}^2/\text{s}$  leading to observation times of roughly  $\sim 10 - 30 \text{ ms}$  for a confocal fluorescence microscope as well as the possible subdiffraction size of those microdomains ( $< 200 \text{ nm}$ )[54]. These 'raft' properties place great demands on the experimental setup and method used for their investigation, since it has to provide a high spatial - temporal resolution while simultaneously being live cell compatible.

In this part of my work I will show that STED FFS uniquely combines the high temporal resolution (theoretically down to  $\sim \text{ns}$ ) of a fluorescence fluctuation technique with the sufficiently high spatial resolution due to the resolution enhancement by STED (down to  $< 30 \text{ nm}$ ), enabling the investigation of the dynamics of microdomains in the plasma membrane. Moreover as a non invasive far field method I am able to directly apply this novel techniques in living cells under physiological conditions.

#### 4.1.2 The 'raft' controversy

Since 'rafts' were initially proposed[105], a whole range of biochemical and biophysical method have been applied to native as well as artificial model membranes to prove their existence and investigate their properties. The most widely used method for 'raft'-studies is based on the fact that parts of the plasma membrane are resistant to the membrane dissolving detergent triton X-100 at  $4^\circ\text{C}$  and that those parts are enriched in cholesterol and sphingolipids, while phospholipids show no preference. This has led to the conclusion that those resistant parts form small domains in the cell membrane[19, 24, 105]. However it was found out later that this method is prone to many different artifacts, including structural changes in the plasma membrane induced by the unphysiological extraction temperature and by the detergent itself[45]. Because of this one nowadays refers to the membrane content which is found to be resistant to the extraction procedure as DRMs (detergent resistant membranes), thereby acknowledging that those fractions may only partly reflect a physiologically meaningful component of the membrane.

Studies on model membranes in general have shown the ability of bilayers to separate into different phases and form microdomains when the right amounts of cholesterol (20 - 30%) and sphingolipids are present[6, 109]. These microdomains have sizes ranging from the nanoscale[17, 53] to the microscale[6], depending on their lipid content, and are therefore within the reach of a standard confocal fluorescence microscope. Unfortunately, domains of that size are not present in cell membranes, although the amount of cholesterol in the plasma membrane is high enough (30-40%). One caveat associated with such model membrane systems is the inherent need to use a simpler molecular composition than in a real membrane systems. This is especially true for the protein content of native membranes, which



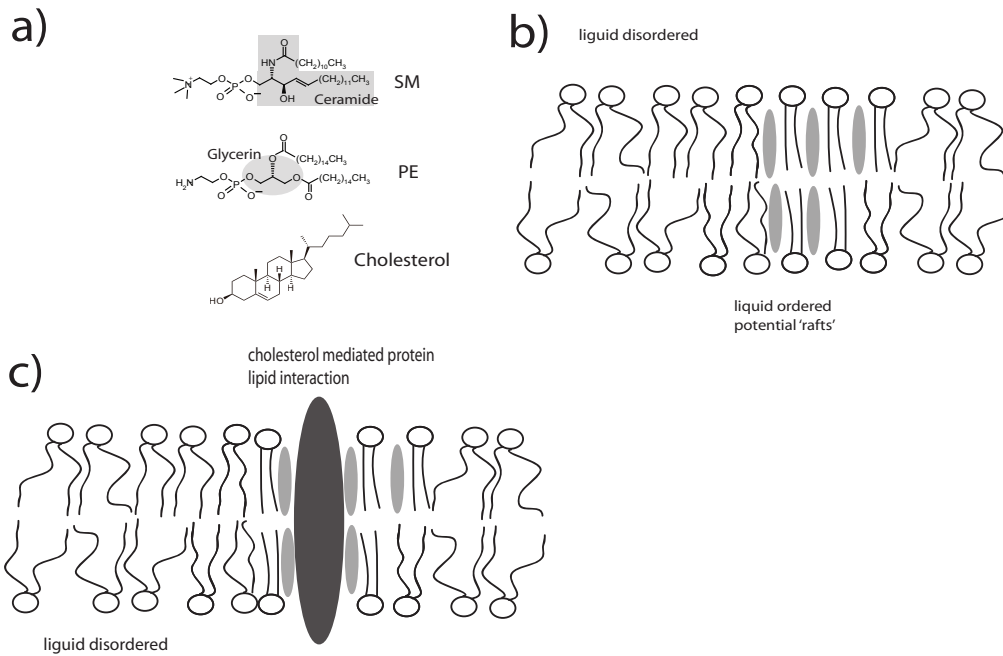


**Figure 4.1: The plasma membrane:** (a) lipid structures of three prominent lipid species, Sphingomyelin (SM, Ceramide backbone (grey shadow)), Phosphoethanolamine (PE, glycerol backbone (grey shadow)) and cholesterol. (b) Scheme of a lipid bilayer with ordered and disordered liquid phases. Cholesterol facilitates the spontaneous formation of ordered phases due to its rigid four ring structure. The ordered phases are supposed to be rich in sphingolipids, whereas disordered phases contain mainly phospholipids. Rafts are proposed to be cholesterol and sphingolipid enriched subdomains. (c) Alternatively sphingolipids could interact with membrane proteins. The interaction is eventually mediated by cholesterol.

according to theoretical consideration might be responsible for the absence of such giant 'rafts' in native membrane systems[127].

In vivo investigations of 'rafts' are usually based on common fluorescence techniques, such as FCS[6, 115], FRET[128] and FRAP[37, 126] or on single molecule tracking[94, 96]. Although it is not possible to review here all results of these studies in detail it is enough to say that they show contradictory results, ranging from findings of heavily clustered lipid protein domains to totally random distributed domain components. Even those studies which found microdomains report widely differing diameters (25 - 700 nm), which can be merely a side effect of the different spatial resolutions of each of these methods[54].

Further, it was shown recently that certain types of lipids interact specifically with membrane proteins by forming lipid shells (see figure 4.1b)[3]. Although the organization of such shells is still unknown, it is highly probable that cholesterol and sphingolipids play an important role in the formation of those entities.

All in all, this is not to say that membrane rafts do not exist in native membranes but that their existence is still speculative and that further investigations are required to either accept or discard the 'raft' hypothesis.

## 4.2 Experimental details

### Cell culture.

The epithelial cell line PtK2 was grown as described previously. For further treatment the cells were seeded on no.1 thickness standard glass coverslips (diameter 25 mm) to a confluence of about 80 %. The cells were grown at 37° C in a water-saturated atmosphere of 5% CO<sub>2</sub> in air. All media and supplements were purchased from Invitrogen (Karlsruhe, Germany).

### Preparation of the BSA-lipid-complex.

I used the organic dye Atto 647N (fluorescence excitation and emission maxima at 645 and 670 nm, respectively; Atto-Tec, Siegen, Germany) as a fluorescence marker in our experiments. N-(Atto 647N)-1,2-dipalmitoyl-sn-glycero-3-phosphoethanolamine (Atto 647N-PE, sometimes simply referred to as PE), N-(Atto 647N)-1,2-dioleoyl-sn-glycero-3-phosphoethanolamine (Atto 647N-DOPE), N-(Atto 647N)-sphingosylphosphocholine (N-Atto 647N-sphingomyelin, Atto 647N-SM, sometimes simply referred to as SM), N-dodecanoylsphingosyl-[N<sup>3</sup>-(Atto 647N)-phosphoethanolamine] (Atto 647N-ceramide-phosphoethanolamine, Atto 647N-CPE) and N-(Atto 647N)-erythro-sphingosine (N-Atto 647N-ceramide, Atto 647N-Cer) were purchased from Atto-Tec. 1-palmitoyl-2-(Atto 647N)-sn-glycero-3-phospho-

ethanolamine (Atto 647N-PE1) was prepared from 1-palmitoyl-sn-glycero-3-phospho-ethanolamine (Avanti Polar Lipids Inc., Alabaster, AL) by protection of the amino group with tert-butoxycarbonyl residue (Boc<sub>2</sub>O, Et<sub>3</sub>N, iPrOH), esterification of the secondary hydroxy group with Atto 647N-COOH (DCC, 4-dimethylaminopyridine, CH<sub>2</sub>Cl<sub>2</sub>) followed by removal of the N-Boc protection (4 M HCl in dioxane, 0° C, CH<sub>2</sub>Cl<sub>2</sub>). The Atto 647N-labeled gangliosides (Atto 647N-GM1 and Atto 647N-GM1<sup>+</sup>, sometimes simply referred to as GM1 and GM1<sup>+</sup>, respectively) were synthesized by a procedure similar to that outlined previously[2, 98]. The lipids differ in their head group structure, the saturation and length of the acyl chains, and the labeling position of the dye, as shown in Figure 4.12. Throughout the text I simply refer to the two main classes of lipids under investigation, i.e., the (fluorescent) phosphoglycerolipids (PE, PE1 and DOPE) and sphingolipids (SM, CPE and Cer as well as the gangliosides GM1 and GM1<sup>+</sup>) as phospho- and sphingolipids, respectively. For comparison, PE and SM were examined with a different dye marker: Atto532-SM (Atto-Tec) and Atto532-SM labeled with the very hydrophilic dye Atto532 (fluorescence excitation and emission maxima at 532 and 553 nm, respectively). Purity of all labeled lipid analogs was proved by chromatography (HPTLC on MERCK SiO<sub>2</sub> plates or RP-HPLC). Complexes of the labeled lipids and Bovine Serum Albumin (BSA) were prepared according to [72, 97], with slight modifications. Briefly, 100 nmol of the lipid stock solutions (CHCl<sub>3</sub>/MeOH, 3:1) were dried under a stream of nitrogen. The dried lipids were dissolved in 20 µl of absolute ethanol and vortexed vigorously after addition of 1 ml of defatted BSA solution (100 µM, i.e., 10<sup>-4</sup> M defatted BSA in Dulbecco's Modified Eagle Medium DMEM without phenol-red buffered with 10 mM HEPES (HEPES + DMEM = HDMEM)). Addition of 9 ml HDMEM results in a final concentration of 10 µM BSA and 0.2 % ethanol. The lipids PE, DOPE, CPE and GM1<sup>+</sup> were prepared in a similar way, except that the BSA concentration was twice as large (2 × 10<sup>-4</sup> M).

#### **Incubation of cells with lipid-BSA-complexes.**

According to the slightly changed protocol of Martin and Pagano[72], cells were washed with HDMEM and incubated with BSA-lipid-complexes on ice for 30 min, washed in cold HDMEM and incubated at 37° C for 4 min in HDMEM (PE, PE1, DOPE, SM and CPE) or directly prepared for observation after washing to prevent internalization (GM1, GM1<sup>+</sup> and Cer). Different concentration of BSA-lipid-complexes were applied for incubation on ice depending on the lipid type and measurement mode: 0.3–0.5 µM (SM) and 1–3 µM (PE) for imaging and 5–50 nM (GM1, SM, PE1), 10–300 nM (PE, DOPE), and ~5 µM (CPE, GM1<sup>+</sup>) for single-molecule analysis and FCS.

#### **Glycosylphosphatidylinositol (GPI) anchor.**

The nanoscale dynamics of a GPI-anchor were observed using an Atto 647N-labeled GPI-anchor in the plasma membrane of PtK2 cells. For labeling, an acyl carrier protein (ACP) tag (Covalys Bioscience, Witterswil, Switzerland) was applied. 24 hours after transfection PtK2 cells expressing GPI-anchored

ACP (pAEMXT-ACPwt-GPI plasmid, Covalys) were incubated for 30 min at 37° C in complete medium supplemented with 5  $\mu$ M CoA-Atto 647N (AttoTec; CoA: coenzyme A), 5 mM MgCl<sub>2</sub> (Fluka) and 1  $\mu$ M ACP Synthase (Covalys). Afterwards, cells were washed three times and prepared for measurements using a medium containing no phenolred.

#### **Treatment with Cholesterol oxidase and $\beta$ -cyclodextrin.**

To modify the cholesterol content of the plasma membrane, cells were either treated with 1 U/ml Streptomyces spec. cholesterol oxidase (COase, Sigma, stock solution 34 U/ml in 50 mM KH<sub>2</sub>PO<sub>4</sub>, pH 7.5) in HDMEM (and washed afterwards in HDMEM) or with 10 mM  $\beta$ -cyclodextrin ( $\beta$ -CD) (Sigma) in HDMEM (without phenol red) for 30 min at 37° C. The COase or  $\beta$ -CD treatment was either performed before or after the insertion of the fluorescent lipid analogs into the plasma membrane.

#### **Measurements.**

The coverslips were mounted in a special microscope chamber (RC-40, Warner Instruments, Hamden, CT). This chamber together with an objective heater (Biotech Inc., Butler, PA) allowed for a precise control of the samples temperature. The lipid dynamics were analyzed in the lower plasma membrane facing the coverslip and all measurements were completed before significant internalization or any morphological changes in the cell could take place. Most measurements were performed at 37° C. Some results were obtained from experiments at 27° C. These experiments comprised the gathering of data for statistical evaluation. Lipid internalization and cholesterol recovery after depletion (by, for example, COase) is faster at 37°C, leaving a smaller time window for sufficient measurements compared to 27°C. Further, the optical performance of the microscope (with regards to optical aberrations) was slightly better at 27°C, allowing for more precise measurements in focal spots with diameter below 40 nm. Nonetheless, within our experimental accuracy, the lipid dynamics hardly alter by changing the temperature from 37°C to 27°C. Apart from a slight slowdown of free diffusion (diffusion coefficient  $D = (5 \pm 2) \cdot 10^{-9} \text{cm}^2/\text{s}$  at 27°C compared to  $D = (6 \pm 2) \cdot 10^{-9} \text{cm}^2/\text{s}$  at 37° C), sphingolipid trapping remains unchanged ( $\tau_{\text{trap}} \approx 10$  ms and  $A_2 \sim 60$  % at both 27° C and 37° C in the case of Atto 647N-SM), and at both temperatures sphingolipid trapping is abolished upon COase and  $\beta$ -CD treatment. Nanoscale dynamics of the GPI-anchor were observed at 24° C.

Diffusion of non-integrated lipids (or dye tags) were excluded by control measurements in between the cells.

#### **STED microscope**

see subsection 3.2.

## Single molecule analysis

As outlined in subsection 2.4 single photon information was collected to perform single molecule fluorescence analysis. For every photon, the macro time, the time between two consecutive photon events, is stored. This allows a time trace of fluorescence bursts to be built up with a chosen time window size. The fluorescence burst were subsequently selected according to the procedure described in subsection 2.4 and only bursts with more than 50 photons were finally accepted. Out of these burst frequency histograms were created by plotting the burst duration against the burst count rate. Burst count rate was calculated by dividing the number of photons per burst by the burst duration. The duration was determined by establishing the temporal full-width-at-half-maximum from a separate fluorescence count time trace with a time window of 0.25 ms set up only for the photons selected for the according burst. There is a certain probability that a fluorescence burst might be caused by more than a single molecule, depending on the concentration of fluorescently marked molecules[36, 40]. Therefore concentration was kept as low as possible to prevent multi molecule events. Nevertheless, especially in the case of the long fluorescence burst due to trapping events for SM one cannot exclude such events. This can explain the slight increase in the count rate of the fluorescence bursts with long burst duration as observed in figure 4.3e).

## Fluorescence Correlation Spectroscopy

The details for deriving an expression for the autocorrelation curve is given in subsection 2.2. For fitting the recorded correlation data the following model was used:

$$G(\tau) = G_{Diff} + G_{Triplet} + G_{kinetic} \quad (4.2.1)$$

$G_{Diff}$  accounts for the diffusion of the lipids in the plasma membrane (see equation 2.2.10),  $G_{Triplet}$  describes the triplet kinetics of the dye (equation 2.2.14) and  $G_{kinetic} = K \cdot \exp(-\tau/\tau_K)$  had to be introduced to account for an additional kinetic term seeing in the data. The individual component of the autocorrelation curve were added instead of multiplied (compare equation 2.2.13) to get faster and more stable fitting results. This approximation is valid as long as the individual component of the autocorrelation curve have correlation times differing at least in one order of magnitude. At the excitation intensities applied, the triplet amplitude  $T_{Triplet}$  and the triplet lifetime  $\tau_T$  were 0.1 and 5  $\mu$ s, respectively and the additional kinetic term had an amplitude  $K$  of 0.05 - 0.1 and a correlation time  $\tau_K$  of 50-150  $\mu$ s. The triplet values were fixed and the kinetic term was ensured to stay in the given boundaries. Most probably the kinetic term stems from an additional dark state of the dye molecule or from conformational fluctuations of the lipid-dye system, leading to a change in brightness.

The two dimensional diffusion model for one freely diffusing species is not adequate to describe the diffusion behavior of sphingolipids for small detection areas. Therefore, in this cases the factor  $G_{Diff}$  in the autocorrelation curve has to be modified by introducing either hindered diffusion (see equation

2.2.12) or by including two dissimilar modalities of diffusion (see equation 2.2.11). Both models give a good parametrization for the deviation from free diffusion.

In the case of two distinct focal spot traversing events, with amplitudes  $A_1$  and  $A_2$  and traversing times  $\tau_{D1}$  and  $\tau_{D2}$ , respectively. The brightness was assumed to be equal for both types of transit (free or hindered, compare figure 4.2). Therefore,  $A_1$  and  $A_2$  directly give the corresponding fractions of molecules, with  $A_1 + A_2 = 1$ . While fitting the data with two diffusion times,  $\tau_{D1}$  was chosen to depend linearly on the size of the detection area, with a diffusion coefficient derived from the corresponding phospholipid measurement, and  $\tau_{D2}$  was a free parameter describing the hindrance of lipid diffusion.

Alternatively, the same data were fitted by an anomalous diffusion model, introducing a new parameter  $1/\alpha$  to account for the degree of hindrance. High values of  $1/\alpha$  indicate more trapping than smaller values, whereas a value of 1 for  $1/\alpha$  means free diffusion. Although the latter being in principle the more accurate way of fitting the data, both models provided a sufficient fit accuracy.

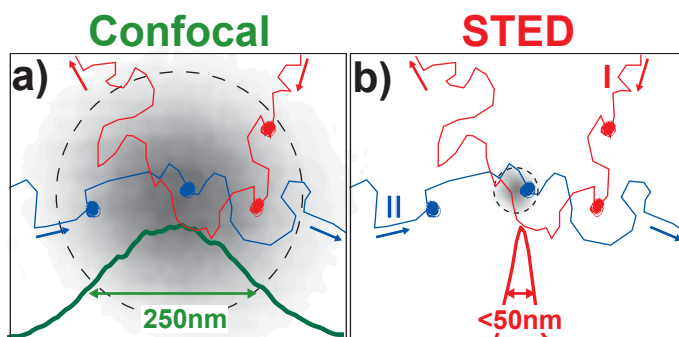


**Figure 4.2: Heterogeneous sphingolipid diffusion in the plasma membrane using STED microscopy.** a,b) Sphingolipids moving through the plasma membrane are transiently trapped on small spatial scales. While the large detection area (diameter  $d \approx 250$  nm) of a confocal microscope is too large to distinguish between locally hindered and unvaryingly slower diffusion a), the small ( $d < 50$  nm) spot created in STED microscopy b) is able to discriminate between lipids that diffuse freely (I) and those which are hindered (II) during their passage.

### 4.3 STED FFS on cell membranes

#### 4.3.1 Lipid Diffusion in the cellular plasma membrane on a nanoscale

Following earlier discussion, unlike phospholipids, sphingolipids are supposed to integrate into  $<200$  nm sized microdomains (assisted by cholesterol) or form molecular complexes, supposedly altering their diffusion in the plasma membrane[85]. Confocal microscopy, limited in resolution by diffraction, averages over such kinds of diffusion as is illustrated in figure 4.2a) whereas STED microscopy, due to its enhanced resolution (see equation 1.3.11), is able to distinguish between differences in the diffusion behavior occurring on spatial scales below the diffraction limit, for example, both free diffusion (I) and hindered diffusion with a trapping event (II) as can be seen in figure 4.2b).

*Lipid Diffusion: Single molecule Analysis* To test whether STED microscopy is indeed able to observe differing diffusion behavior of lipids on the nanoscale I have incorporated the sphingolipids sphingomyelin SM and ganglioside GM1, as well as the glycerophospholipid phosphethanolamine PE, all labeled with the dye Atto 647N, into the plasma membrane of the mammalian cell line Ptk2 (see experimental details). At this stage the question as to whether the labeled lipids are able to mimic the native behavior of the respective lipids is still open. In subsection 4.3.3 I am going to argue why this is indeed so, but here I simply assume this to be the case. Figure 4.3 shows the fluorescence bursts of dye labeled lipids crossing the focal spot. The focal spots in the confocal mode and in the STED

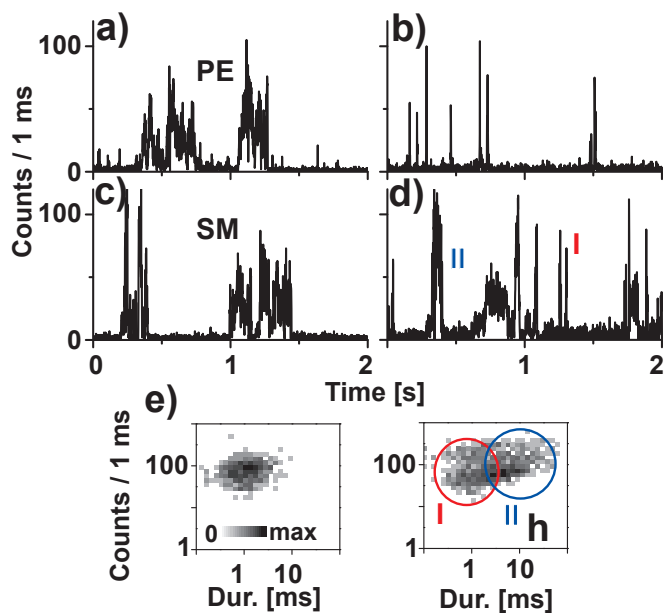


**Figure 4.3: Single molecule study of heterogeneous lipid diffusion with STED.** Fluorescence bursts from single diffusing Atto 647N-labeled PE (a) and SM (c) lipids detected with a confocal setup show no significant difference in height and duration. In the STED recording ( $d \approx 40$  nm), the bursts from PE (b) and SM (d) are markedly different. The PE bursts are shorter in duration, indicating free diffusion, while the SM bursts display molecular transits with both short durations (I) similar to PE, and with longer durations, indicating hindered diffusion (II). (e) Hindered diffusion is further exhibited by the frequency plot of the value pairs of fluorescence counts per millisecond and duration (Dur.) of selected bursts for Atto 647N-labeled PE (497 bursts) and SM (539 bursts). SM transits as fast as those of PE (I) and prolonged transits (II) become apparent.

mode were arbitrarily placed on the plasma membrane. Single molecule concentrations was assured by sparse labeling of the cell membrane, which had the additional advantage that the natural composition of the membrane is not significantly altered upon labeling.

The molecular time traces for PE were recorded for the confocal and STED mode, showing in both cases, clearly distinguishable fluorescence bursts with good signal to noise ratio, as expected for both modes due to the two dimensional nature of the plasma membrane (see figure 4.3a,b)). Moreover, it additionally demonstrates that single molecule studies are possible with a STED microscope in living cells. The burst in the STED mode for PE are uniformly shorter as compared to the burst in the confocal mode, accounted for by the reduction of the focal transit time  $\tau_{xy}$ , but show only, if at all, a small reduction in the burst height. In the case of SM a reduction of the duration can be observed only for some of the fluorescence bursts. In addition one can clearly identify a second type of molecular



transit with a significantly longer burst duration in the STED mode (see figure 4.3c,d). The existence of the two types of molecular transits, as revealed by the STED mode for SM, are hidden in the confocal mode, where the time traces of both lipids are qualitatively indistinguishable.

To account quantitatively for the heterogeneous diffusion behavior of SM, I recorded several time traces in the STED mode and plotted a frequency histogram displaying the number of counts along with the burst duration (see section 2.4 and experimental details) for about 500 bursts recorded for PE and SM. The frequency histogram of PE is characterized by burst durations around  $\sim 1$  ms and no obvious heterogeneities or burst duration longer than 10 ms are visible. The frequency histogram of SM, however exposes a broader distribution of burst durations ranging from short burst similar to the one for PE to long burst with burst durations up to 50ms. This indicates that the SM molecules, beside a PE like molecular transit, also feature an additional molecular transit with longer passing times through the focal area.

*Lipid diffusion: Fluorescence Correlation Spectroscopy* To gain more insight into the details of the molecular transit through the detection area I applied Fluorescence Correlation Spectroscopy, taking advantage of the possibility to average over many molecular passages and thereby revealing typical characteristics (a description of the fitting routine is given in the experimental details). The decay of the correlation curve yields the average molecular transit time through the focal area depending on the applied STED power (see equation 3.3.1 and figure 1.3).

Figure 4.4a) shows a slightly longer diffusion time in the confocal mode for the sphingolipid SM than for the phospholipid PE, while both correlation curves are perfectly described by a diffusion model featuring one transit time (30 and 20 ms, respectively). Therefore, one cannot determine whether the prolongation in the transit time of SM stems from heterogeneities in the diffusion on a subdiffraction length scale or whether it is simply due to a smaller diffusion constant for SM compared to PE. This is remarkably different in the case of STED (see figure 4.4b)). Here, the correlation curve for SM is only describable by a diffusion model assuming at least two components or, alternatively, anomalous diffusion (see section 2.2), whereas the PE curve is still sufficiently well described by a model with a single normal diffusing species. Apparently this second diffusion component can be reduced by depleting the cholesterol content of the cell as can be seen in figure 4.4c), where the correlation curve for SM is significantly shifted to shorter correlation times due to the treatment with Cholesterol Oxidase (COase, see experimental details). As a result, the diffusion of SM is now similar to that of PE, indicating a freely diffusing sphingolipid SM.

*Lipid diffusion: Tuning the focal diameter*

One nice feature of a STED microscope is the ability to seamlessly tune the diameter  $d$  of the STED focal area  $d^2$  (by varying the STED power) from 250 nm down to 30 nm (see equation 1.3.11 and figure 1.3). This allows one to measure the dependence of the transit time  $\tau_D$ , the fraction of slowly diffusing

molecules  $A_2$  and the anomalous factor  $1/\alpha$  on the focal diameter, giving a hint as to the length scale at which the heterogeneities in the SM diffusion take place.

In figure 4.5 the results are shown for both, the two species model as well as for the anomalous diffusion model for SM, and for the one species diffusion model for PE. The heterogeneous diffusion of SM becomes apparent around a focal diameter of around 160 nm (before that the SM correlation curves are still well described by a one-component diffusion, data not shown) and is significant for focal diameters below 60 nm. The focal transit time for PE scales linearly with the focal diameter, which would be expected for a freely diffusing molecules (see equation 3.3.1), resulting in a diffusion constant of  $D = 5 \cdot 10^{-9} \text{ cm}^2/\text{s}$  (since  $\langle r^2 \rangle = 4D \cdot \tau_D$ ) for PE. The total decrease in the diffusion time corresponds to a  $\sim 70$  fold decrease of the focal volume. In the case of SM, for a focal diameter  $< 80$  nm I first fixed the shorter diffusion time  $\tau_{D1}$  to the one of PE, assuming that freely diffusing SM shows the same dynamic behavior as PE (see figure 4.5a)). This leaves the second diffusion time  $\tau_{D2}$  and the fraction of slower diffusing molecules  $A_2$  as independent parameters. Interestingly,  $\tau_{D2}$  begins to level off for focal diameter smaller than 60 nm, reaching a plateau of  $\sim 10$  ms, becoming seemingly independent of further reduction of the focal volume. Moreover, the plot in figure 4.5b) shows that roughly 60% of all SM molecules are transiently trapped during their passage of a focal spot with a diameter  $< 60$  nm.

From the average trapping period  $\tau_{D2}$  one can approximate the average trapping  $\tau_{trap} = \tau_{D2} - \tau_{D1}$  time by subtracting the free diffusion time  $\tau_{D1}$  (see figure 4.5a)), assuming that the passage of the focal spot consist of a freely diffusing part and eventual trapping events. Since the trapping period  $\tau_{trap}$  levels off for  $d < 50$  nm, one can assume that in those spot sizes only one trapping event occurs on average. This is different for larger focal areas (see also figure 4.7), because for  $d > 60$  nm the trapping time plus the diffusion time of PE is slightly smaller than the diffusion time of SM indicating up to two trapping events for larger spot sizes. The low number of trapping events for large focal areas close to the diffraction limit, as compared to the  $\sim 70$ -fold smaller areas formed by STED, seems to be surprising, but can be explained by photobleaching as I will argue in subsection 4.3.4.

The alternative approach of describing the hindered diffusion of SM by a diffusion model with an additional parameter accounting for the degree of hindrance delivers qualitatively the same results (see figure 4.5c,d)). The anomaly parameter ( $1/\alpha$ ) for PE is around  $\sim 1$ , indicating free diffusion where as ( $1/\alpha$ ) is  $> 1$  for SM and GMI due to trapping of those lipids during the passage through the focal area. Note, that also in this case a significant difference between PE and SM is only clearly visible for focal diameter  $d < 60$  nm.

#### *Lipid diffusion: Role of Cholesterol*

As already mentioned, a treatment of the cells with cholesterol oxidase (COase) abolishes the trapping of SM. This is visible by a shortening of the average diffusion time  $\tau_D$ , now nicely following a linear relationship with regard to the focal diameter comparable to the behavior for the diffusion time of PE

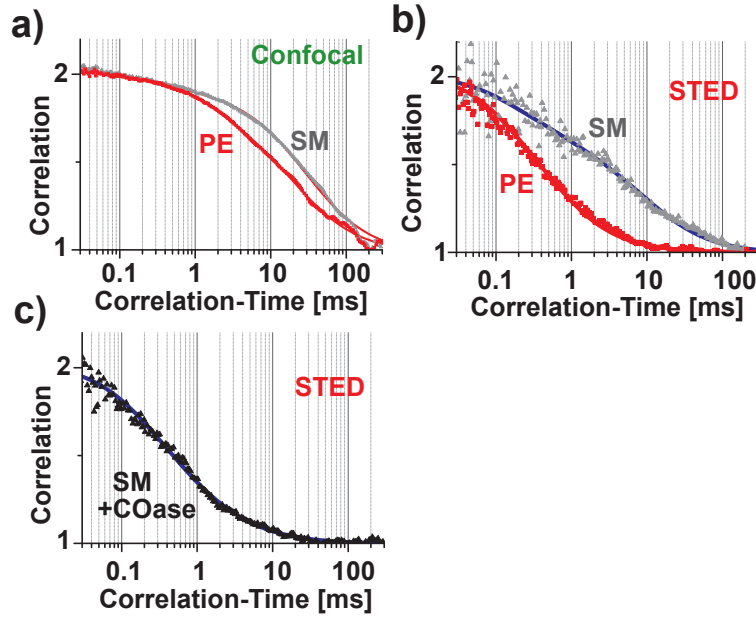


**Figure 4.4: Fluorescence Correlation Spectroscopy of Atto 647N-labeled PE and SM plasma membrane diffusion.** **a)** Normalized confocal correlation data of PE (red dots) and SM (grey dots). The red lines show a single-species fit of the PE and SM data with transit times of  $\tau_D = 19$  and 28 ms, respectively. The confocal recording does not reveal whether the slightly prolonged focal transit time of SM is due to transient local trapping or just due to slower diffusion. **b)** Normalized STED correlation data ( $d \approx 40$  nm) of PE (red dots) and SM (grey dots). Compared to the confocal data, the PE data recorded with STED is significantly shifted to shorter correlation times following the reduction in detection area. In comparison to the PE data, the SM correlation curve observed in the subdiffraction spot shows a shift to longer time scales due to hindered diffusion. The red line shows a single-species fit to the PE-data ( $\tau_D = 0.45$  ms) and the blue line a fit assuming two dissimilar modalities of focal transits to the SM data ( $\tau_{D1} = 0.45$  ms,  $\tau_{D2} = 10$  ms and  $A_2 = 64$  %, see equation 2.2.11). **c)** Normalized STED correlation data of SM with addition of COase (black dots), showing a shift to shorter time scales under addition of COase; SM now diffuses as fast as PE. The blue line shows a fit assuming two dissimilar modalities of focal transits of the COase data ( $\tau_D = 0.45$  ms,  $\tau_D = 4$  ms and  $A_2 = 15$  %).

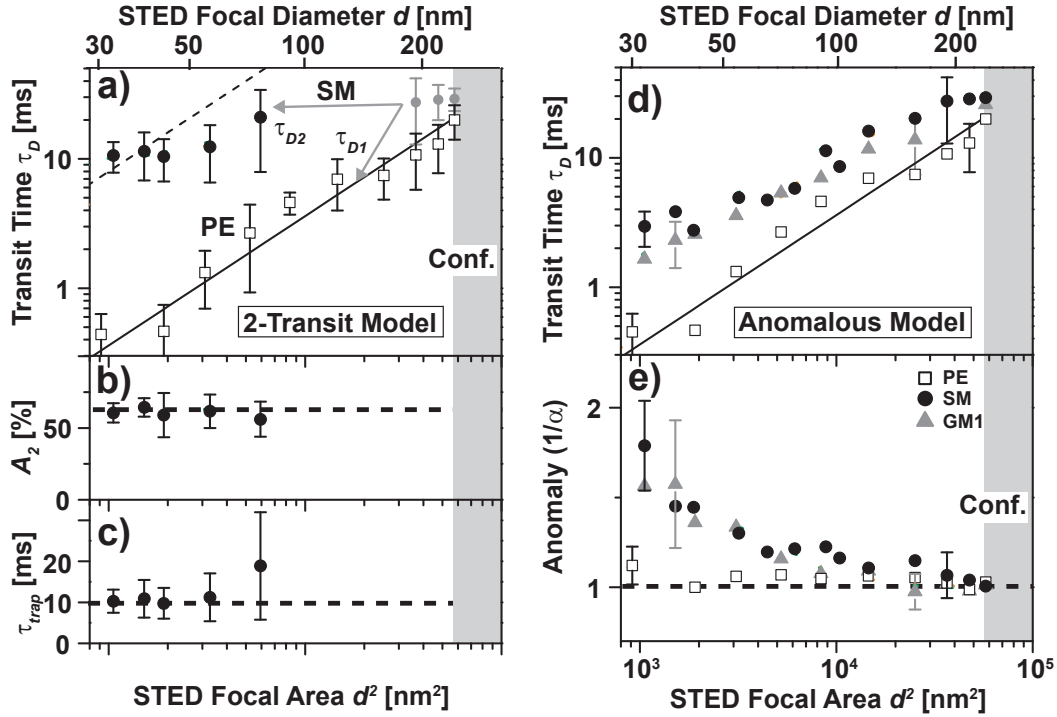


**Figure 4.5: Results from Fluorescence Correlation Spectroscopy analysis of the Atto 647N-labeled lipids PE, SM and GM1 in focal areas dynamically reduced down to 30 nm in diameter formed by STED.** a-c) Model of two distinct modalities of focal transits: a) The transit times  $\tau_D$  determined for PE (open squares) decrease linearly with the focal area  $d^2$ , confirming free diffusion (solid line,  $D = 5 \cdot 10^{-9} \text{ cm}^2/\text{s}$ ). While the SM correlation data found in large focal areas can be described by a single (and compared to PE by 1.5–2.5-fold longer) transit time  $\tau_D$  (grey dots), two transit times  $\tau_{D1}$  and  $\tau_{D2}$  are necessary to describe the correlation data of SM for small detection areas (grey arrows), with one transit time  $\tau_{D1}$  being equal to the transit time of freely diffusing PE (solid line). The other transit time  $\tau_{D2}$  is  $> 10$  fold larger than that for free diffusion (black dots), demonstrating hindered diffusion. A free diffusion that is slower than that of PE would follow a different behavior (dashed line for  $D = 2 \cdot 10^{-10} \text{ cm}^2/\text{s}$ ). b) In the range  $d < 60$  nm, the fraction  $A_2 \approx 60$  % of the SM transits characterized by hindered diffusion is independent of the detection area. c) Trapping time  $\tau_{trap}$  of hindered diffusion of SM calculated from  $\tau_{D2} - \tau_{D1}$  for  $d < 70$  nm. The determination of  $\tau_D$ ,  $A_2$  and  $\tau_{trap}$  becomes inaccurate for  $d > 60$  nm and is impossible for diffraction-limited detection areas (grey shaded area). d-e) Model of anomalous diffusion: Average transit time  $\tau_D$  d) and anomaly ( $1/\alpha$ ) e) of PE (open squares), SM (black dots) and GM1 diffusion (grey triangles). While PE diffuses normally (straight line,  $D = 5 \cdot 10^{-9} \text{ cm}^2/\text{s}$ ), SM and GM1 diffusion is anomalous, as revealed by downsizing  $d$  through STED. Typical error bars are exemplary given, resulting from averaging over more than thirty FCS measurements on different cells.

(see figure 4.4c) and figure 4.6a)). On the other hand the diffusion time of PE is unaltered by the COase treatment. Nevertheless, the diffusion of SM remains anomalous (see figure 4.6b)), indicating, probably, some remaining trap events due to an incomplete depletion process or artifacts introduced by the rather harsh treatment of the cells with COase. To further investigate the remaining heterogeneity in the diffusion of SM and to exclude possible artifacts of the COase treatments of the cells, I additionally depleted cholesterol with  $\beta$ -cyclodextrin (see [87, 78] for a discussion of the problems involved with the depletion of cholesterol in cell membranes by cholesterol oxidase and  $\beta$ -cyclodextrin). As can be seen in figure 4.6c) the depletion of cholesterol by  $\beta$ -cyclodextrin effects the diffusion time of SM and PE in a manner similar to that observed for the depletion by COase (see figure 4.6 c)). Interestingly, in the case of  $\beta$ -cyclodextrin also the heterogeneity of the SM diffusion seems to disappear (see figure 4.6d)). As to whether this is an artifact of the  $\beta$ -cyclodextrin depletion or a result of a more thoroughly depletion of cholesterol remains speculative.

#### *Lipid diffusion: Confocal mode*

In figure 4.7 the diffusion time for focal diameters from 160 - 240 nm is depicted for both PE and SM. The difference between the diffusion times of both lipids is used to estimate the trapping time  $\tau_{trap}$ , which interestingly first increases due to the higher probability of more than one trapping event but then decreases again when reaching the confocal mode, because now the SM diffusion time is no longer determined by the number of trapping events or the free diffusion in between, but predominantly by the observation time depending on the bleaching probability. This again shows the importance of the reduced observation time in the STED mode, which, in combination with the higher spatial resolution, enables the observation of the trapping events for SM without bleaching artifacts. Still, one has to be careful not to use too high excitation intensities to generally avoid any artifact due to bleaching (for a more detailed discussion regarding the influence of bleaching see section 4.3.4).

#### *Lipid diffusion: ganglioside GM1 and Glycosylphosphatidylinositol (GPI) anchor*

A second sphingolipid associated with the formation of microdomains is the ganglioside GM1. Not surprisingly it shows a comparable diffusion behavior to SM, as depicted in figure 4.8. The trapping time is around  $\sim 11$  ms with 45% of the molecules trapped for focal spots smaller than 60 nm. Depletion of cholesterol has the same effects as already described for SM.

Moreover, I have observed trapping for the transfected glycosyl-phosphatidyl-inositol (GPI) anchor indicating that those lipid anchors undergo trapping events in the plasma membrane, similar to that of the sphingolipids (see figure 4.9). GPI-anchored proteins are well known to undergo ‘raft’-like interactions in the plasma membrane and have been implicated in playing a role in many important cellular functions (see for example [39, 103]). More importantly, the labeling procedure for the GPI lipid anchor differs significantly from the other lipid labeling techniques (see experimental details), since in this case the modified lipids (fused with an ACP (acyl carrier protein) tag) are synthesized

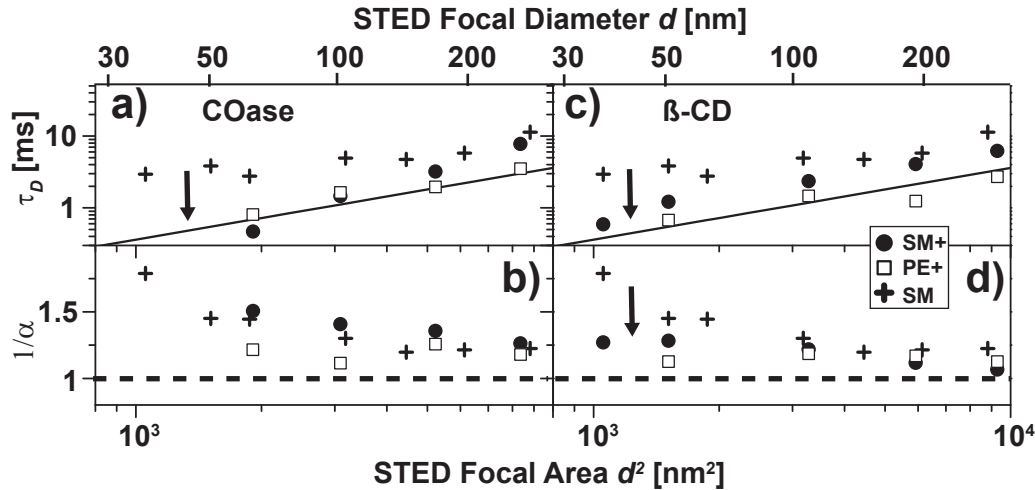


**Figure 4.6: FCS analysis of cholesterol depletion.** Transit time  $\tau_D$  **a, c**) and anomaly ( $1/\alpha$ ) **b, d**) of diffusion determined for  $d < 100$  nm from the correlation data of Atto 647N-labeled PE with cholesterol depletion (open squares) and Atto 647N-labeled SM with (black dots) and without (cross) cholesterol depletion. Cholesterol was depleted from the plasma membrane by the addition of COase (**a, b**) or  $\beta$ -CD (**c, d**). COase and  $\beta$ -CD treatment highlight that trapping of sphingolipids (SM) is cholesterol assisted, revealed by the decrease in  $\tau_D$  (arrow); following COase and  $\beta$ -CD treatment (PE and SM) diffuse nearly as fast as the phospholipid PE in untreated cells ( $D = 5 \times 10^{-9} \text{ cm}^2/\text{s}$ , solid line). Cholesterol depletion by the addition of COase or  $\beta$ -CD may potentially also induce changes in the phase behavior of the membrane, e.g., creating solid like regions in the plasma membrane. Besides possible incomplete cholesterol depletion, such additional COase or  $\beta$ -CD interactions are reflected in our data by the anomaly factor  $1/\alpha > 1$ . Especially in the case of COase treatment, the values of ( $1/\alpha$ ) of SM diffusion remain virtually unchanged. To minimize such additional interactions, the time of  $\beta$ -CD incubation has been chosen much shorter as compared to previous studies[41]. The results are the same, independently of whether COase or  $\beta$ -CD treatment has been performed before or after insertion of the fluorescent lipid analogs into the plasma membrane. This ensures that the changes in sphingolipid dynamics truly result from cholesterol depletion and not from potential differences in the lipid insertion following changes in the plasma membrane induced by COase or  $\beta$ -CD.

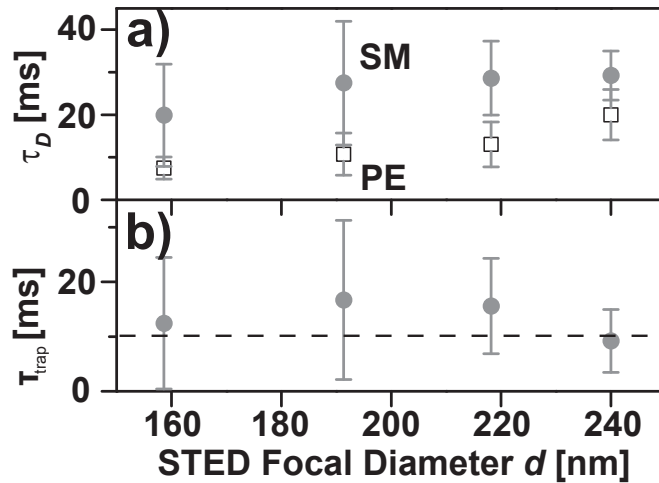


**Figure 4.7: FCS analysis of Atto 647N-labeled PE and SM at or close to the diffraction limit.** **a)** Transit time  $\tau_D$  of diffusion determined from the correlation data of PE (open squares) and SM (grey dots) for  $d > 160$  nm. All correlation data can be described by a single traversing species. The transit times  $\tau_D$  determined for SM are a factor of 1.5–2.5 larger than for PE, but one cannot determine whether SM diffusion is hindered on small spatial scales or normal but just slower than PE diffusion. On the other hand, the single-species data of SM rules out movements of larger and/or slower particles other than the single SM lipid. **b)** Total time of SM trapping  $\tau_D(\text{SM}) - \tau_D(\text{PE})$ , which is a factor of 1.5 larger than the time of a single trapping event  $\tau_{D,\text{trap}} \approx 10$  ms (dashed line, i.e., there is a non-negligible probability of being trapped twice or more often within an area of diameter  $d \approx 200$  nm). One can approximate the total trapping time from the results of the STED analysis, i.e., that SM is trapped on small spatial scales and freely diffusing (just as PE) in between trapping events (figure 4.5). The total trapping time decreases for  $d < 160$  nm, since the probability of detecting (multiple) trapping events declines with the focal spot area. Further, the trapping time is also smaller for  $d > 220$  nm. In the comparatively large focal areas of the diffraction-limited confocal detection the increased transit time leads to an increased probability of photobleaching before leaving the focal spot, introducing bias to the observation of slowly diffusing molecules. Error bars result from averaging over more than thirty measurements

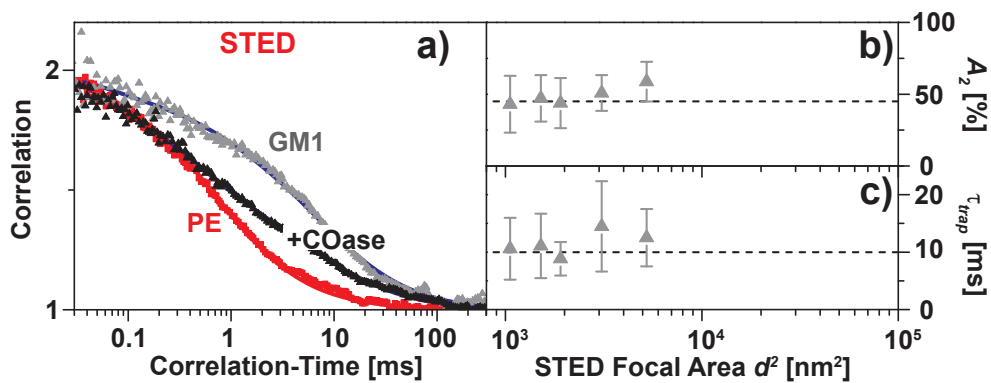


**Figure 4.8: FCS analysis of the Atto 647N-labeled ganglioside GM1 plasma membrane diffusion.** **a)** Normalized STED correlation data ( $d \approx 40$  nm) of GM1 (grey dots) and GM1 with addition of COase (black dots), and for comparison of Atto 647N-labeled PE (red dots). The red line shows a one-species fit to the PE data ( $\tau_D = 0.5$  ms) and the blue lines fits assuming two distinct modalities of focal transits to the GM1 data ( $\tau_{D1} = 0.5$  ms,  $\tau_{D2} = 8.5$  ms and  $A_2 = 60\%$  for GM1 and  $\tau_{D1} = 0.5$  ms,  $\tau_{D2} = 9$  ms and  $A_2 = 30\%$  for GM1 + COase). STED data reveals hindered diffusion of GM1. The addition of COase depletes cholesterol and shifts the correlation data of GM1 to shorter time scales, partially abolishing trapping. **b-c)** Results from FCS analysis of GM1 diffusion for  $d < 70$  nm applying the model of two distinct modalities of focal transits: fraction  $A_2$  ( $\approx 45\%$ ) of hindered-diffusing events **b)** and trapping time  $\tau_{trap}$  ( $\approx 11$  ms) **c)**. Diffusion of GM1 is similar to (Atto 647N-labeled) SM (compare Fig. 3b) and c)), albeit trapping is a little bit less pronounced ( $A_2 \approx 45\%$  compared to  $A_2 \approx 60\%$  for SM) and slightly less abolished upon COase treatment (compare also Supplementary Fig. 6). Error bars result from averaging over more than thirty measurements.



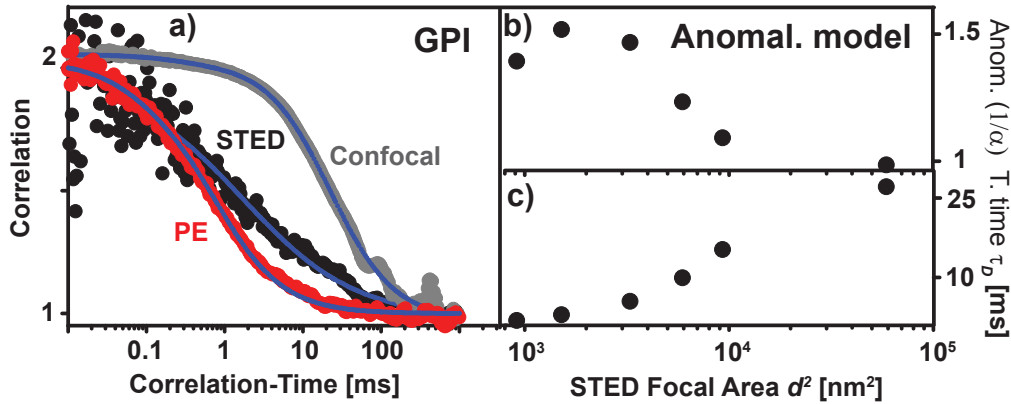


**Figure 4.9: FCS analysis of the Atto 647N-labeled GPI anchor plasma membrane diffusion.**  
**a)** Normalized correlation data of GPI in the confocal (grey circles) and STED mode ( $d \approx 40$  nm, black circles) as well as PE in the STED mode (red circles,  $d \approx 40$  nm) for comparison. The blue line shows a normal one-species fit to the PE data ( $\tau_D = 0.5$  ms) and the confocal GPI data ( $\tau_D = 25$  ms). The GPI STED data was fitted by an anomalous diffusion model ( $1/\alpha = 1.6$  and  $\tau_D = 2.1$  ms). STED data reveals hindered diffusion of the GPI anchor. **b,c)** Results from FCS analysis of the GPI anchor diffusion for  $d < 100$  nm and  $d = 240$  nm (confocal mode) applying the model of anomalous diffusion: apparent diffusion time  $\tau_D$  and anomalous factor  $1/\alpha$ . Diffusion of GPI is similar to (Atto 647N-labeled) SM (compare figure 4.4 and figure 4.5d,e)), albeit with a slightly longer diffusion time in the confocal mode ( $\tau_D^{GPI} = 25$  ms versus  $\tau_D^{SM} = 20$  ms).

by the cell itself and incorporated into the cell membrane and not inserted artificially into the cell membrane. This excludes the unlikely possibility that the heterogeneities observed in the sphingolipid diffusion are artificially introduced by the lipid insertion technique.

All in all, the two sphingolipids SM and GM1 as well as the lipid protein anchor GPI show local trapping, but not the phospholipid PE.

#### *Lipid diffusion: Estimating the spatial extent of trapping*

The findings presented thus far imply that labeled sphingolipids, during their trapping, remain within an area roughly smaller than 30 nm in diameter. This becomes clear if one looks at the dependence of the fraction of trapped molecules  $A_2$  and the trapping time  $\tau_{trap}$  on the focal diameter (see for example figure 4.5), since both values level off roughly between  $30 < d < 60$  nm. If trapped molecules were able to pass those focal diameter, one would expect a decline in the trapping time and in the fraction of trapped molecules. Additionally, the diffusion of the sphingolipids gets increasingly anomalous ( $1/\alpha$

increases) if the focal diameter is of those sizes.

All in all our data show that if 'rafts' exists at all they have to be smaller than 30 nm and they have to be localized at least for a short period of time.

### 4.3.2 Monte Carlo simulations of lipid diffusion

To further analyze the results presented in the last section I have used Monte Carlo simulations (see [68] for a similar approach) to see how different models for the diffusion of sphingolipids reflect our data.

Briefly, fluorescence time traces of the diffusion of lipids within a certain area of the plasma membrane were generated. The diffusing molecules were assumed to be excited by Gaussian shaped spots, with different focal diameters representing different STED powers. In the beginning, a certain number of molecules were randomly distributed over the simulation area. The focal spot was then placed arbitrarily on the simulation area assuring that no particular geometry was preferred. The results from ten time traces were subsequently averaged.

First the diffusion behavior assuming domains of various size with impermeable barriers for the lipids were simulated. Figure 4.10 shows how the anomaly factor  $1/\alpha$  depends on the focal diameter for different domains sizes and compares it to the experimental results for PE and SM. While one can observe a small increase in the  $1/\alpha$  up to values of  $\sim 1.1$ , especially for larger domain sizes in the simulations. This can clearly not explain the much larger increase in the experimental values of  $1/\alpha$  observed for SM, but may reflect the behavior of PE within the standard error of our experiments.

In a second approach, potential interaction areas or nanodomains of different sizes (molecular complexes, 20 nm, 50 nm diameter) were randomly placed all over the simulation area. The nanodomains were assumed to be immobile, circular domains with a hardcore potential precluding their overlap. The diffusion of the lipids was assumed to be free between and within the nanodomains, with a diffusion coefficient of  $5 \cdot 10^{-9} \text{ cm}^2/\text{s}$  between the domains and a three times lower coefficient within them. It was assumed that lipid molecules could enter the domains with a probability  $p_{in} = 10^{-4}$  every time they reach a domain barrier (similar to the approach in [68]). The lipids then continue to diffuse within the nanodomains, only with a smaller diffusion coefficient ( $D_{in} = D_{out}/3$ ), and can leave the domain with a probability  $p_{out} = 4.5 \cdot 10^{-4}$  upon reaching the boundaries again. The exiting and entering probabilities were chosen in such a way as to ensure an average trapping time of  $\sim 10$  ms as observed in our experiments. The results of the analysis of the data generated by the simulation for changing domain sizes from 0 - 50 nm and focal diameters from 10 - 250 nm are displayed in figure 4.11. The figure shows the behavior of both the trapping time  $\tau_{D2}$  and the fraction  $A_2$  in the case of the two species model, and the anomaly factor  $1/\alpha$  and the average transit  $\tau_D$  for the anomalous diffusion model. The dependence of all parameters on the focal diameter is only in a fairly good agreement with my experimental results for small domains with a size of 20 nm or smaller, additionally supporting the conclusion I have made in the last section that if nanodomains exist they have to be smaller than 30

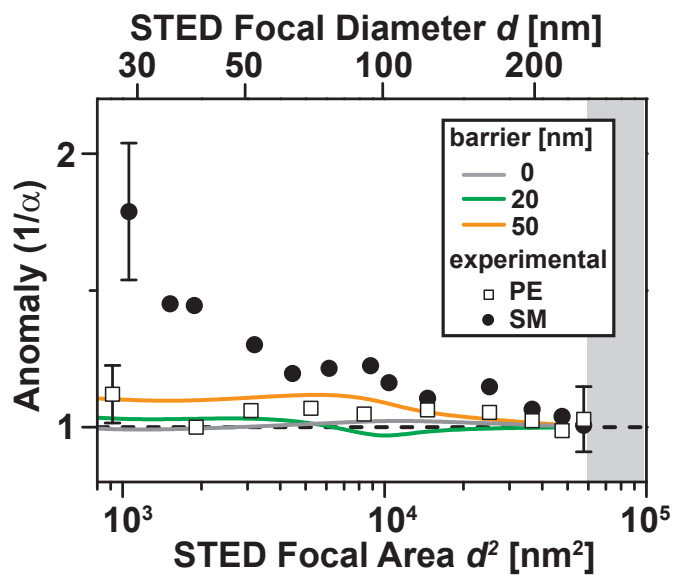


**Figure 4.10: Monte Carlo simulation of lipid diffusion.** Anomaly ( $1/\alpha$ ) determined from fitting the model of anomalous diffusion to FCS data generated by Monte Carlo simulations of free lipid diffusion with impermeable domain barriers of different diameters: free diffusion (‘0 nm’ grey line), 50 nm (orange) and 20 nm (green); and experimental data of Atto 647N-labeled PE (open squares) and SM diffusion (black dots). Further results from Monte Carlo simulations of nanodomain integration or molecular complex formation are given in Fig. 3. See text for details. Typical error bars are exemplary given, resulting from averaging over more than thirty FCS measurements.

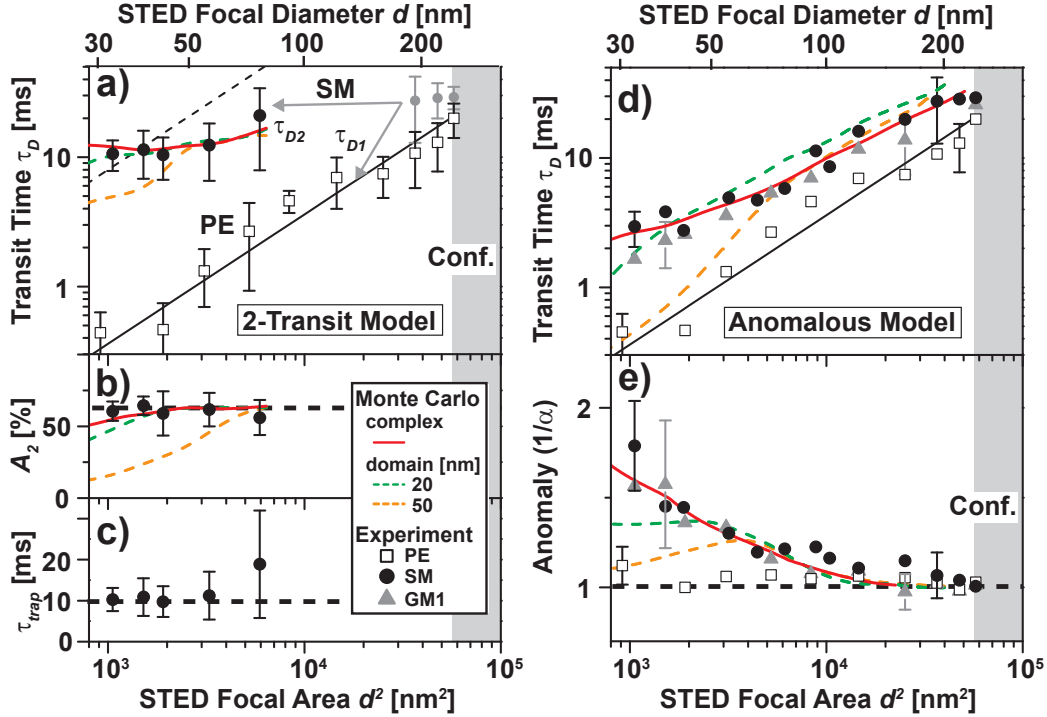


**Figure 4.11: Results from Monte Carlo - simulations of sphingolipid diffusion compared with experimental data.** See caption of figure 4.5 for details of the experimental data. The observed diffusion characteristics of SM and GM1 is compatible with Monte Carlo simulations assuming molecular complex formation (red line) but less compatible with lipid integration into nanodomains of 20 nm (green dashed line) and definitively strongly deviates for nanodomains of 50 nm diameter (orange dashed line). See text for details.

nm. Moreover, differences between the MC - Simulation results and the experimental data for domains with sizes greater than 20 nm only become significant for focal diameters  $< 50$  nm, showing ones more the importance of reaching small focal areas.

Finally, we simulated the time traces with freely diffusing lipids forming transient complexes characterized by an equilibrium reaction. The kinetic rates  $k_{on} = k_{off} = 8 \cdot 10^5$  1/s for the trapping were again chosen in such a way as to ensure the experimentally estimated trapping time of  $\sim 10$  ms. As can be seen in figure 4.11 the experimental data can be well described by the simulation results, with regards to the tendencies of the different parameters for both diffusion models (transit time  $\tau_D$ , fraction of trapped molecules  $A_2$ , anomaly factor  $1/\alpha$  and trapping time  $\tau_{trap}$ ).

Altogether both models, the nanodomains ( $< 20$  nm) and the transient complexes model, lead to results which can explain our experiments, with the results of the transient complexes model giving

the best fit of the experimental data.

### 4.3.3 Membrane affinity of the labeled lipids

A fluorescent label may alter the properties of its targeted species. They may significantly change the spatial size and the weight of the labeled molecule, the polarity, they may block binding sites (steric hindrance) or prevent intramolecular interactions. Moreover, the dye labels can introduce additional interactions not present for the non-labeled molecules. Here I will therefore discuss possible effects of the fluorescently labeled lipids on the membrane structure and behavior of lipids, and problems that could occur as previously outlined on model membranes[114].

Since lipids are comparably small molecules themselves, the general labeling strategy is to substitute a part of the lipid structure with the dye as to not alter either the molecular weight or the general shape of the lipids significantly [114](M.W.(lipids)  $\sim$ 800 - 1000, M.W.(dyes)  $\sim$ 650). Normally this means that one of the two acyl-chains (see figure 4.12d)) is replaced by the dye. In order to be a good replacement for an acyl chain the dye has to fulfill two main requirements. First, since the acyl chains are located in the hydrophobic lipid phase and normally do not flip to the water interface, the dye has to be sufficiently hydrophobic and second, the dye should ideally have comparable steric properties to the acyl chain. The first requirement is well met by the dye, Atto 647N, which I have used in most of the experiments, as shown by silica gel chromatography (data not shown). The second requirement is harder to fulfill because most organic dyes are rather bulky molecules, especially if one needs a photostable and bright dye, as in single molecule experiments. On the other hand, acyl chains, which are linear molecules, can be relatively bulky themselves especially in their various unsaturated forms. Nevertheless, studies which show that dyes indeed influence the behavior of lipids to which they are attached to (BODIPY or NBD, two widely used dyes, alter significantly the affinity of sphingolipids for liquid ordered domains), have found that dyes do so mostly because of their strong hydrophilic nature and less due to their steric properties[114]. Nevertheless, I have performed several control measurements to ensure that the different behavior of the labeled phospholipids and sphingolipids is not due to artifacts introduced by the dye<sup>3</sup>.

I have incorporated dye labeled phospho-, sphingo- and ganglioside lipids (PE, SM and GM1) into the membrane with altered dye positions: at the water phase, e.g. attached to the polar headgroup (PE, CPE, GM1<sup>+</sup>), or the water - lipid interface, e.g. replacing the acyl chain (see PE1, SM, GM1 in figure 4.12d)). The difference in the diffusion behavior of phospholipids and sphingolipids remains unaltered irrespective of the dye position. The trapping is only significant for the sphingolipids SM, CPE, GM1 and GM1<sup>+</sup> ( $1/\alpha > 1.5$ ) whereas the phospholipids PE and PE1 ( $1/\alpha < 1.2$ ) diffuse freely (see figure 4.12c)). In each case, treatment of the cells with cholesterol oxidase reduced the amount of trapping for the sphingolipids (figure 4.12b)). The reduction is more pronounced for SM and CPE than for the gangliosides. The difference in the molecular dynamics between lipids which only differ

---

<sup>3</sup>The structure of the dyes Atto 647N and Atto532 is kept secret by the company AttoTec.

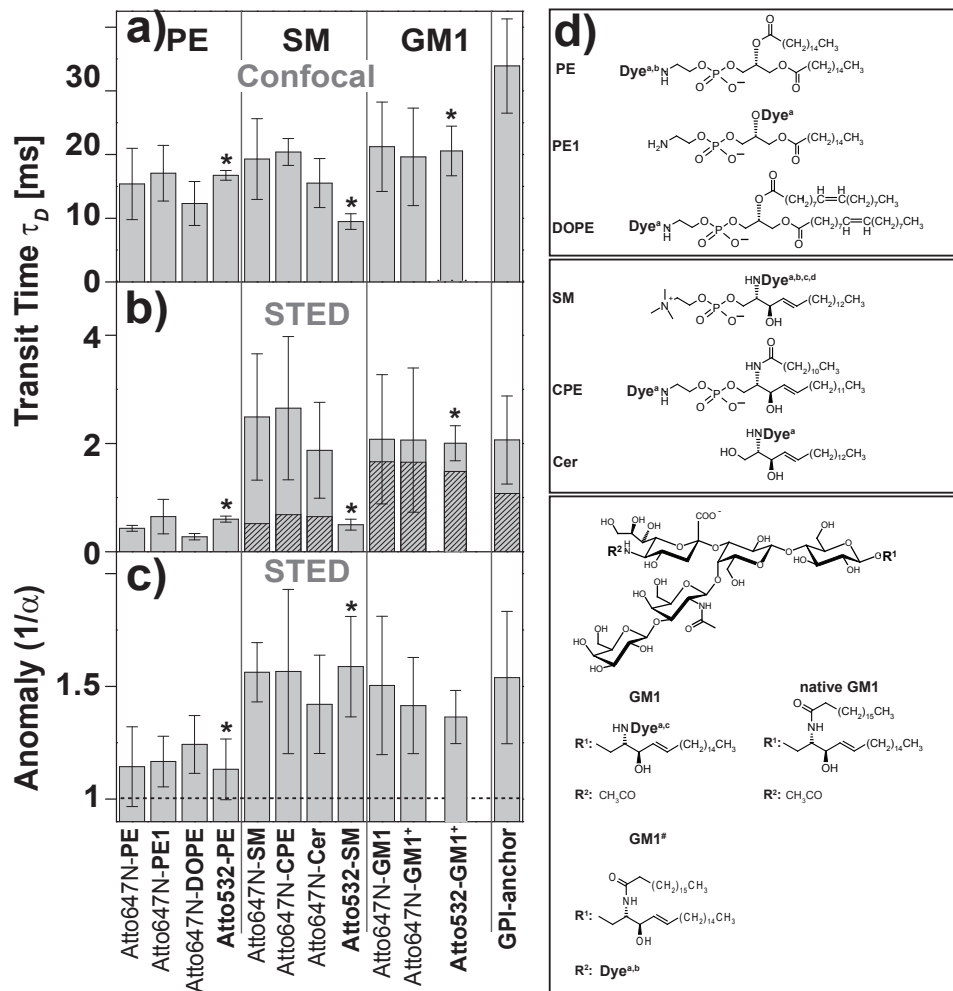


**Figure 4.12: Membrane affinity of the Atto 647N-labeled lipids: Analysis of the plasma membrane diffusion of different fluorescent lipid analogs and their structures.** a-c) FCS analysis applying the model of anomalous diffusion for confocal ( $d \approx 240$  nm) a) and STED ( $d \approx 40$  nm) recording b,c): average transit time  $\tau_D$  a,b) and anomaly ( $1/\alpha$ ) c) of the Atto 647N-labeled phospho- PE, PE1 and DOPE, sphingo- SM, CPE and Cer, and ganglioside lipids GM1 and GM1<sup>+</sup>, of Atto532-labeled PE, SM and GM1<sup>+</sup>, and of an Atto 647N-tagged GPI-anchor. The mashed bars in b) indicate the values of  $\tau_D$  determined for the sphingo- and ganglioside lipids after cholesterol depletion by COase treatment. The Atto532-labeled derivatives were measured in slightly different focal spots ( $d \approx 200$  nm and 60-70 nm for confocal and STED, respectively, due to the different laser wavelengths and STED intensities applied) and the values of  $\tau_D$  were approximately extrapolated to values expected for  $d \approx 240$  nm and 40 nm. Error bars result from averaging over more than thirty measurements. **d)** Structural details of the different lipid analogs in our experiments. See text for further details.

in their backbone structure but not in the position of the dye label (compare PE with CPE and PE1 with SM) rule out any significant influence of the dye on the diffusion behavior. Additionally, the unsaturated lipid dioleoyl-glycero-phosphoethanolamine DOPE behaves as the saturated counterpart PE.

Moreover, since the sphingolipids CPE and SM, only differing in the acyl chain structure, show the same heterogeneities in their diffusion one can conclude that the structure of the lipid backbone is essential for the trapping of the sphingolipids, most probably due to the ability of the ceramide backbone to function simultaneously as a hydrogen donor and acceptor (compare section 4.1.1). This is supported by the anomalous diffusion ( $1/\alpha > 1.4$ ) of the Atto 647N labeled ceramide (Atto 647N - Cer) shown in figure 4.12c), see d) for the structure of ceramide).

When I substitute the lipophilic dye Atto 647N with the more hydrophilic dye Atto532 the general behavior of the labeled lipids is changed. In the case of SM the abnormality remains high with ( $1/\alpha > 1.5$ ) for the STED mode, but the diffusion time is significantly shorter in the STED as well as in the confocal mode. Thus indicating a slightly less perfect incorporation of the dye labeled lipid into the membrane as one would expect due to the hydrophilic nature of the dye Atto532 (chromatographic data not shown). For GM1 and PE no difference is observable for the lipids labeled with both dyes, most probably since in both cases the lipids are labeled at the polar headgroups, shielding away possible influence from the polarity of the dye.

To test whether the pure dye Atto 647N interacts with molecules within the membrane, I tried to incorporate the dye into the membrane. This proved itself to be difficult. Furthermore, there is no trapping present (data not shown), so that interaction of the dye with parts of the membrane alone can also be dismissed.

A further proof of the biological relevance of my findings is the observed cholesterol assisted trapping (see figure 4.9 and figure 4.12a-c)) of a glycosol-phosphatidyl-inositol (GPI) anchor similar to the trapping seen for the sphingolipids. It was already shown that GPI anchored proteins are trapped, with the lipid anchor mediating the trapping[15, 39, 54, 105]. The labeling here was done by an acyl carrier protein (ACP) attached to the dye Atto 647N. Since this is a completely different labeling procedure than the one used for the lipids it is rather unlikely that this would lead to comparable results only induced by artifacts (compare section 4.3.1).

#### **4.3.4 Photobleaching and adverse STED effects on the plasma membrane**

Due to the high power applied in the STED mode, one has to be careful not to introduce experimental bias into the observed system. Possible artifacts can stem from photobleaching[30], local heating by absorption[95] or the creation of various highly reactive molecules like radicals[5]. Photobleaching can occur from the triplet state as well as the first and higher excited states of the dye molecules[23, 31]. Local heating may result from absorption in the surrounding water, by the lipids and proteins, or the fluorophore. Highly reactive molecules emerge from excited reactive species and their generation has

been shown in artificial membranes by excited fluorescence dyes when attached to lipids [5].

The pulse STED intensity of up to  $6 \text{ GW/cm}^2$  (corresponding to a STED power of  $> 100 \text{ mW}$ ) is in the range of the intensities used in multi photon microscopy[18], if one takes into account the 100-1000 times shorter pulse duration in the STED case. Multi photon microscopy is routinely used in live cell experiments. Moreover morphological changes of the cell could not be observed during measurements performed in the STED mode (checked by transmitted light microscopy).

I do not anticipate any heating effect, since the heat dissipation of the surrounding water should be sufficient, especially when one take into consideration the 4 - 5 times bigger envelope and cross section of the doughnut compared to a confocal spot, allowing for a more effective heat dissipation[95].

The generation of radicals, although observable in artificial membranes, should be less of a problem in native membranes since in biological systems many radical scavenger systems are present to prevent damage by radicals [5]. Moreover, especially in the single molecule experiments the dye concentration is very low so that the production of radicals should be very ineffective right from the beginning. If radical formation would play a significant role any change in the dye concentration should alter the results of the measurement. This was not observed even for large changes of the concentration in the range of two orders of magnitude between FCS and single molecule experiments.

Nonetheless I have performed some controls to exclude radical formation as well as local heating by scanning the focal spot slowly over the membrane. The scanning was either done in a hop - like fashion (step length  $1.7 \mu\text{m}$ ,  $0.5 \text{ s}$  dwell time per pixel) or by continuously scanning (step length  $40 \text{ nm}$ ,  $0.5 \text{ s}$  dwell time per pixel) over the cell membrane. In both cases the long dwell time ensures that the scanning itself is slow enough to not influence the recorded correlation data, but to exclude potential adverse effect by heating and radical formation. In all control experiments I could not observe any difference in the diffusion behavior of the lipids.

The last potential source of artifacts is photobleaching by the excitation light or by the STED light. As I have previously mentioned the cross section for stimulated emission is similar to the cross section for photobleaching ( $10^{-17} \text{ cm}^2$ ) so that the de-excitation rates are generally more efficient than the bleaching rates by STED (bleaching probability from excited states  $\sim 10^{-8} - 10^{-6}$ ), even from higher excited states. This however does not completely exclude possible bleaching of molecules by the STED light in the focal periphery. To check whether this has an effect on the molecular dynamics I have analyzed the correlation data with FCS (anomalous model, see equation (2.2.12)) and with FIDA (see section 2.3). Figure 4.13a) shows that for the freely diffusing PE the number of particles decrease in agreement with the reduction in the focal volume given by the decrease in the lateral diffusion time  $\tau_D$  (compare equation 2.2.9). This is also the case for the particle number of SM despite the fact that the diffusion time is dominated by trapping and therefore does not scale proportionally. Bleaching should be visible in the data by an additional decrease in the number of particles,  $N$ , because any molecule which is bleached by STED before entering the detection area, is not counted. Therefore one can conclude that bleaching by STED does not play a prominent role. Moreover the observed correspondence between  $N$  and  $\tau_D$  is also a strong indicator that other artifacts by STED are not



significantly influencing my results, since any of them should either artificially increase or decrease the number of particles and therefore break the observed proportionality.

More interesting is the bleaching by the excitation light. In the previous chapter I have already shown that STED is able to reduce the amount of bleaching by reducing the effective observation time of the molecules (compare figure 3.6). In figure 4.13b) the relative transit (observation) time  $\tau_D$  is plotted against the excitation power  $P_{exc}$  for STED ( $d \approx 40$  nm) and confocal confinement. As expected the decline in the relative transit time is more prominent for PE in the confocal mode compared to the STED mode, indicating that bleaching by the excitation light is of greater importance for the confocal detection due to the per se longer transit times. For SM the picture is somewhat different. Here, the relative transit time is strongly affected in both detection modi (figure 4.13b)) and the absolute transit times (figure 4.13c)) of SM and PE in the STED mode are approaching each other. At the same time, the anomaly (figure 4.13d)) of both lipids for the STED mode are also becoming ever more similar, approaching the anomaly of the confocal detection mode. That means, that for high excitation powers SM exhibits the same diffusion behavior as PE, because eventually trapped SM molecules are predominantly bleached. In other words the maximal observation time of a molecule, defined by the bleaching probability and not by the diffusion time has to be significantly longer than the trapping time or one is not able to observe trapping events in an unbiased manner.

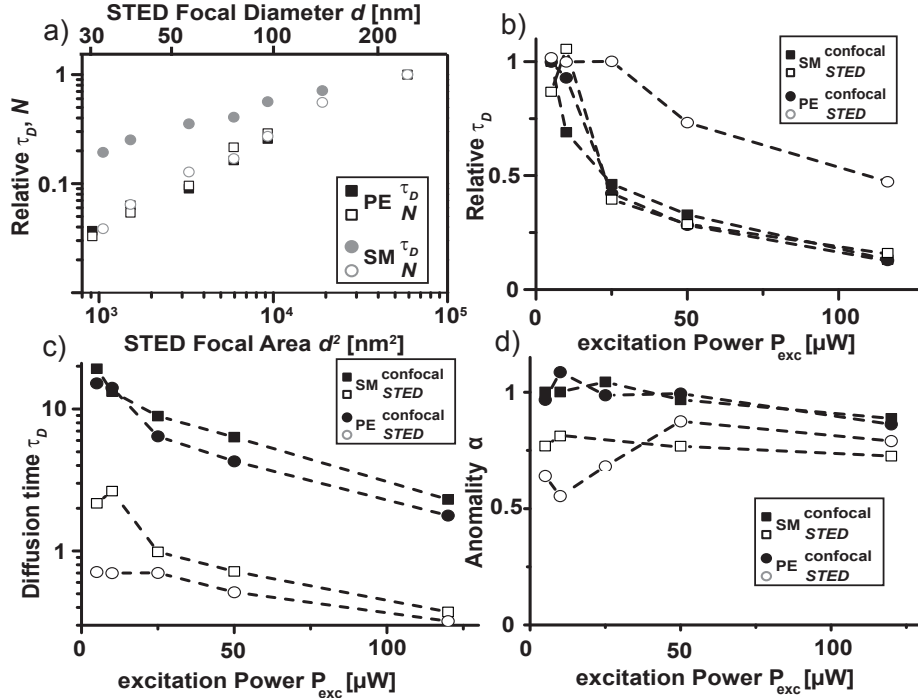


**Figure 4.13: Evidence against artifacts when generating subdiffraction focal spots by STED:**  
a) Relative reduction of the particle number  $N$  and average transit time  $\tau_D$  of Atto 647N-labeled PE and SM diffusion with focal diameter  $d$  confined by STED. I determined the values of  $N$  and  $\tau_D$  from FIDA and FCS (applying the model of anomalous diffusion), respectively. All values are normalized to the value determined with a confocal spot of low excitation power ( $P_{exc} = 5 \mu\text{W}$ ). As expected from a 'ideal' reduction of the fluorescence spot by STED,  $N$  and  $\tau_D$  decline in proportion to the focal area. While the transit time of SM deviates from this linear dependence due to the local trapping reported in section 4.3.1, the SM particle number  $N$  still scales with the focal area, as expected from a flawless reduction of the fluorescence spot by STED. This independence of the average particle number from the local transit time is a strong argument against light-induced artifacts induced by the spot size reduction due to STED, such as photobleaching. **b,c,d)** Diffusion time  $\tau_D$  b), relative diffusion time  $\tau_D$  normalized to the confocal value for low excitation power ( $P_{exc} = 5 \mu\text{W}$ ) c) and anomaly  $1/\alpha$  d) plotted against the excitation power  $P_{exc}$  for confocal confinement and STED confinement ( $d \approx 40 \text{ nm}$ ). All three values were estimated using the Anomalous Diffusion model for FCS. The applied STED power was  $\sim 200 \text{ mW}$ , giving a focal diameter of  $\sim 40 \text{ nm}$ . The relative diffusion time strongly declines in the confocal case for both lipids SM (black squares) and PE (empty squares) as expected due to photobleaching by the increasing excitation power. In the STED mode the decline for PE (empty circles) is less pronounced because of the shorter observation time. This is different for SM (empty squares) because here trapped molecules with a trapping time of  $\sim 10 \text{ ms}$  are also predominantly bleached, leading to a strong decline in the diffusion time of SM (empty squares) approaching the free diffusion time of PE (empty circles) (b).

## 5 Conclusion

Fluorescence single molecule spectroscopy is a well established technique to study a huge variety of biological process and dissect the dynamics behind those processes[28, 73, 100, 116]. Although the various fluorescence spectroscopy methods are able to span large time scales, ranging from picoseconds[26] to minutes[10], they are fundamentally limited in their spatial resolution by diffraction.

I have shown in my work how recent improvements in the resolution of fluorescence microscopy by the RESOLFT or STED concept, already successfully applied for imaging various cell components[22, 124], can be extended to two prominent fluorescence spectroscopy methods: single molecule analysis (SMA) and Fluorescence Correlation Spectroscopy (FCS). In the first part of my study I scrutinized in detail the reasons for the problems encountered in an earlier attempt to perform fluctuation fluorescence spectroscopy at the nanoscale in a 3D volume[59]. The low signal to noise ratio, which was negatively impacting the further prospect of STED FCS and STED SMA in this earlier study, stems from low brightness noise due to incomplete fluorescence inhibition in the axial out of focus areas. An important insight of the first part of my study is that a reduction of the sample dimension from three- to two-dimensional (for example lipid membranes) completely removes the problem associated with the uncorrelated low brightness background, thereby enabling one to perform single molecule spectroscopy with a signal to noise ratio equal to a standard confocal approach, but with a nanoscale resolution. This is not to say that three dimensional STED single molecule spectroscopy is impossible but rather less convenient and still needs further improvement.

In the second part of my work I have successfully applied STED FCS and STED SMA to a prominent and widely studied biological problem: What is the structural and dynamical nature of lipid - protein nanodomains in the plasma membrane of living eukaryotic cells? This was thus far not addressable by diffraction limited fluorescence microscopy[54]. I was able to show that the sphingolipid sphingomyelin SM and the ganglioside GM1 as well as the GPI lipid anchor undergo cholesterol interaction on spatial scales below 30 nm in the plasma membrane of living cells, eventually forming lipid nanodomains, while the phospholipid PE does not show such kind of interactions. This was made possible by using the ability of the STED microscope to seamlessly tune the focal diameter from  $\sim 250$  nm down to  $\sim 30$  nm by simply varying the applied STED power.

The study of single molecule dynamics on the nanoscale on biological cell membranes of living cells opens a whole new field of possible applications and is not restricted to the dynamics of lipids. The vast amount of available labeling techniques should allow to investigate the dynamics of various membrane components in area smaller than the diffraction limit. A first example is the dynamics of the GPI anchor labeled with an ACP tag - attached fluorescent dye (see figure 4.12).

Another important result of my study is the counter intuitive fact that the STED microscope, at least for dynamic studies, is less prone to bias introduced by photobleaching than a confocal microscope. Photobleaching is a widely studied issue in the field of single molecule spectroscopy and thus far a major source of artifacts in a lot of its applications, especially for the slow diffusion regime. The problem

of photobleaching is usually attacked by three different approaches: (1) photobleaching is directly incorporated into the model, (2) photobleaching is minimized by low excitation intensities, stable dyes (e.g. Quantum dots) or chemical stabilizers[118], or (3) photobleaching is avoided by technically sophisticated measurement methods (e.g. scanning FCS [84]). STED FFS belongs to the third type and provides a new approach by reducing the effective observation time and thus the photobleaching probability of the dye molecules.

Finally, I want to stress, that the STED method is not only restricted to the fluorescence fluctuation spectroscopy methods I have used in my work, but is in principle extendable to any fluorescence spectroscopy technique available, since STED does not influence the dyes within the very focal center by design. Examples would be: fluorescence resonance energy transfer (FRET)[66], fluorescence lifetime imaging (FLIM)[4] and fluorescence lifetime correlation spectroscopy (FLCS)[9] among others.

## List of Publications

Parts of this thesis have been published as follows:

1. C. Ringemann, A. Schönle, A. Giske, C. v. Middendorf, S. W. Hell and C. Eggeling. Enhancing fluorescence brightness: Effect of reverse intersystem crossing studied by fluorescence fluctuation spectroscopy. *ChemPhysChem* 9:612-624, 2008
2. C. Eggeling, M. Hilbert, H. Bock, C. Ringemann, M. Hofmann, A.C. Stiel, M. Andresen, S. Jakobs, A. Egner, A. Schönle and S. W. Hell. Reversible photoswitching enables single-molecule fluorescence fluctuation spectroscopy at high molecular concentration. *Microscopy Research and Technique* 70:1003-1009, 2007
3. C. Eggeling\*, C. Ringemann\*, R. Medda, G. Schwarzmann, K. Sandhoff, S. Polyakova, V. N. Belov, B. Hein, C. v. Middendorff, A. Schönle and S. W. Hell. Direct observation of the nanoscale dynamics of membrane lipids in a living cell. submitted to *Nature*

\*These authors contributed equally to this work.

## References

- [1] E. Abbe. Beiträge zur theorie des mikroskops und der mikroskopischen wahrnehmung. *Arch. Mikr. Anat.*, 9:413–468, 1873.
- [2] B. Albrecht, G. Pohlentz, K. Sandhoff, and G. Schwarzmann. Synthesis and mass spectrometric characterization of digoxigenin and biotin labeled ganglioside gm1 and their uptake by and metabolism in cultured cells. *Chem. Phys. Lipids*, 86:37–50, 1997.
- [3] R.G. Anderson and K.A. Jacobson. A role for lipid shells in targeting proteins to caveolae, rafts, and other lipid domains. *Science*, 296:1821–1825, 2002.
- [4] E. Auksorius, B. R. Boruah, C. Dunsby, P. M. P. Lanigan, G. Kennedy, M. A. A. Neil, and P. M. W. French. Stimulated emission depletion microscopy with a supercontinuum source and fluorescence lifetime imaging. *Opt. Lett.*, 33(2):113–115, 2008.
- [5] A.G. Ayuyan and F.S. Cohen. Lipid peroxides promote large rafts: Effects of excitation of probes in fluorescence microscopy and electrochemical reactions during vesicle formation. *Biophys. J.*, 91:2172–2183, 2006.
- [6] K. Bacia, D. Scherfeld, N. Kahya, and P. Schwille. Fluorescence correlation spectroscopy relates rafts in model and native membranes. *Biophys. J.*, 87:1034–1043, 2004.
- [7] K. Balasubramanian and A.J. Schroit. Aminophospholipid asymmetry: a matter of life and death. *Annu. Rev. Physiol.*, 65:701–734, 2003.
- [8] W. Baumeister. Electron tomography: towards visualizing the molecular organization of the cytoplasm. *Curr. Opin. Struct. Biol.*, 12:679–684, 2002.
- [9] M. Böhmer, M. Wahl, H. Rahn, R. Erdmann, and J. Enderlein. Time-resolved fluorescence correlation spectroscopy. *Chem. Phys. Lett.*, 353:439–445, 2002.
- [10] D.A. Stavreva B.L. Sprague, R.L. Pego and J.G. McNally. Analysis of binding reactions by fluorescence recovery after photobleaching. *Biophys J*, 86:3473–3495, 2004.
- [11] M. Born and E. Wolf. *Principles of Optics*. Cambridge University Press, Cambridge, New York, Melbourne, Madrid, Cape Town, 7th edition, 2002.
- [12] M. Bossi, J. Fölling, M. Dyba, V. Westphal, and S. W. Hell. Breaking the diffraction resolution barrier in far-field microscopy by molecular optical bistability. *New J. Phys.*, 8:275, 2006.
- [13] M.S. Bretscher. Membrane structure: some general principles. *Science*, 181:622–629, 1973.
- [14] S. Bretschneider, C. Eggeling, and S. W. Hell. Breaking the diffraction barrier in fluorescence microscopy by optical shelving. *Phys. Rev. Lett.*, 98:218103, 2007.

- [15] D.A. Brown and E. London. Structure and function of sphingolipid- and cholesterol-rich membrane rafts. *J. Biol. Chem.*, 275(23):17221–17224, 2000.
- [16] Y. Chen, J.D. Müller, P.T.C. So, and E. Gratton. The photon counting histogram in fluorescence fluctuation spectroscopy. *Biophys. J.*, 77:553–567, 1999.
- [17] R. F. de Almeida, L. Loura, A. Fedorov, and M. Prieto. Lipid rafts have different sizes depending on membrane composition: A time-resolved fluorescence resonance energy transfer study. *J. Mol. Biol.*, 346:1109–1120, 2005.
- [18] W. Denk, J. H. Strickler, and W. W. Webb. Two-photon laser scanning fluorescence microscopy. *Science*, 248:73–76, 1990.
- [19] C. Dietrich, L. A. Bagatolli, N. L. Volovyk, N. L. Thompson, M. Levi, K. Jacobson, and E. Gratton. Lipid rafts reconstituted in model membranes. *Biophys. J.*, 80:1417–1428, 2001.
- [20] J. A. Dix and A. S. Verkman. Crowding effects on diffusion in solutions and cells. *Annu. Rev. Biophys.*, 37:247–63, 2008.
- [21] G. Donnert, C. Eggeling, and S. W. Hell. Major signal increase in fluorescence microscopy through dark-state relaxation. *Nat. Methods*, 4(1):81–86, 2007.
- [22] G. Donnert, J. Keller, R. Medda, M. A. Andrei, S. O. Rizzoli, R. Lührmann, R. Jahn, C. Eggeling, and S. W. Hell. Macromolecular-scale resolution in biological fluorescence microscopy. *Proc. Natl. Acad. Sci. USA*, 103(31):11440–11445, 2006.
- [23] M. Dyba and S.W. Hell. Photostability of a fluorescent marker under pulsed excited-state depletion through stimulated emission. *Appl. Optics*, 42(25):5123–5129, 2003.
- [24] M. Edidin. The state of lipid rafts: from model membranes to cells. *Annu. Rev. Biophys. Biomol. Struct.*, 32:257–283, 2003.
- [25] C. Eggeling. *Analyse von photochemischer Kinetik und Moleküldynamik durch mehrdimensionale Einzelmolekül-Fluoreszenzspektroskopie*. PhD thesis, Georg-August-Universität, 1999.
- [26] C. Eggeling, S. Berger, L. Brand, J.R. Fries, J. Schaffer, A. Volkmer, and C. A. M. Seidel. Data registration and selective single-molecule analysis using multi-parameter fluorescence detection. *J. Biotechnol.*, 86:163–180, 2001.
- [27] C. Eggeling, M. Hilbert, H. Bock, C. Ringemann, M. Hofmann, A. C. Stiel, M. Andresen, S. Jakobs, A. Egner, A. Schönle, and S. W. Hell. Reversible photoswitching enables single-molecule fluorescence fluctuation spectroscopy at high molecular concentration. *Micr. Res. Tech.*, 70:1003–1009, 2007.

- [28] C. Eggeling, S. Jäger, D. Winkler, and P. Kask. Comparison of different fluorescence fluctuation methods for their use in fret assays: Monitoring a protease reaction. *Curr. Pharm. Biotechnol.*, 6(351-371), 2005.
- [29] C. Eggeling, A. Volkmer, and C. A. M. Seidel. Molecular photobleaching kinetics of rhodamine 6g by one- and two-photon induced confocal fluorescence microscopy. *ChemPhysChem*, 6:791–804, 2005.
- [30] C. Eggeling, J. Widengren, R. Rigler, and C. A. M. Seidel. Photobleaching of fluorescent dyes under conditions used for single-molecule detection: Evidence of two-step photolysis. *Anal. Chem.*, 70:2651–2659, 1998.
- [31] C. Eggeling, J. Widengren, R. Rigler, and C. A. M. Seidel. Photostabilities of fluorescent dyes for single-molecule spectroscopy: Mechanisms and experimental methods for estimating photobleaching in aqueous solution. In W. Rettig, B. Strehmel, M. Schrader, and H. Seifert, editors, *Applied fluorescence in chemistry, biology and medicine*, pages 193–240. Springer, Berlin, 1999.
- [32] M. Ehrenberg and R. Rigler. Rotational brownian motion and fluorescence intensity fluctuations. *Chem. Phys.*, 4:390–401, 1974.
- [33] E.L. Elson and D. Magde. Fluorescence correlation spectroscopy i. conceptual basis an theory. *Biopolymers*, 13:1–27, 1974.
- [34] J. Enderlein, I. Gregor, D. Patra, T. Dertinger, and U. P. Kaupp. Performance of fluorescence correlation spectroscopy for measuring diffusion and concentration. *ChemPhysChem*, 6(11):2324–2336, 2005.
- [35] J. Enderlein, D.L. Robbins, W.P. Ambrose, P.M. Goodwin, and R.A. Keller. The statistics of single molecule detection: An overview. *BioImaging*, 5(3):88–98, 2001.
- [36] J. Enderlein, D.L. Robbins, W.P. Ambrose, and R.A. Keller. Molecular shot noise, burst size distribution, and single-molecule detection in fluid flow: Effects of multiple occupancy. *J. Phys. Chem. A*, 102:6089–6094, 1998.
- [37] T. J. Feder, I. Brust-Mascher, J. P. Slattery, B. A. Baird, and W. W. Webb. Constrained diffusion or immobile fraction on cell surfaces: A new interpretation. *Biophys. J.*, 70:2767–2773, 1996.
- [38] E. Fernandez-Sequra and A. Warley. Electron probe x-ray microanalysis for the study of cell physiology. *Methods in Cell biology.*, 88:19–43, 2008.
- [39] C.J. Fielding. *Lipid Rafts and Caveolae*. Wiley-VCH, Weinheim, 2006.



- [40] J.R. Fries, L. Brand, C. Eggeling, M. Köllner, and C. A. M. Seidel. Quantitative identification of different single-molecules by selective time-resolved confocal fluorescence spectroscopy. *J. Phys. Chem. A*, 102:6601–6613, 1998.
- [41] M. Hao, S. Mukherjee, and F.R. Maxfield. Cholesterol depletion induces large scale domain segregation in living cell membranes. *Proc. Natl. Acad. Sci. USA*, 98(23):13072–13077, 2001.
- [42] B. Harke, J. Keller, C. K. Ullal, V. Westphal, A. Schoenle, and S. W. Hell. Resolution scaling in sted microscopy. *Optics Express*, 16(6):4154–4162, 2008.
- [43] B. Harke, J. Ullal, J. Keller, and S. W. Hell. Three-dimensional nanoscopy of colloidal crystals. *Nano Lett.*, 8 (5):1309–1313, 2008.
- [44] E. Haustein and P. Schwille. Ultrasensitive investigations of biological systems by fluorescence correlation spectroscopy. *Methods*, 29(2):153–166, 2003.
- [45] H. Heerklötz. Triton promotes domain form in lipid raft mixtures. *Biophys J*, 83:2693–2701, 2002.
- [46] S. W. Hell and J. Wichmann. Breaking the diffraction resolution limit by stimulated emission: stimulated emission depletion microscopy. *Opt. Lett.*, 19(11):780–782, 1994.
- [47] S.W. Hell. Toward fluorescence nanoscopy. *Nature Biotechnol.*, 21(11):1347–1355, 2003.
- [48] S.W. Hell. Far-field optical nanoscopy. *Science*, 316(5828):1153–1158, 2007.
- [49] S.W. Hell, G. Reiner, C. Cremer, and E. H. K. Stelzer. Aberrations in confocal fluorescence microscopy induced by mismatches in refractive index. *J. Microsc.*, 169:391–405, 1993.
- [50] R. Hemmler, G. Böse, R. Wagner, and R. Peters. Nanopore unitary permeability measured by electrochemical and optical single transporter recording. *Biophys. J.*, 88:4000–4007, 2005.
- [51] M. Hofmann, C. Eggeling, S. Jakobs, and S.W. Hell. Breaking the diffraction barrier in fluorescence microscopy at low light intensities by using reversibly photoswitchable proteins. *Proc. Natl. Acad. Sci. USA*, 102(49):17565–17569, 2005.
- [52] T. Holthuis, J.C. and Pomorski, R.J. Raggars, H. Sprong, and G. van Meer. The organizing potential of sphingolipids in intracellular membrane transport. *Physiol. Rev.*, 81:1689–1723, 2001.
- [53] Y. W. Hsueh, K. Gilbert, C. Trandum, M. Zuckermann, and J. Thewalt. The effect of ergosterol on dipalmitoylphosphatidylcholine bilayers: a deuterium nmr and calorimetric study. *Biophys J*, 88:1799–1808, 2005.

- [54] K. Jacobson, O.G. Mouritsen, and G.W. Anderson. Lipid rafts: at a crossroad between cell biology and physics. *Nature Cell Biol.*, 9(1):7–14, 2007.
- [55] P. Kask, C. Eggeling, K. Palo, Ü. Mets, M. Cole, and K. Gall. Fluorescence intensity distribution analysis (fida) and related fluorescence fluctuation techniques: theory and practice. In R. Kraayenhof, A.J.W.G. Visser, and H.C. Gerritsen, editors, *Fluorescence Spectroscopy, Imaging and Probes - New Tools in Chemical, Physical and Life Sciences*, pages 153–181. Springer, 2002.
- [56] P. Kask, R. Günther, and P. Axhausen. Statistical accuracy in fluorescence fluctuation experiments. *Eur. Biophys. J.*, 25:163–169, 1997.
- [57] P. Kask and K. Palo. Introduction to the theory of fluorescence intensity distribution analysis. In R. Rigler and E.L. Elson, editors, *Fluorescence Correlation Spectroscopy - Theory and Applications*, pages 396–409. Springer, Berlin, Heidelberg, 2001.
- [58] P. Kask, K. Palo, D. Ullmann, and K. Gall. Fluorescence-intensity distribution analysis and its application in biomolecular detection technology. *Proc. Natl. Acad. Sci. USA*, 96:13756–13761, 1999.
- [59] L. Kastrup, H. Blom, C. Eggeling, and S. W. Hell. Fluorescence fluctuation spectroscopy in subdiffraction focal volumes. *Phys. Rev. Lett.*, 94:178104, 2005.
- [60] L. Kastrup and S. W. Hell. Absolute optical cross section of individual fluorescent molecules. *Angew. Chem. Int. Ed.*, 43:6646–6649, 2004.
- [61] J. Keller, A. Schönle, and S. W. Hell. Efficient fluorescence inhibition patterns for resoltf microscopy. *Opt. Express*, 15(6):3361–3371, 2007.
- [62] S.A. Kim, K.G. Heinze, and P. Schwille. Fluorescence correlation spectroscopy in living cells. *Nature Methods*, 4(11):963–73, 2007.
- [63] A.I. Kirkland and L Hutchinsons. Atomic resolution transmission electron microscopy. In P.W. Hawkes and J.C. Spence, editors, *Science of Microscopy*, volume 1, pages 3–64. Springer, 2007.
- [64] T. A. Klar, S. Jakobs, M. Dyba, A. Egner, and S. W. Hell. Fluorescence microscopy with diffraction resolution limit broken by stimulated emission. *Proc. Nat. Acad. Sci. U.S.A.*, 97:8206–8210, 2000.
- [65] D. E. Koppel. Statistical accuracy in fluorescence correlation spectroscopy. *Phys. Rev. A*, 10(6):1938–1945, 1974.
- [66] Joseph R. Lakowicz. *Principles of fluorescence spectroscopy*. Kluwer Academic/Plenum, New York, 1999.

- [67] J. M. Larkin, W. R. Donaldson, A.S. Foster, and R. S. Knox. Reverse intersystem crossing from a triplet state of rose bengal populated by sequential 532- +1064-nm laser excitation. *Chemical Physics*, 244:319–330, 1999.
- [68] P.-F. Lenne, L. Wawrezinieck, F. Conchonaud, O. Wurtz, A. Boned, X.-J. Guo, H. Rigneault, H.-T. He, and D. Marguet. Dynamic molecular confinement in the plasma membrane by microdomains and the cytoskeleton meshwork. *EMBO J.*, 25:3245–3256, 2006.
- [69] M.J. Levene, J. Korlach, S.W. Turner, M. Foquet, H.G. Craighead, and W.W. Webb. Zero-mode waveguides for single-molecule analysis at high concentrations. *Science*, 299:682–686, 2003.
- [70] D. Madge. Chemical kinetics and fluorescence correlation spectroscopy. *Quart. Rev. Biophys.*, 9(1):35–47, 1976.
- [71] D. Madge, E. L. Elson, and W. W. Webb. Thermodynamic fluctuations in a reacting system - measurement by fluorescence correlation spectroscopy. *Phys. Rev. Lett.*, 29(11):705–708, 1972.
- [72] O.C. Martin and R.C. Pagano. Internalization and sorting of a fluorescent analogue of glucosylceramide to the golgi apparatus of human skin fibroblasts: utilization of endocytic and nonendocytic transport mechanisms. *J. Cell Biol.*, 125:769–781, 1994.
- [73] W.E. Moerner and D.P. Fromm. Methods of single-molecule fluorescence spectroscopy and microscopy. *Rev. Sci. Instrum.*, 74(8):3597–3619, 2003.
- [74] M. Moertelmaier, M. Brameshuber, M. Linimeier, G. J. Schütz, and H. Stockinger. Thinning out clusters while conserving stoichiometry of labeling. *Appl. Phys. Lett.*, 87:263903, 2005.
- [75] D. Mueller, O. Rudin, H. T. Tien, and W. C. Wescott. Reconstruction of cell membrane structure in vitro and its transformation into an excitable system. *Nature*, 194:979–980, 1962.
- [76] P. Muller and A. Hermann. Rapid transbilayer movement of spin-labeled steroids in human erythrocytes and in liposomes. *Biophys J*, 82:1418–1428, 2002.
- [77] S. Munro. Lipid rafts: elusive or illusive? *Cell*, 115:377–388, 2003.
- [78] S. Y. Nishimura, M. Vrljic, L. O. Klein, H. M. McConnell, and W. E. Moerner. Cholesterol depletion induces solid-like regions in the plasma membrane. *Biophys. J.*, 90:927–938, 2006.
- [79] M. Orrit and J. Bernard. Single pentacene molecules detected by fluorescence excitation in a p-terphenyl crystal. *Phys. Rev. Lett.*, 65:2716–2719, 1990.
- [80] K. Palo, Ü. Mets, S. Jäger, P. Kask, and K. Gall. Fluorescence intensity multiple distribution analysis: Concurrent determination of diffusion times and molecular brightness. *Biophys. J.*, 79:2858–2866, 2000.

- [81] I. Pascher. Molecular arrangements in sphingolipids: Conformation and hydrogen bonding of ceramide and their implication on membrane stability and permeability. *Bioch. Biophys. Acta*, 455:433–451, 1976.
- [82] J. B. Pendry. Negative refraction makes a perfect lens. *Phys. Rev. Lett.*, 85(18):3966–3969, 2000.
- [83] C. Petibois and G.M. Cestelli. Bioimaging of cells and tissues using accelerator-based sources. *Anal. Bioanal. Chem.*, 391(5):1599–608, 2008.
- [84] Z. Petrasek and P. Schwille. Precise measurement of diffusion coefficients using scanning fluorescence correlation spectroscopy. *Biophys J*, 94(4):1437–1448, 2008.
- [85] L.J. Pike. Rafts defined: a report on the keystone symposium on lipid rafts and cell function. *J. Lipid Res.*, 47:1597–1598, 2006.
- [86] D. W. Pohl, W. Denk, and M. Lanz. Optical stethoscopy: Image recording with resolution 1/20. *Appl. Phys. Lett.*, 44:651–653, 1984.
- [87] A. Pralle, P. Keller, E.-L. Florin, K. Simons, and J. K. H. Hörber. Sphingolipid-cholesterol diffuse as small entities in the plasma membrane of mammalian cells. *J. Cell Biol.*, 148(5):997–1007, 2000.
- [88] S. Reindl and A. Penzkofer. Higher excited-state triplet-singlet intersystem crossing of some organic dyes. *Chem. Phys.*, 211:431–439, 1996.
- [89] R. Rigler and E. S. Elson. *Fluorescence correlation spectroscopy. Theory and applications*. Springer-Verlag, Berlin, Heidelberg, 2001.
- [90] R. Rigler, J. Widengren, and Ü. Mets. Interactions and kinetics of single molecules as observed by fluorescence correlation spectroscopy. In *Fluorescence Spectroscopy*. Springer Verlag, Berlin, 1992.
- [91] C. Ringemann, A. Schönle, A. Giske, C. von Middendorff, S.W. Hell, and C. Eggeling. Enhancing fluorescence brightness: effect of reverse intersystem crossing studied by fluorescence fluctuation spectroscopy. *Chemphyschem.*, 9(4):612–24, 2008.
- [92] E. Rittweger, B. R. Rankin, V. Westphal, and S. W. Hell. Fluorescence depletion mechanisms in super-resolving sted microscopy. *Chem. Phys. Lett.*, 442:483 – 487, 2007.
- [93] M.J. Saxton. Anomalous diffusion due to obstacles: a monte carlo study. *Biophys. J.*, 66:394–401, 1994.
- [94] M.J. Saxton and K. Jacobson. Single particle tracking: Applications to membrane dynamics. *Annu. Rev. Biophys. Biomol. Struct.*, 26:373–399, 1997.

- [95] A. Schönle and S. W. Hell. Heating by absorption in the focus of an objective lens. *Opt. Lett.*, 23(5):325–327, 1998.
- [96] G.J. Schütz, G. Kada, V.Ph. Pastushenko, and H. Schindler. Properties of lipid microdomains in a muscle cell membrane visualized by single molecule microscopy. *EMBO J.*, 19(5):892–901, 2000.
- [97] G. Schwarzmann, P. Hofmann, U. Pütz, and B. Albrecht. Demonstration of direct glycosylation of nondegradable glucosylceramide analogs in cultured cells. *J. Biol. Chem.*, 270(36):21271–21276, 1995.
- [98] G. Schwarzmann, M. Wendeler, and K. Sandhoff. Synthesis of novel nbd-gm1 and nbd-gm2 for the transfer activity of gm2-activator protein by a fret-based assay system. *Glycobiology*, 15(12):1302–1311, 2005.
- [99] M. Schwentker, H. Bock, M. Hofmann, S. Jakobs, J. Bewersdorf, C. Eggeling, and S. W. Hell. Wide-field subdiffraction resolt microscopy using fluorescent protein photoswitching. *Micr. Res. Tech.*, 70(3):269–280, 2007.
- [100] P. Schwille, U. Haupts, S. Maiti, and W.W. Webb. Molecular dynamics in living cells observed by fluorescence correlation spectroscopy with one- and two-photon excitation. *Biophys. J.*, 77:2251–2265, 1999.
- [101] P. Schwille, K. Korlach J., and W.W. Webb. Fluorescence correlation spectroscopy with single-molecule sensitivity on cell and model membranes. *Cytometry*, 36:176–182, 1999.
- [102] P. Schwille, F. J. Meyer-Almes, and R. Rigler. Dual-color fluorescence cross-correlation spectroscopy for multicomponent diffusional analysis in solution. *Biophys. J.*, 72(4):1878–1886, 1997.
- [103] P. Sharma, R. Varma, R.C. Sarasij, K. Gousset, G. Krishnamoorthy, M. Rao, and S. Mayor. Nanoscale organization of multiple gpi-anchored proteins in living cell membranes. *Cell*, 116:577–589, 2004.
- [104] E. Brooks Shera, Newton K. Seitzinger, Lloyd M. Davis, Richard A. Keller, and Steven A. Soper. Detection of single fluorescent molecules. *Chem. Phys. Lett.*, 174(6):553–557, 1990.
- [105] K. Simons and E. Ikonen. Functional rafts in cell membranes. *Nature*, 387:569–572, 1997.
- [106] K. Simons and G. van Meer. Sorting in epithelial cells. *Biochemistry*, 27:6197–6202, 1988.
- [107] T. Staudt, M. Lang, R. Medda, J. Engelhardt, and S. W. Hell. 2,2'-thiodiethanol: a new water soluble mounting medium for high resolution optical microscopy. *Microsc. Res. Tech.*, 70:1–9, 2007.

- [108] G.G. Stokes. On the refrangibility of light. *Phil. Trans.*, 142:463–562, 1852.
- [109] J. Thewalt and M. Bloom. Phosphatidylcholine: cholesterol phase diagrams. *Biophys J*, 63:1176–1181, 1992.
- [110] Nancy L. Thompson. Fluorescence correlation spectroscopy. In *Topics in Fluorescence Spectroscopy*, pages 337–378. Plenum Press, New York/ London, 1991.
- [111] T.E. Thompson and T.W. Tillack. Organization of glycosphingolipids in bilayers and plasma membranes of mammalian cells. *Annu. Rev. Biophys. Biophys. Chem.*, 14:361–386, 1985.
- [112] G. van Meer. Lipid traffic in animal cells. *Annu. Rev. Cell Biol.*, 5:247–275, 1989.
- [113] M. Wachsmuth, W. Waldeck, and J. Langowski. Anomalous diffusion of fluorescent probes inside living cell nuclei investigated by spatially-resolved fluorescence correlation spectroscopy. *J. Mol. Biol.*, 298:677–689, 2000.
- [114] J. R. Wang, T.-Y. & Silvius. Different sphingolipids show differential partitioning into sphingolipid/cholesterol-rich domains in lipid bilayers. *Biophys J*, 79:1478–1489, 2000.
- [115] L. Wawrezynieck, H. Rigneault, D. Marguet, and P.-F. Lenne. Fluorescence correlation spectroscopy: diffusion laws to probe the submicron cell membrane organization. *Biophys J*, 89:4029–4042, 2005.
- [116] S. Weiss. Fluorescence spectroscopy of single biomolecules. *Science*, 283:1676–1683, 1999.
- [117] J. Wenger, F. Conchonaud, J. Dintinger, L. Wawrezynieck, T.W. Ebbesen, H. Rigneault, D. Marguet, and P.-F. Lenne. Diffusion analysis within single nanometric apertures reveals the ultrafine cell membrane organization. *Biophys. J.*, 92(3):913–919, 2007.
- [118] J. Widengren, A. Chmyrov, C. Eggeling, P.-A. Löfdahl, and C. A. M. Seidel. Strategies to improve photostabilities in ultrasensitive fluorescence spectroscopy. *J. Phys. Chem. A*, 111:429–444, 2007.
- [119] J. Widengren, Ü. Mets, and R. Rigler. Fluorescence correlation spectroscopy of triplet states in solution: A theoretical and experimental study. *J. Phys. Chem.*, 99:13368–13379, 1995.
- [120] J. Widengren and R. Rigler. Mechanisms of photobleaching investigated by fluorescence correlation spectroscopy. *Bioimaging*, 4(3):149–156, 1996.
- [121] J. Widengren, R. Rigler, and Ü. Mets. Triplet-state monitoring by fluorescence correlation spectroscopy. *J. Fluoresc.*, 4:255–258, 1994.
- [122] K. Willig, J. Keller, M. Bossi, and S.W. Hell. Sted microscopy resolves nanoparticle assemblies. *New J. Phys.*, 8:106, 2006.

- [123] K. I. Willig, R. R. Kellner, R. Medda, B. Hein, S. Jakobs, and S. W. Hell. Nanoscale resolution in gfp-based microscopy. *Nature Methods*, 3(9):721–723, 2006.
- [124] K. I. Willig, S. O. Rizzoli, V. Westphal, R. Jahn, and S. W. Hell. Sted-microscopy reveals that synaptotagmin remains clustered after synaptic vesicle exocytosis. *Nature*, 440(7086):935 – 939, 2006.
- [125] B.V. Ramos Y. Lange, M.H. Swaisgood and T.L. Staeck. Plasma membranes contain half the phospholipid and 90cholesterol and sphingomyelin in cultured human fibroblasts. *Journal of biological Chemistry*, 264:3786–3793, 1989.
- [126] E. Yechiel and M. Edidin. Micrometer-scale domains in fibroblast plasma membranes. *J. Cell Biol.*, 105(2):755–760, 1987.
- [127] A. Yethiraj and J.C. Weisshaar. Why are lipid rafts not observed in vivo? *Biophys J BioFAST*, 93:3113–3119, 2007.
- [128] D.A. Zacharias, J.D. Violin, A.C. Newton, and R.Y. Tsien. Partitioning of lipid-modified monomeric gfps into membrane microdomains of live cells. *Science*, 296:913–916, 2002.
- [129] Christoph Zander, Jörg Enderlein, and Richard A. Keller (eds.). *Single-molecule detection in solution*. Wiley-VCH, Berlin, Germany, 1st edition, 2002.

## Acknowledgment

This thesis was carried out in the department of NanoBiophotonics at the Max-Planck-Institute for Biophysical Chemistry in Göttingen. I would like to thank all people who have directly or indirectly contributed to the success of this thesis.

First of all, I would like to thank Prof. Dr. Stefan Hell not only for offering the fascinating and challenging project of STED Fluorescence Fluctuation Spectroscopy, but also for the outstanding and highly motivating scientific environment. His continuous interest and inspiring support in the project has significantly contributed to the success of the work.

I would like to thank Prof. Dr. T. Salditt from the Georg-August University of Göttingen for his interest in my work and his willingness to be the first referee of my thesis.

I am especially thankful to Dr. Christian Eggeling. Without his continuous support and help this work would not have been possible.

I also like to thank the following former and present members of the department of NanoBiophotonics

- Rebecca Medda for providing most of the biological samples used in this work.
- Class von Middendorf and Dr. Andreas Schönle for implementing and designing the Monte Carlo simulation of the membrane lipids, which greatly clarified the analysis of the data.
- Dr. Vladimir Belov and Svetlana Polyakova for providing some of the dye-labeled lipids in my experiment.
- Birka Hein for help in the labeling of the GPI anchor lipids and providing additional data for the diffusion of the membrane lipids.
- Arnold Giske for his support and advise in the beginning of my thesis. Discussing with him about the details of the optical setup was very helpful.
- Jaydev Jethwa and Harald Meyer for their technical assistance and helpful advise.
- Dr. Jan Keller, Dr. Ben Harke, Dr. Chaitanya Ullal and Brian Rankin for proof reading the manuscript.

This work would not have been possible without the help of the mechanical and optical workshop.

I am also thankful to all the other members of the NanoBiophotonic department for providing a really nice and comfortable working atmosphere.



Finally, I like to thank my parents Heinz Ringemann and Maria Ringemann, as well as my girlfriend Cornelia Köhl for their support during the time of my studies.

# Lebenslauf

## **Persönliche Daten**

---

Name, Vorname	Ringemann, Christian
Geburtsdatum	25.06.1978
Geburtsort	Harsewinkel
Familienstand	ledig
Nationalität	deutsch

## **Schulbildung**

---

1985 - 1989	Grundschule, Greffen
1990 - 1998	CJD Gymnasium Versmold

## **Zivildienst**

---

1998-1999	Elisabeth Hospital, Gütersloh
-----------	-------------------------------

## **Studium**

---

1999 - 2001	Grundstudium der Biophysik, Humboldt Universität Berlin
2001 - 2005	Hauptstudium der Biophysik, Humboldt Universität Berlin
seit 2005	Promotion am Max-Planck-Institut für Biophysikalische Chemie, Abteilung Nanobiophotonik

Göttingen den 22.10.2008    Christian Ringemann